

HSOH

—

An elusive species with
many different traits.

Inaugural-Dissertation

zur

Erlangung des Doktorgrades

der Mathematisch-Naturwissenschaftlichen Fakultät

der Universität zu Köln

vorgelegt von

OLIVER BAUM

AUS KÖLN

Köln 2008

I. Berichterstatter:
II. Berichterstatter:

Privatdozent Dr. Thomas F. Giesen
Professor Dr. Markus Grüninger

Tag der mündlichen Prüfung:

Für Sonja

When I heard the learn'd astronomer;
When the proofs, the figures, were ranged
in columns before me;
When I was shown the charts and the diagrams,
to add, divide, and measure them;
When I, sitting, heard the astronomer, where
he lectured with much applause in
the lecture-room,
How soon, unaccountable, I became tired and sick;
Till rising and gliding out, I wander'd off by myself,
In the mystical moist night-air, and from time to time,
Look'd up in perfect silence at the stars.

Walt Whitman (1819–1892)

Abstract

In the scope of this thesis different traits of the elusive species HSOH have been examined. HSOH, either known as oxadisulfane or hydrogen thio-peroxide is the link between the well known molecules HSSH, disulfane, and HOOH, hydrogen peroxide. HSOH is not only interesting because of its relevance in the combustion theory of sulfur, the sulfur cycle in the atmosphere, or as possible constituent in the interstellar medium but also because of its substantially spectroscopical importance.

With two different rotor moieties, SH and OH, HSOH represents the most general case of a four-atomic, internally rotating chain molecule. In order to provide further improvement of the theoretical understanding of internal rotation earlier experimental studies by Winnewisser *et al.*¹ have been extended into the THz-region.

The first gas-phase detection of the singly deuterated oxadisulfane HSOD presented here provided the last piece of the puzzle to determine a semi-experimental equilibrium structure of HSOH.

In order to get information on the dynamics involved in the molecule, the measurements have been extended into the infrared region and both high frequency bond stretching modes $\nu_{OH} = 1$ and $\nu_{SH} = 1$ have been assigned. The analysis of the bands proves HSOH to be a fairly rigid “textbook” molecule in case of the OH-stretching mode, while the $\nu_{SH} = 1$ state shows a strong potential coupling to some dark state.

Last but not least, it turned out that HSOH exhibits an anomalous intensity pattern for rotational transitions involving $K_a > 3$ states. Even though this effect is not reported yet it seems to be not a special trait of HSOH, but rather a spectroscopic effect of general importance.

¹G. Winnewisser, F. Lewen, S. Thorwirth, M. Behnke, J. Hahn, J. Gauss, E. Herbst. Gas-Phase detection of HSOH: Synthesis by Flash Vacuum Pyrolysis of ditert-butyl-sulfoxide and rotational-torsional spectrum. *Chem. Eur. J.* **9** (2003) 5501–5510.

Kurzzusammenfassung

Im Rahmen dieser Arbeit wurden verschiedene Eigenschaften des instabilen und daher nur schwer zu fassenden Moleküls HSOH untersucht. HSOH ist sowohl als Oxadisulfan als auch als Wasserstoff-thio-peroxid bekannt. Es ist das Bindeglied zwischen den gut bekannten Molekülen HSSH, Disulfan, und HOOH, Wasserstoffperoxid. HSOH ist nicht nur auf Grund seiner Bedeutung im Rahmen der Verbrennungstheorie von Schwefel, dem Schwefelkreislauf in der Atmosphäre und als mögliches Molekül im Interstellaren Medium interessant, sondern vor allem auch aus spektroskopischer Sicht wegen seiner fundamentalen Eigenschaften.

HSOH repräsentiert mit zwei verschiedenen rotierenden Gruppen, SH und OH, den allgemeinsten Fall eines Ketten-Moleküls mit vier Atomen, welches die Eigenschaft einer internen Rotation aufweist. Um weitere Daten, die für das theoretische Verständnis dieses Effektes nötig sind, zu erhalten, wurden frühere Untersuchungen von Winnewisser *et al.*² im Rahmen dieser Arbeit in den THz-Bereich ausgedehnt.

Die im Rahmen dieser Arbeit präsentierte Entdeckung des einfach deuterierten Oxadisulfan, HSOD, ebnete den Weg zur Bestimmung einer semi-experimentellen Gleichgewichtsstruktur von HSOH. Um mehr über die dynamischen Eigenschaften des Moleküls zu erfahren, wurden die Messungen in den Infrarot-Bereich ausgedehnt. Im Rahmen dieser Messungen konnten zwei Schwingungsbanden den hochfrequenten Streckschwingungen ν_{OH} und ν_{SH} zugeordnet werden. Die Analyse der beiden Banden zeigt, dass HSOH im Fall der OH-Streckschwingung ein verhältnismäßig starres "Lehrbuch"-Molekül ist. Im Gegensatz hierzu zeigt der Zustand mit $\nu_{SH} = 1$ eine starke Potentialkopplung mit einem weiteren, nicht näher bekannten Zustand.

Als weiteres Ergebnis dieser Arbeit zeigt sich, dass die Rotationsübergänge im Spektrum von HSOH für $K_a > 3$ eine nicht erwartete Intensitätsverteilung aufweisen. Ein ähnlicher Effekt ist noch nicht in der Literatur beschrieben. Dennoch scheint es sich nicht um eine spezielle Eigenschaft von HSOH zu handeln, sondern vielmehr um ein generelles Phänomen von hoher spektroskopischer Bedeutung.

²G. Winnewisser, F. Lewen, S. Thorwirth, M. Behnke, J. Hahn, J. Gauss, E. Herbst. Gas-Phase detection of HSOH: Synthesis by Flash Vacuum Pyrolysis of ditert-butyl-sulfoxide and rotational-torsional spectrum. *Chem. Eur. J.* **9** (2003) 5501–5510.

Zusammenfassung

HSOH, welches in der Literatur sowohl unter dem Namen Oxadisulfan als auch als Wasserstoff-thio-peroxid geführt wird, kann als Bindeglied zwischen den Molekülen Disulfan, HSSH, und Wasserstoffperoxid, HOOH, betrachtet werden. Schon seit langer Zeit kennen Chemiker die Strukturen und chemischen Eigenschaften der Geschwister-Moleküle HSSH und HOOH³. Im Gegensatz hierzu gibt es nur wenige Informationen über das Molekül HSOH.

Auf Grund einer fehlenden effizienten Synthese für HSOH waren Untersuchungen in der Gasphase lange Zeit nicht möglich. Der Durchbruch zur Synthese des Moleküls in großen Mengen gelang Behnke und Hahn [10, 123] im Jahr 2003. Winnewisser *et al.* [123] führten daraufhin erste rotationsspektroskopische Messungen an dem Molekül durch und identifizierte die gemessenen Linien mit Hilfe extrem genauer Vorhersagen von Gauss *et al.*, welche auf Quantenchemischen *ab-initio* Rechnungen auf höchstem Niveau beruhten.

Es stellte sich heraus, dass HSOH ein asymmetrisches Kreisel-Molekül, nah an dem Grenzfall des symmetrischen prolaten Kreisels ist. Aus diesem Grund sehen die reinen Rotations- und Rotations-Vibrations-Spektren auf den ersten Blick verhältnismäßig einfach aus. Wenn man jedoch etwas mehr ins Detail geht, so stellt sich heraus, dass das Molekül einige Eigenheiten offenbart, welche mit den grundlegenden Konzepten der Rotations-Vibrations-Theorie nicht zu erklären sind. Diese Effekte genauer zu untersuchen war ein Ziel dieser Arbeit.

Zum einen ist HSOH, so wie auch HSSH und HOOH, eines der einfachsten Beispiele für ein chirales Molekül. Das heißt HSOH hat zwei stabile Konfigurationen, welche zwar energetisch jedoch nicht geometrisch äquivalent sind. Eine Konfiguration bildet das so genannte rechtshängige und die andere das linkshändige Isomer. Diese beiden Isomere können nicht getrennt werden, denn mittels Tunneln durch die sie trennende Potential Barriere tauschen sie ihre Konfigurationen zwischen links- und rechtshändig hin und her. Der

³Siehe für HOOH: [46, 95, 96, 107] und für HSSH: [11, 16, 40, 47, 121].

Tunnelvorgang durch die Barriere ist eine so genannte interne Rotation um die S-O Bindung im HSOH. Offensichtlich ist HSOH nicht so symmetrisch wie HSSH und HOOH, deshalb ist HSOH nicht nur eines der einfachsten chiralen Moleküle, sondern auf Grund der unterschiedlichen Bewegungsgruppen, SH und OH, ist es gleichzeitig der allgemeinste Fall eines vier-atomigen Moleküls, welches eine interne Rotation aufweisen kann. Die aufgenommenen Linien von HSOH spalten daher in Doppellinien auf.

Eine erste Erklärung dieses Phänomens -der internen Rotation in HSOH- wird durch das *Yamada-Winnewisser-Jensen* (YWJ) Modell [130] gegeben. In diesem Modell ist es notwendig, die Periode für die interne Rotation von 2π auf 6π zu erweitern. Das bedeutet, dass HSOH nicht nur ein links- und ein rechtshändiges Isomer hat, sondern viel mehr sechs äquivalente Spiegelbilder.

Um das YWJ Modell experimentell zu überprüfen, wurden im Rahmen dieser Arbeit weitere Messungen an HSOH durchgeführt. Es konnten erstmalig die Aufspaltungen der Energiezustände mit $K_a = 4$ und 5 experimentell bestimmt werden, des Weiteren ermöglichten die hoch präzisen Messungen eine Überarbeitung und genauere Bestimmung der von Yamada *et al.* [130] angegebenen Aufspaltungen für die Energiezustände mit $K_a = 0, 1, 2$ und 3 . Die in dieser Arbeit erhaltenen Werte zeigen, dass das YWJ Modell in der Lage ist die beobachteten Aufspaltungen qualitativ zu erklären.

In einer Zusammenarbeit mit Theoretikern um Ovsyannikov wurden die hier erhaltenen Werte genutzt um ein neues, das YWJ-Modell vervollständigtes Modell zu entwickeln. Ovsyannikov *et al.* [89] benutzten hierzu einen direkteren Ansatz, d.h. sie benutzten das Programm TROVE [132] zusammen mit einer neu berechneten Potentialhyperfläche für HSOH. Die auf diese Weise erhaltenen Werte stimmen nicht nur qualitativ, sondern auch quantitativ hervorragend mit den experimentellen Werten überein.

Ein weiterer Effekt, welcher nicht durch einfache Modelle der Rotations-Vibrations-Theorie zu erklären ist betrifft die beobachtete Intensitätsanomalie für Übergänge von $K_a = 4 \leftarrow 3$. Übergänge von $K_a = 1 \leftarrow 0$, $K_a = 2 \leftarrow 1$ und $K_a = 3 \leftarrow 2$ haben starke *c*-Typ und etwas schwächere *b*-Typ Linien. Für den Übergang $K_a = 4 \leftarrow 3$ wurden hingegen keine *b*-Typ Linien beobachtet. Dieser Effekt ist vollkommen unerwartet und bis jetzt noch nicht in allen Details verstanden. Ein im Rahmen dieser Arbeit gegebener erster Erklärungsansatz deutet darauf hin, dass es sich bei diesem Effekt nicht um eine spezielle Eigenschaft von HSOH handelt, sondern dass es sich hierbei vielmehr um ein allgemeines Phänomen handelt, welches jedes asymmetrische Kreiselmolekül mit einer internen Rotation aufweisen sollte.

Hochauflöste Infrarot-Messungen der SH- und OH- Streckschwingungen des Oxdisulfan wurden mit Hilfe eines Bruker IFS 120 HR Fourier Transform Spektrometer (Bergische Universität Wuppertal) aufgenommen. Mehr als 1300 Linien konnten der $\nu(\text{OH})$ fundamentalen Schwingungsmode zugeordnet werden. Diese Vibrationsmode verhält sich wie *im Lehrbuch* und

zeigt klare Senkrecht- und Parallel-Hybridbanden. Eine Aufspaltung der Linien durch das "Torsions-Tunneln" wurde in dieser Bande nicht beobachtet. Die Analyse der Daten gibt einen Wert von 3625.6 cm^{-1} für das Bandenzentrum, sowie die Rotationskonstanten und Zentrifugaldehnungskonstanten für den angeregten $\nu_{OH}=1$ Zustand.

Der Ursprung der $\nu(\text{SH})$ Schwingungsmode liegt bei 2538.0 cm^{-1} und damit nur wenig über der $(\nu_1 + \nu_3)$ Kombinationsbande des Nebenproduktes SO_2 bei 2500.0 cm^{-1} . Hierdurch ist der Bereich der *P*-Zweige der SH-Streckschwingung durch die Bande des Nebenprodukts überdeckt. Dennoch konnten dieser Vibrationsmode mehr als 700 Linien zugeordnet werden. Es zeigt sich, dass die Intensität der Bande rund 5 Mal schwächer als die der OH-Streckschwingung ist. Im Gegensatz zu der $\nu(\text{OH})$ Bande spalten die Übergänge im $\nu_{SH} = 1$ Zustand in Doppellinien auf. Dieses unerwartete Ergebnis zeigt die Grenzen des klassischen Modells von Normalschwingungen auf und ist mit einer Potentialkopplung zwischen der SH-Streckschwingung und einem weiteren, nicht näher bekannten Zustand zu erklären. Auch für diesen schwingungsangeregten Zustand wurden sowohl die Rotationskonstanten als auch Zentrifugaldehnungskonstanten bestimmt.

HSOH ist jedoch nicht nur wegen seiner fundamentalen spektroskopischen Charakterzüge interessant sondern auch wegen seiner chemischen Eigenschaften.

Schwefel formt eine große Vielfalt an Oxo-Säuren $\text{H}_x\text{S}_y\text{O}_z$. Es wird weitgehend angenommen, dass diese Schwefel-Sauerstoff-Säuren eine Rolle bei der Bildung von Luftverunreinigungen in der oberen Atmosphäre der Erde spielen. Die meisten dieser Verbindungen sind zu unstabil um in reiner Form untersucht zu werden. Deshalb sind sowohl die physikalischen als auch die chemischen Eigenschaften dieser wichtigen Gruppe von Molekülen nicht gut bekannt. Die einfachsten Sauerstoffsäuren des Schwefels haben die Gestalt H_2SO_n mit $n = 1, \dots, 4$. Für keines dieser Moleküle ist bisher eine experimentelle Gleichgewichtsstruktur in der Gasphase bestimmt worden. HSOH ist das kleinste Mitglied dieser Gruppe und es ist zudem das einfachste Molekül, welches eine S-O Einfachbindung aufweist. In Molekülen wie HSO, SO oder SO_2 handelt es sich um eine S-O Mehrfachbindung. Bis jetzt ist noch kein experimenteller Wert für eine S-O Einfachbindung verfügbar.

Ein weiteres Ziel dieser Arbeit war somit die experimentelle Strukturbestimmung von Oxadisulfan. Um die hierfür notwendigen Messungen an weiteren Isotopologen des HSOH durchführen zu können wurde in enger Zusammenarbeit mit der Anorganischen Chemie der Universität zu Köln [39] nach neuen Synthesemethoden für HSOH und seine Isotopologen gesucht. Es zeigte sich, dass HSOH auch in einer Radiofrequenz Entladung mit Wasser und Schwefel gebildet wird. Dieser "einfache Weg" der Synthese eröffnete die Herstellung von HSOD mit Hilfe von einfach deuteriertem Wasser (HDO) und Schwefel.

Im Rahmen dieser Arbeit werden die ersten Gasphasen-Spektren des einfach deuteriertem Oxadisulfan, HSOD, im Vibrationsgrundzustand vorge-

stellt. Mit Hilfe des Kölner Terahertz Spektrometers wurden mehr als 100 Übergänge mit höchster Genauigkeit gemessen. Die Analyse der Daten zeigt, dass auch HSOD ein nur leicht asymmetrisches Kreiselmolekül nahe am Grenzfall des symmetrischen prolaten Kreisels ist ($\kappa = -0.9985$). Im Bereich zwischen 716 bis 772 GHz wurden sowohl *c*- als auch etwas schwächere *b*-Typ Linien aufgenommen. Die *c*-Typ Linien spalten auf Grund des Tunneln durch die internen Rotation in Doppellinien auf, wohingegen für *b*-Typ Linien keine Aufspaltung innerhalb der Dopplerbreite gemessen wurde.

Die hier bestimmten Daten zu HSOD lieferten das letzte Puzzlestück zur experimentellen Bestimmung der Struktur von Oxadisulfan. Um die Gleichgewichtsstruktur von HSOH zu bestimmen wurden die in dieser Arbeit experimentell bestimmten Rotationskonstanten A_0 , B_0 und C_0 von HSOH, $H^{34}\text{SOH}$ und HSOD sowie von Brünken *et al.* [19] bestimmte Werte für DSOD genutzt. Die benötigten Gleichgewichtskonstanten A_e , B_e und C_e wurden mit Hilfe Rotations-Vibrations Wechselwirkungskonstanten α_r aus hoch genauen quantenchemischen *ab initio* Rechnungen bestimmt.

Die theoretischen Rotations-Vibrations Wechselwirkungsterme, welche zur Berechnung der semi-experimentellen Gleichgewichtsstruktur benutzt wurden, stimmen hervorragend mit den aus der Analyse der Infrarotspektren verfügbaren α_{OH} und α_{SH} überein.

Auf Grund des “einfachen” Syntheseweges von HSOH über Schwefel und Wasser ist es durchaus wahrscheinlich, dass Oxadisulfan auch im Interstellaren Raum reichlich vorhanden ist. Im Rahmen dieser Arbeit werden mögliche “Interstellare Synthese-Routen” diskutiert. Die in dieser Arbeit erhaltenen Molekülparameter für HSOH und seine Isotopomere bilden die Grundlage für eine Suche nach dem Molekül im Interstellaren Raum. Der Nachweis von HSOH im All würde weitere Einblicke in die interstellare Chemie des Schwefels als auch der Astrochemie im Allgemeinen geben.

Contents

Abstract	i
Kurzzusammenfassung	iii
Zusammenfassung	v
1 Introduction	1
2 Theoretical Considerations	7
2.1 Rotational Spectroscopy	7
2.1.1 Symmetric Top Molecules	9
2.1.2 Asymmetric Top Molecules	13
2.1.3 Spectral line intensities	17
2.2 Vibrational Spectroscopy	19
2.2.1 Normal Coordinates of Vibration	19
2.2.2 Quantum Mechanical Description	20
2.2.3 Selection Rules	21
2.2.4 Anharmonicities	22
2.2.5 Internal Coordinates	23
2.2.6 Vibration-Rotation	24
2.3 Internal motions	26
2.3.1 <i>Yamada-Winnewisser-Jensen</i> model	27
2.4 Derivation of Molecular Structures	35
2.4.1 Evaluation of Equilibrium Structures	36

3	Basics on Quantum Chemical Calculations	39
3.1	<i>Ab initio</i> Molecular Orbital Theory	40
3.1.1	The physicochemical model	40
3.1.2	Hartree-Fock theory	41
3.1.3	Basis Sets	46
3.1.4	Electron correlation	48
3.2	Theoretical ROVibrational Energies (TROVE)	53
4	Laboratory Spectroscopy	55
4.1	The Cologne Terahertz Spectrometer	55
4.2	Frequency Multipliers	59
4.2.1	Design of Frequency Multipliers	59
4.3	Fourier Transform Infrared Spectrometer	62
4.3.1	Resolution	64
4.3.2	Apodization	64
4.3.3	Bruker IFS 120HR	65
5	Synthesis of 1-oxadisulfane (HSOH) and its isotopologues	67
5.1	Synthesis of 1-oxadisulfane by flash vacuum pyrolysis of di- <i>tert</i> -butyl sulfoxide	67
5.2	Synthesis of the single deuterated 1-oxadisulfane (HSOD) by <i>rf</i> -discharge of pure sulfur (S ₈) and HDO	69
5.3	Synthesis of HSOH in the interstellar medium	69
5.4	Conclusion and Discussion	73
6	Rotational torsional spectrum of singly deuterated 1-oxadisulfane, HSOD	75
6.1	Synthesis of HSOD: Elimination of by-products	75
6.2	rQ_2 -branch of HSOD at 729 GHz	76
6.3	Molecular Parameters	78
6.4	Conclusion and Discussion	79
7	Empirical equilibrium structure of HSOH	83
7.1	Geometrical parameters of HSOH	85
7.2	Conclusion and Discussion	85

8	High Resolution Infrared Measurements on HSOH	89
8.1	Fundamental OH-stretching mode of HSOH	92
8.1.1	The <i>a</i> -type parallel band	94
8.1.2	The <i>c</i> -type perpendicular band	96
8.1.3	Molecular Parameters	97
8.1.4	Conclusion and Discussion	98
8.2	Fundamental SH-stretching mode of HSOH	100
8.2.1	The torsional splitting in the first excited SH stretch- ing state of HSOH	102
8.2.2	Molecular Parameters	105
8.2.3	Conclusion and Discussion	108
9	Measurements on HSOH and its isotopologue H³⁴SOH at 1.3 THz	111
9.1	The rQ_3 -branch of HSOH and its isotopologue H ³⁴ SOH	112
9.2	Internal rotation tunneling in HSOH	117
9.3	Intensity anomaly in <i>b</i> -type transitions of HSOH	121
9.4	Conclusion and Discussion	125
10	Conclusion and Prospects	127
	Bibliography	129
	Acknowledgement	140

List of Tables

2.1	Identification of the a, b, c axes with the x, y, z axes.	8
2.2	Relations between the distortion coefficients of the A and S reduced Hamiltonians	16
2.3	Selection rules for asymmetric top molecules.	17
4.1	Equipment of the FT-IR Spectrometer IFS 120HR at different spectral regions.	66
5.1	Cosmic abundance of the elements normalized to $\text{Si} = 10^6$	70
5.2	Interstellar and circumstellar molecules	72
6.1	Ground state molecular parameters of HSOD	81
7.1	Geometrical parameters for HSOH	85
7.2	Rotational constants and vibrational corrections for HSOH and its isotopologues	86
7.3	Geometrical parameters for HOOH, HSOH, and HSSH	86
8.1	Calculated and experimental Matrix vibrational modes (cm^{-1}) (relative intensities in parentheses)	90
8.2	Spectroscopic parameters for the $\nu(\text{OH})$ first excited state of HSOH.	98
8.3	Spectroscopic parameters for the $\nu(\text{SH})$ first excited state of HSOH.	107
9.1	Ground state molecular parameters of H^{32}SOH and H^{34}SOH	116
9.2	Experimental tunnelling splittings of transitions in MHz.	118

9.3	Observed and calculated internal rotation splittings δ_{K_a} (MHz) for energy levels.	119
9.4	Permanent dipole moment components for HSOH	121
9.5	Intensity ratio S_b/S_c in the ${}^rQ_{K_a}$ -branches ($K_a = 0, 1, 2, 3$) . . .	124

List of Figures

1.1	The kin molecules HOOH, HSOH, and HSSH.	1
1.2	The enantiomers of HSOH.	2
1.3	Schematic diagram of the electromagnetic spectrum and corresponding interactions of radiation with molecules. . . .	4
2.1	Correlation diagram of the asymmetric rotor energy levels. .	13
2.2	Scheme of two vibrational levels of an accidentally symmetric prolate top molecule.	25
2.3	The two equivalent equilibrium configurations of HSOH. . .	27
2.4	Rotation angles χ_1 , χ_2 , and internal rotation angle τ of HSOH.	28
2.5	The 6π -periodic potential $V(\tau)$ for HSOH.	30
2.6	The pattern of torsional energy-level splittings for states with $K = 3t > 0$ for HSOH	31
2.7	The pattern of torsional energy-level splittings for states with $K = 3t \pm 1$ for HSOH	32
2.8	The pattern of torsional energy-level splittings for states with $K = 3t \pm 1$ in the symmetric top limit for HSOH.	34
2.9	Sketch of a harmonic and an anharmonic potential of a diatomic molecule.	35
3.1	Comparison of exponential and gaussian functions.	45
4.1	Schematic of the Cologne Terahertz Spectrometer.	56
4.2	Schematic drawing of a Backward-Wave-Oscillator.	57
4.3	Planar multiplier chain.	60
4.4	All-solid-state terahertz source.	61

4.5	Optical schematic of a classic Michelson interferometer. . .	62
4.6	Schematic of data acquisition in a FT-IR spectrometer . . .	63
4.7	Schematic sketch of the Bruker IFS 120HR.	66
5.1	Synthesis of HSOH via pyrolysis of di- <i>tert</i> -butyl sulfoxide. .	68
5.2	Decomposition route of HSOH. (see [8])	68
5.3	Potential energy surface for the reaction $\text{H}_2\text{O} + \text{S}(^1\text{D}) \rightarrow \text{HSOH}$. 74	
6.1	Spectrum and reference spectra of discharge generated HSOD. 76	
6.2	Band-head region of the rQ_2 -branch of HSOD.	77
6.3	Fortrat diagram of the HSOD rQ_2 -branch at 729 GHz. . . .	78
7.1	The kin molecules HOOH, HSOH, and HSSH.	84
7.2	Equilibrium configuration and direction of the three principal axes of HSOH.	87
8.1	Gas-phase IR-spectra of the pyrolysis of di- <i>tert</i> -butyl sulfoxide products.	91
8.2	Measured and calculated spectrum of HSOH at the $\nu(\text{OH})$ band center region.	92
8.3	Band center region of the $\nu(\text{OH})$ stretching mode.	93
8.4	Sub-bands of the parallel band from the $\nu(\text{OH})$ of HSOH. .	94
8.5	Rotational energy (in the $\nu_{\text{OH}} = 1$ state) of the slightly asymmetric top molecule HSOH.	95
8.6	Sub-bands of the perpendicular band from the $\nu(\text{OH})$ of HSOH.	96
8.7	Fortrat diagram of the $\nu(\text{OH})$ perpendicular band of HSOH	97
8.8	Calculated parallel band, perpendicular band, and spectrum of the fundamental OH-stretching mode of HSOH.	99
8.9	Experimental and calculated spectrum of the $\nu(\text{SH})$ fundamental vibrational mode of HSOH.	100
8.10	Band center region of the $\nu(\text{SH})$ stretching mode of HSOH.	101
8.11	Torsional splittings of transitions in the $\nu_{\text{SH}} = 1$ -state.	103
8.12	Minimum-energy path of HSOH.	105
8.13	Torsional splitting of <i>a</i> - and <i>b</i> - type transitions in the $\nu_{\text{SH}} = 1$ state.	106

8.14	rQ_0 -branch of the $\nu_{SH} = 1$ state.	108
9.1	Band head of the rQ_3 -branch of HSOH and its isotopologue $H^{34}SOH$	113
9.2	$J = 5 \leftarrow 4$ c -type transition of the rR_4 -branch.	114
9.3	Fortrat diagram of HSOH and its isotopologue $H^{34}SOH$	115
9.4	Torsional splitting for b - and c -type transitions of the ${}^rQ_{K_a}$ -branches with $K_a = 0, 1, 2, 3$	117
9.5	The ${}^rQ_{K_a}$ transitions of HSOH.	118
9.6	Unique pattern of hypothetical b - and c -type transitions in the rQ_3 -branch.	122
9.7	rQ_2 -branch of HSOH.	123

Introduction

HSOH, either known as oxadisulfane or hydrogen thio-peroxide, can be considered a “link molecule” in between the molecules HSSH, disulfane, and HOOH, hydrogen peroxide (see Figure 1.1). The chemical and structural

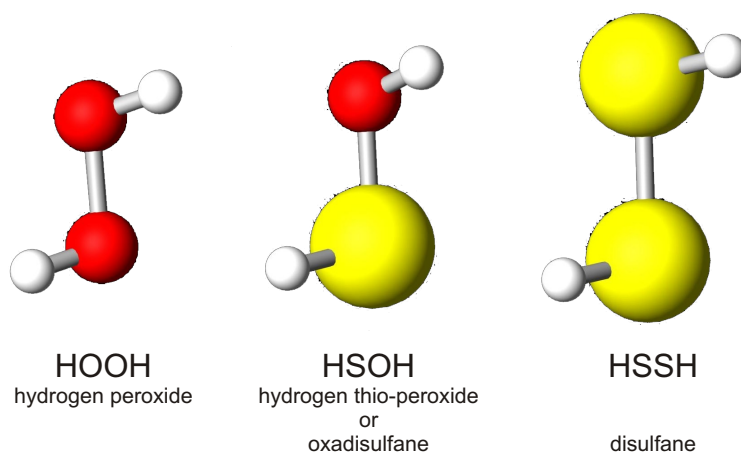


Figure 1.1: The kin molecules HOOH, HSOH, and HSSH.

properties of the brethren molecules HSSH and HOOH are well known to chemists for many decades¹. On the contrary only little information is available for HSOH.

Experimental data on gas-phase HSOH were hampered by the difficulties of its synthesis for a long time and became available only recently [123]. Smardzewski and Lin recorded infrared spectra of products from photolysis of ozone (O_3) and hydrogen sulfide (H_2S) trapped in an argon matrix and they assigned some of the spectral features to vibrational modes of HSOH [105]. Later on, Iraqi and Schwarz detected HSOH via mass spectroscopy

¹See for HOOH: [46, 95, 96, 107] and for HSSH: [11, 16, 40, 47, 121].

in a chemical ionization source from a $\text{H}_2\text{S}/\text{N}_2\text{O}$ gas mixture [64]. However, none of these syntheses were suited for gas-phase detection of HSOH by means of absorption spectroscopy. Winnewisser, Hahn, and co-workers began to hunt down HSOH and it took them at least 15 years of trial and error before the breakthrough came in 2003. Behnke and Hahn [10, 123] found a novel method of producing oxadisulfane in large quantities from flash vacuum pyrolysis of di-*tert*-butyl sulfoxide. The chemical reaction creating HSOH additionally builds many other similar molecules simultaneously. Given those circumstances, synthesizing HSOH and recording its spectrum in the laboratory was not so much like “searching for a needle in a haystack” but rather like “looking for an ant somewhere in Canada”, Behnke said. Nevertheless, this synthesis enables measurements of the rotational spectra of HSOH, and due to extremely precise prognoses based on high level quantum chemical *ab initio* calculations by Gauss *et al.*, Winnewisser *et al.* [123] succeeded in assigning the rotational spectrum of this elusive species.

The molecule HSOH is an asymmetric rotor close to the limiting case of a symmetric prolate top molecule. Therefore the pure rotational and rotational-vibrational spectra of this molecule appear very simple at first glance. However, if the spectra are inspected in detail, the molecule manifests its peculiarities which require the reexamination of some of the basic concepts in vibration-rotation theory.

HSOH, as well as HSSH and HOOH, is one of the most simple examples for a molecule showing chirality. In Figure 1.2 the two stable configurations are shown, they are energetically but not geometrically identical. This means that they are not congruent. One configuration forms the so called

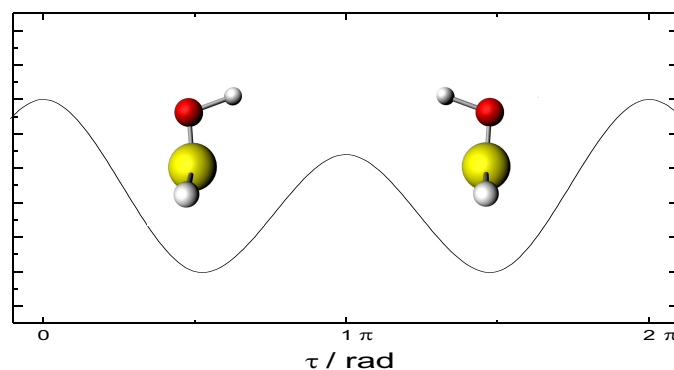


Figure 1.2: The enantiomers of HSOH.

right-handed and the other the left-handed isomer. However, the two isomers cannot be separated. They change their configuration forth and back between right-handed and left-handed by tunneling through the potential

barrier separating the enantiomers².

The tunneling process through the barrier is an internal rotation about the S-O bond in HSOH. Obviously, HSOH is of lower symmetry than HSSH and HOOH. Hence HSOH is not only one of the simplest examples of a molecule showing chirality but with two different rotor moieties, SH and OH, it also represents the most general case of an internally rotating four atomic chain molecule. The recorded transitions of HSOH split into doublets due to the internal rotation tunneling. In order to give an explanation of the observed line splitting it is necessary to extend the period of internal rotation from 2π to 6π , meaning HSOH has not only one left and one right handed isomer but rather six enantiomers.

Furthermore, in the HSOH spectra presented here another new effect of fundamental spectroscopic importance has been observed: The spectra of HSOH exhibit an intensity anomaly. This effect is most probably related to a state-mixing and should be observable in case of all asymmetric top molecules bearing a hindered internal motion and having at least two different dipole moment components. Even though this effect seems to be of general nature it has not been reported so far.

The high frequency stretching modes $\nu(\text{SH})$ and $\nu(\text{OH})$ exhibit entirely different traits of the molecule HSOH. In case of the OH-stretching mode the molecule can be regarded as a fairly rigid “textbook” molecule, displaying unperturbed spectra. On the contrary, the spectra observed in case of the SH stretching mode display a strong potential coupling and hence, identify the limits given by the model of normal modes.

HSOH is not only interesting because of its fundamental spectroscopic importance but it attracts the attention of chemists as well. Sulfur forms a large number of oxoacids, $\text{H}_x\text{S}_y\text{O}_z$. Sulfur oxoacids are widely considered to occur in the formation of pollutants in the Earth’s upper atmosphere [29, 113, 108, 91] and combustion chemistry of sulfur [42]. Most of these compounds are too unstable to be isolated in pure form. Consequently, the physical and chemical properties of these important species are not well-known. The most simple (‘mononuclear’) oxoacids of sulfur are of composition H_2SO_n with n ranging from 1 to 4. For none of these species an experimental equilibrium structure in the gas-phase has been reported, yet. HSOH is the smallest member of oxygen counting sulfur acids and it is the basic molecule exhibiting a S-O single bond. The S-O bond in molecules such as HSO, SO, or SO_2 is known to possess multibond character. Up to date no experimental value for a S-O single bond has been reported. In addition to its role in atmospheric chemistry, there is some evidence, that HSOH is formed in the interstellar medium [33, 34], too.

²That means: mirror images.

The most powerful tool to investigate the structure as well as the dynamics of a molecule is given by means of spectroscopy.

Molecular spectroscopy involves the study of the absorption and emission of electromagnetic radiation by matter; the radiation can be detected directly, or indirectly by its effects on certain molecular properties. The primary purpose of spectroscopic studies is to understand the nature of the nuclear and electronic motions within a molecule.

The different branches of spectroscopy may be classified either in terms of the wavelength, or frequency, of the electromagnetic radiation, or in terms of the type of intramolecular dynamic motion involved as shown in Figure 1.3.

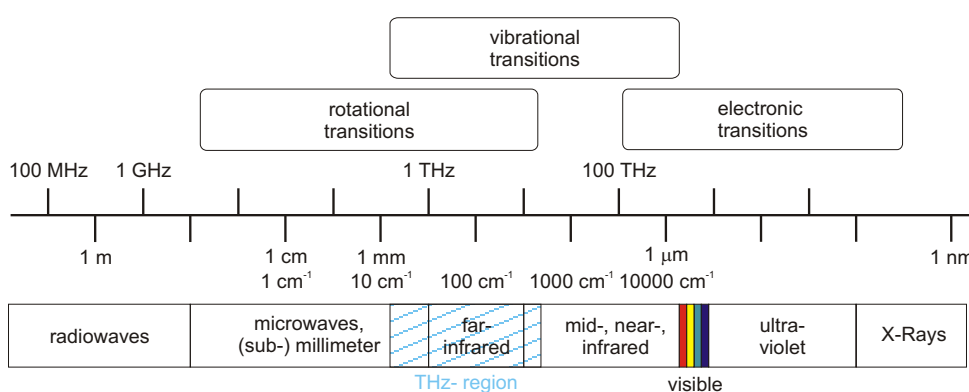


Figure 1.3: Schematic diagram of the electromagnetic spectrum and corresponding interactions of radiation with molecules.

Molecular spectroscopy covers a nominal energy range from 0.0001 cm^{-1} to 100000 cm^{-1} , nine decades in energy, frequency or wavelength. The experimental techniques employed over the full range given in Figure 1.3 are multifarious. In the experimental part of this thesis, spectra in the sub-millimeterwave, THz, and mid-IR region have been recorded by employing quite different experimental setups. Details on the spectrometers introduced are given in Chapter 4 of this thesis.

Molecular spectra arise from electronic, vibrational, and rotational transitions. These motions are not independent from each other, and the complexity of the spectra is increased by the possibility of interactions between them. If they can be analyzed, the information they yield should be correspondingly valuable, it is possible to extract details of molecular dimensions, the strengths of bonds, and the shapes of molecular potential energy curves. The energy associated with rotational transitions is usually lower than that involved in vibrational transitions, which in turn is usually lower than in electronic transitions. As a consequence, although it is possible to observe pure rotational spectra (in the *microwave* region) a vibrational motion is generally accompanied by rotational transitions. A vibrational spectrum (in the *infrared* region) is thus superimposed by a structure due to simultaneous rotational transitions. In an electromagnetic transition both vibrational and

rotational transitions are stimulated and the spectrum (in the *visible* and *ultraviolet* regions) contains information on all of them.

The outline of the present thesis is as follows: The fundamental theoretical concepts related to rotational and vibrational spectroscopy of molecules, as well as introductory information on deriving molecular structures are given in Chapter 2.

This thesis is an example for the fruitful interplay of theoretical and experimental studies and hence, a brief overview on quantum chemical calculations is presented in Chapter 3.

The study of transient molecules requires spectroscopic methods high in sensitivity, resolution, versatility, et cetera. Thus, steady effort is necessary to develop new techniques and to improve existing instruments. In Chapter 4 information on the various experimental setups and spectrometers employed in the experimental part of this thesis are presented.

Chapter 5 deals with the different ways to synthesize the transient species HSOH under laboratory conditions. Besides the well established method of synthesizing the molecule via pyrolysis of di-*tert*-butyl sulfoxide a new production method for the molecule in a *rf*-discharge of water and pure sulfur has been examined. Furthermore, a brief discussion on the possibility of HSOH production in the interstellar medium is given in this chapter as well. The first gas-phase detection of the singly-deuterated oxadisulfane HSOD is presented in Chapter 6. The results of these measurements on HSOD were substantial for the evaluation of an experimental equilibrium structure of HSOH, in Chapter 7.

To get information not only on the structure of this elusive species, but also its dynamics the studies have been extended to the infrared region. The vibrational-rotational spectra recorded in course of this thesis are analyzed in Chapter 8.

Before concluding remarks and prospects are given in Chapter 10, Chapter 9 deals with the subject of internal dynamics in HSOH. New experimental results have been obtained by measurements in the THz-region. These findings identified the limits of theory available at that time and triggered intense theoretical studies on the internal rotation tunneling in this molecule. Furthermore Chapter 9 presents a new, so far unknown, fundamental characteristic of asymmetric top molecules, that possess a barrier to internal rotation tunneling.

2

Theoretical Considerations

In course of this thesis different traits of the elusive species HSOH have been investigated. In the first part of the experimental work pure rotational spectra of the isotopologue HSOD have been recorded and an empirical equilibrium structure of HSOH has been derived. The second part concerns the dynamics of the molecule, i.e. vibrational-rotational spectra as well as rotational-torsional spectra of HSOH have been observed. In the following sections introductory information referring to the theoretical fundamentals of these topics will be given based mainly on textbooks by Gordy and Cook [48], Bernath [15], and Herzberg [59].

2.1 Rotational Spectroscopy

For a rigid body, the classical expression of its rotational kinetic energy is

$$\begin{aligned} E_r &= \frac{1}{2} \vec{\omega}^T \mathbf{I} \vec{\omega} \\ &= \frac{1}{2} I_{xx} \omega_x^2 + \frac{1}{2} I_{yy} \omega_y^2 + \frac{1}{2} I_{zz} \omega_z^2 + I_{xy} \omega_x \omega_y + I_{xz} \omega_x \omega_z + I_{yz} \omega_y \omega_z. \end{aligned} \quad (2.1)$$

x , y , z are its positional coordinates in a rectangular coordinate system fixed in the body with the origin at the center of mass. The moment of inertia tensor \mathbf{I} is defined by

$$\begin{aligned} \mathbf{I} = & \quad I_{xx} \mathbf{e}_x \mathbf{e}_x + I_{xy} \mathbf{e}_x \mathbf{e}_y + I_{xz} \mathbf{e}_x \mathbf{e}_z \\ & + I_{yx} \mathbf{e}_y \mathbf{e}_x + I_{yy} \mathbf{e}_y \mathbf{e}_y + I_{yz} \mathbf{e}_y \mathbf{e}_z \\ & + I_{zx} \mathbf{e}_z \mathbf{e}_x + I_{zy} \mathbf{e}_z \mathbf{e}_y + I_{zz} \mathbf{e}_z \mathbf{e}_z, \end{aligned} \quad (2.2)$$

with

$$\begin{aligned}
 I_{xx} &= \sum_i m_i (y^2 + z^2) \\
 I_{yy} &= \sum_i m_i (z^2 + x^2) \\
 I_{zz} &= \sum_i m_i (x^2 + y^2) \\
 I_{xy} &= I_{yx} = - \sum_i m_i xy \\
 I_{zx} &= I_{xz} = - \sum_i m_i xz \\
 I_{yz} &= I_{zy} = - \sum_i m_i zy,
 \end{aligned} \tag{2.3}$$

where m_i is the mass of a particular particle. According to common mechanics, it is always possible to choose the coordinate axes in such way that off-diagonal elements vanish, leaving only diagonal elements. Those are called the principal moments of inertia and principal axes, respectively. When the notation a , b , and c represents the principal axes system, equation (2.1) becomes

$$\begin{aligned}
 E_r &= \frac{1}{2} I_a \omega_a^2 + \frac{1}{2} I_b \omega_b^2 + \frac{1}{2} I_c \omega_c^2 \\
 &= \frac{1}{2} \left(\frac{J_a^2}{I_a} + \frac{J_b^2}{I_b} + \frac{J_c^2}{I_c} \right),
 \end{aligned} \tag{2.4}$$

where $J_{a,b,c}$ represent the components of the total angular momentum vector \mathbf{J} . According to a common convention in spectroscopy, it is

$$I_a \leq I_b \leq I_c. \tag{2.5}$$

There are six different ways to relate the x, y, z axes with the a, b, c axes (see Table 2.1). Though the choice of the identification is arbitrary, in certain

Table 2.1: Identification of the a, b, c axes with the x, y, z axes.

	I^r	Π^r	III^r	I^l	Π^l	III^l
x	b	c	a	c	a	b
y	c	a	b	b	c	a
z	a	b	c	a	b	c

Superscripts r and l denote the right- and left-handed orientations of the a, b, c axes (orientation is based on the corresponding identification of the principal axes with the z axis).

cases one identification may be more convenient than another.

Generally, molecules are classified according to their principal moments of inertia. There are five cases:

1. Linear molecules: $I_b = I_c, I_a = 0$,
2. Spherical tops: $I_a = I_b = I_c$,
3. Prolate symmetric tops: $I_a < I_b = I_c$,
4. Oblate symmetric tops: $I_a = I_b < I_c$,
5. Asymmetric tops: $I_a < I_b < I_c$.

In the scope of this work, an asymmetric top molecule close to the limit of a symmetric top¹ has been studied. For this reason both, the theory of a symmetric and an asymmetric top, are briefly discussed in the following.

2.1.1 Symmetric Top Molecules

A molecule in which at least two of the principal moments of inertia are equal is called a symmetric top. The special case in which one of the moments of inertia is zero while the other two are equal yields for all linear molecules.

In a symmetric top, one of the principal moments of inertia must lie along the molecular axis of symmetry. The principal moments of inertia along the other two principal axes perpendicular to the axis of symmetry are equal. If a -the axis of the smallest moment of inertia ($I_a < I_b = I_c$)- lies along the symmetry axis, the molecule is a prolate symmetric top. If c -the axis of the largest moment of inertia ($I_a = I_b < I_c$)- lies along the symmetry axis, the molecule is an oblate symmetric rotor.

Rigid Symmetric Rotor

The classical expression for a rigid symmetric top is

$$\begin{aligned} E_r &= \frac{1}{2} \left(\frac{J_a^2}{I_a} + \frac{J_b^2}{I_b} + \frac{J_c^2}{I_c} \right) \\ &= \frac{J_a^2}{2I_a} + \frac{1}{2I_b} (J_b^2 + J_c^2) \quad (\text{prolate top}) \end{aligned} \quad (2.6)$$

or

$$= \frac{1}{2I_b} (J_a^2 + J_b^2) + \frac{J_c^2}{2I_c} \quad (\text{oblate top}). \quad (2.7)$$

¹Also called: accidentally symmetric top.

Since in this work an accidentally prolate symmetric top was studied, the treatment will be limited to a prolate top. Nevertheless the results also apply to an oblate top by interchanging labels a and c .

With

$$J^2 = J_a^2 + J_b^2 + J_c^2 \quad (2.8)$$

one obtains

$$E_r = \frac{1}{2I_b} J^2 + \left(\frac{1}{2I_a} - \frac{1}{2I_b} \right) J_a^2. \quad (2.9)$$

The corresponding quantum mechanical Hamiltonian is

$$\mathcal{H} = \frac{1}{2I_b} \hat{J}^2 + \left(\frac{1}{2I_a} - \frac{1}{2I_b} \right) \hat{J}_a^2. \quad (2.10)$$

\hat{J} is the operator of total angular momentum. \hat{J}^2 , \hat{J}_Z (projection of \hat{J} onto the space-fixed cartesian axes X , Y , and Z), and \hat{J}_z (projection of \hat{J} onto the molecule-fixed axes system x , y , and z) all commute with \mathcal{H} , so that a set of simultaneous eigenfunctions $\psi = |JKM\rangle$ can be found, as

$$\begin{aligned} \mathcal{H} |JKM\rangle &= E |JKM\rangle \\ \hat{J}^2 |JKM\rangle &= J(J+1) \hbar^2 |JKM\rangle \\ \hat{J}_Z |JKM\rangle &= M \hbar |JKM\rangle \\ \hat{J}_z |JKM\rangle &= K \hbar |JKM\rangle, \end{aligned} \quad (2.11)$$

with quantum numbers

$$\begin{aligned} J &= 0, 1, 2, 3, \dots \\ M &= 0, \pm 1, \pm 2, \pm 3, \dots, \pm J \\ K &= 0, \pm 1, \pm 2, \pm 3, \dots, \pm J. \end{aligned} \quad (2.12)$$

The symmetric top wavefunctions $|JKM\rangle^2$ are of the form:

$$|JKM\rangle = \left[\frac{2J+1}{8\pi^2} \right]^{1/2} e^{iM\phi} d_{MK}^{(J)}(\theta) e^{iK\chi}, \quad (2.13)$$

where ϕ , θ , χ are the Euler-angles³ and the $d_{MK}^{(J)}$ functions are hypergeometric functions of $\sin^2(\theta/2)$. They are also related to the rotational matrices of the angular momentum.

²see e.g. [134]

³The orientation of the molecular system with respect to the laboratory system is described by the three Euler-angles ϕ , θ , and χ (see e.g.[21])

With equations (2.10) and (2.11) one gets

$$\begin{aligned} \mathcal{H} |JKM\rangle &= E |JKM\rangle \\ \left[\frac{1}{2I_b} \hat{J}^2 + \left(\frac{1}{2I_a} - \frac{1}{2I_b} \right) \hat{J}_a^2 \right] |JKM\rangle &= \\ &= \left[\frac{\hbar^2}{2I_b} J(J+1) + \left(\frac{\hbar^2}{2I_a} - \frac{\hbar^2}{2I_b} \right) K^2 \right] |JKM\rangle \end{aligned} \quad (2.14)$$

and thus for the term values

$$E(J, K_a)_{prolate} = BJ(J+1) + (A - B)K_a^2 \quad (\text{prolate top}), \quad (2.15)$$

or

$$E(J, K_c)_{oblate} = BJ(J+1) + (C - B)K_c^2 \quad (\text{oblate top}). \quad (2.16)$$

Here K_a , and K_c respectively, are the quantum numbers corresponding to the projection of \hat{J} onto the symmetry axis of the molecule. The rotational constants A , B , and C are defined in energy units (Joules) by

$$A = \frac{\hbar^2}{2I_a}, \quad (2.17)$$

$$B = \frac{\hbar^2}{2I_b}, \quad (2.18)$$

$$C = \frac{\hbar^2}{2I_c}. \quad (2.19)$$

States only differing in sign of K , have the same energy (due to the term K^2 in the energy expressions (2.15) and (2.16)), they correspond to the two opposite directions of rotation about the symmetry axis. As a consequence, all states with $K > 0$ are doubly degenerated. In addition to the K degeneracy there is a $(2J + 1) M$ degeneracy in the field free symmetric rotor. The M degeneracy can be lifted by the application of an external electric or magnetic field which would have to be treated as additional term in the Hamiltonian.

Centrifugal Distortion

In the previous section the rotors nuclear framework was regarded as rigid. However, in real life, the nuclei are held together by finite restoring forces. Centrifugal stretching is treated as a perturbation on the eigenstates of the rigid rotor. If \mathcal{H}_r represents the Hamiltonian of the rigid rotor and \mathcal{H}_d that corresponding to the distortional energy, the rotational Hamiltonian is given by

$$\mathcal{H} = \mathcal{H}_r + \mathcal{H}_d. \quad (2.20)$$

\mathcal{H}_d has the form

$$\mathcal{H}_d = \frac{\hbar^4}{4} \sum_{\alpha\beta\gamma\delta} \tau_{\alpha\beta\gamma\delta} \hat{J}_\alpha \hat{J}_\beta \hat{J}_\gamma \hat{J}_\delta. \quad (2.21)$$

$\tau_{\alpha\beta\gamma\delta}$ are the centrifugal distortion constants

$$\tau_{\alpha\beta\gamma\delta} = -\frac{1}{2} \sum_{ij} \mu_{\alpha\beta}^{(i)} (k^{-1})_{ij} \mu_{\gamma\delta}^{(j)}, \quad (2.22)$$

where $(k^{-1})_{ij}$ describes an element of the matrix, inverse to the matrix force constants k_{ij} . $\mu_{\alpha\beta}^{(i)}$ is a component of the reciprocal moment of inertia tensor. In equations (2.21) and (2.65) $\alpha, \beta, \gamma, \delta$ represent the principal coordinate axes of the moments of inertia. $\hat{J}_{\alpha,\beta,\gamma,\delta}$ are the components of the total angular momentum. In case of a symmetric top it can be shown⁴ that in first order approximation it is possible to simplify equation (2.21) resulting in the expression

$$E_d^{(1)} = D_J J^2 (J+1)^2 + D_{JK} J (J+1) K^2 + D_K K^4. \quad (2.23)$$

Here D_J , D_{JK} , and D_K are the first order centrifugal stretching constants of the symmetric top molecule.

Selection Rules

The derivation of selection rules for a symmetric top is somewhat involved since the transformation from the laboratory to the molecular frame needs to be considered. A detailed derivation can be found for example in the textbook by Gordy and Cook [48].

In a true symmetric top, any permanent dipole moment $\vec{\mu}$ must of necessity point along the symmetry axes (*molecular frame*). All matrix elements of the transition dipole moment

$$\mathbf{M} = \int \langle J' K' M' | \vec{\mu} | J'' K'' M'' \rangle d\tau \quad (2.24)$$

along a space fixed axis (*laboratory frame*) vanish except for those transitions respecting the selection rules $\Delta J = \pm 1$, $\Delta M = 0, \pm 1$, and $\Delta K = 0$. Because of $\Delta K = 0$ the transitions are confined to lie within a K -stack given by

$$\nu_{J+1, K \leftarrow J, K} = 2B(J+1) - 4D_J(J+1)^3 - 2D_{JK}(J+1)K^2. \quad (2.25)$$

⁴see e.g. reference [48].

2.1.2 Asymmetric Top Molecules

In case of the asymmetric top molecule, none of its three principal moments of inertia is zero and no two are equal. In contrast to linear or symmetric top molecules, the rotational frequencies can no longer be expressed by convenient equations. Even if centrifugal and distortion effects are neglected, only for certain low J values the energy levels of the asymmetric rotor can be expressed in closed form.

In an asymmetric rotor no internal component of the angular momentum is constant to the motion. For this reason the projection \hat{J}_z no longer commutes with \mathcal{H} and only J and M are “good” quantum numbers. Pseudo quantum numbers (customarily designated by subscripts on J) are employed in labelling the energy levels. For this presentation the double subscript system of King *et al.* [72] is used. Their system is best understood by correlating the limiting prolate and oblate symmetric tops. Let the three principal moments of inertia of an asymmetric top be in the conventional order: $I_a < I_b < I_c$. The energies of prolate ($I_b = I_c$) and oblate ($I_a = I_b$) symmetric tops are given by equations (2.15) and (2.16). These levels are plotted to the extreme left and right of Figure 2.1. As is typical for correlation diagrams, the energy levels are not to scale and the lines connecting the prolate with the oblate levels correspond to a hypothetical distortion of a molecule from a prolate to an oblate top. The levels are labelled by J_{K_a, K_c} where J is a good quantum num-

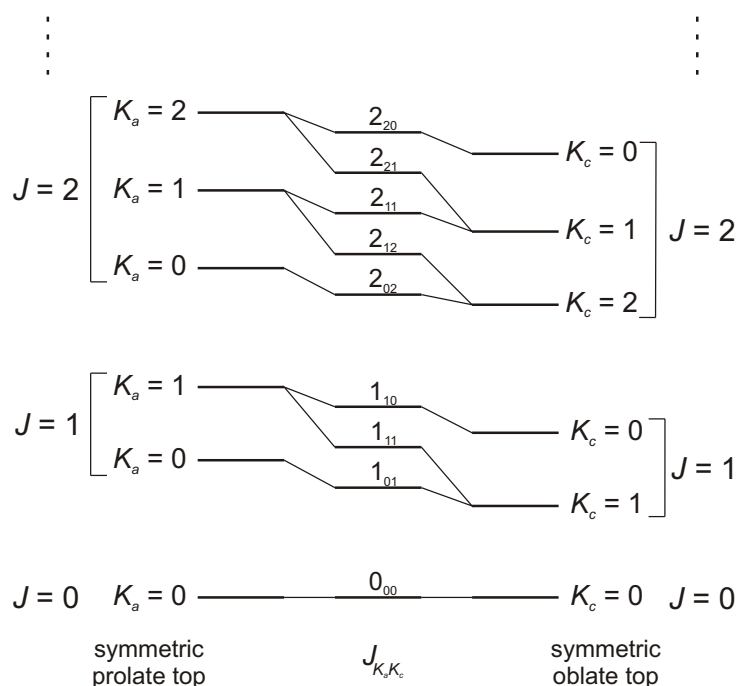


Figure 2.1: Correlation diagram of the asymmetric rotor energy levels. The limiting cases of the prolate and oblate symmetric top are plotted to the left and right, respectively.

ber, but K_a and K_c are just labels for the asymmetric top. The degree of asymmetry can be quantified by “Ray’s”-asymmetry parameter κ :

$$\kappa = \frac{2B - A - C}{A - C}. \quad (2.26)$$

A , B , and C are the rotational constants (see equations (2.17)–(2.19)). The limiting values for κ , -1 and $+1$, correspond to the prolate and oblate symmetric tops, while the most asymmetric top reaches $\kappa = 0$.

Rigid Asymmetric Rotor

The rigid asymmetric rotor’s Hamiltonian is given by

$$\mathcal{H} = \frac{\hat{J}_a^2}{2I_a} + \frac{\hat{J}_b^2}{2I_b} + \frac{\hat{J}_c^2}{2I_c}. \quad (2.27)$$

As mentioned before, the Schrödinger equation for the asymmetric top has no general analytical solution and therefore must be solved numerically using a symmetric top basis set. For convenience, the form of the terms in the Hamiltonian is changed by introducing the raising operator (in I' representation) $\hat{J}_- = \hat{J}_b - i\hat{J}_c$ and the lowering operator $\hat{J}_+ = \hat{J}_b + i\hat{J}_c$:

$$\begin{aligned} \hat{J}_+ |JKM\rangle &= \hbar [J(J+1) - K(K-1)]^{\frac{1}{2}} |J(K-1)M\rangle \\ \hat{J}_- |JKM\rangle &= \hbar [J(J+1) - K(K+1)]^{\frac{1}{2}} |J(K+1)M\rangle \end{aligned} \quad (2.28)$$

Let A , B , C be given, according to equations (2.17)–(2.19), so that

$$\begin{aligned} \hbar^2 \mathcal{H} &= A\hat{J}_a^2 + B\hat{J}_b^2 + C\hat{J}_c^2 \\ &= \left(\frac{B+C}{2}\right) (\hat{J}_b^2 + \hat{J}_c^2) + A\hat{J}_a^2 + \left(\frac{B-C}{2}\right) (\hat{J}_b^2 - \hat{J}_c^2) \\ &= \left(\frac{B+C}{2}\right) \hat{J}^2 + \left(A - \frac{B+C}{2}\right) \hat{J}_a^2 + \left(\frac{B-C}{4}\right) (\hat{J}_+^2 + \hat{J}_-^2). \end{aligned} \quad (2.29)$$

The Distortable Rotor

The classical Hamiltonian \mathcal{H}_d for the distortional energy of a semirigid non-vibrating molecule is given by equation (2.21). In the case of symmetric top molecules it is possible to simplify this equation significantly (see equation (2.23)), unfortunately, an analogous simplification is impossible for the asymmetric rotor. Watson [116] has shown that a maximum of five quartic centrifugal distortion constants can be determined from experimentally observed spectra. Therefore a reduced Hamiltonian has to be employed.

A-reduced Hamiltonian Considering centrifugal distortion effects up to the sixth order in rotational angular momentum, Watson [115] introduced a reduced Hamiltonian $\mathcal{H}^{(A)}$ of the form

$$\mathcal{H}^{(A)} = \mathcal{H}_r + \mathcal{H}_d^{(4)} + \mathcal{H}_d^{(6)} \quad (2.30)$$

with

$$\begin{aligned} \mathcal{H}_r &= B_x \hat{J}_x^2 + B_y \hat{J}_y^2 + B_z \hat{J}_z^2 \\ &= \left(\frac{B_x + B_y}{2} \right) \hat{J}^2 + \left(B_z - \frac{B_x + B_y}{2} \right) \hat{J}_z^2 + \left(\frac{B_x - B_y}{2} \right) (\hat{J}_x^2 - \hat{J}_y^2) \end{aligned} \quad (2.31)$$

$$\begin{aligned} \mathcal{H}_d^{(4)} &= \Delta_J \hat{J}^4 - \Delta_{JK} \hat{J}^2 \hat{J}_z^2 - \Delta_K \hat{J}_z^4 \\ &\quad - 2\delta_J \hat{J}^2 (\hat{J}_x^2 - \hat{J}_y^2) - \delta_K [\hat{J}_z^2 (\hat{J}_x^2 - \hat{J}_y^2) + (\hat{J}_x^2 - \hat{J}_y^2) \hat{J}_z^2] \end{aligned} \quad (2.32)$$

$$\begin{aligned} \mathcal{H}_d^{(6)} &= \Phi_J \hat{J}^6 + \Phi_{JK} \hat{J}^4 \hat{J}_z^2 + \Phi_{KJ} \hat{J}_z^2 \hat{J}^4 + \Phi_K \hat{J}_z^6 \\ &\quad + 2\phi_J \hat{J}^4 (\hat{J}_x^2 - \hat{J}_y^2) \\ &\quad + \phi_{JK} \hat{J}^2 [\hat{J}_z^2 (\hat{J}_x^2 - \hat{J}_y^2) + (\hat{J}_x^2 - \hat{J}_y^2) \hat{J}_z^2] \\ &\quad + \phi_K [\hat{J}_z^4 (\hat{J}_x^2 - \hat{J}_y^2) + (\hat{J}_x^2 - \hat{J}_y^2) \hat{J}_z^4] \end{aligned} \quad (2.33)$$

where

B_x, B_y, B_z : rotational constants⁵

$\hat{J}_x, \hat{J}_y, \hat{J}_z$: operators of the components
of the angular momentum

$\Delta_J, \Delta_{JK}, \Delta_K, \delta_J, \delta_K$: quartic distortion coefficients

$\Phi_J, \Phi_{JK}, \Phi_{KJ}, \Phi_K, \phi_J, \phi_{JK}, \phi_K$: sextic distortion coefficients.

Note that \hat{J}_z^2 and $(\hat{J}_x^2 - \hat{J}_y^2)$ do not commute. There exist a direct connection between the distortion coefficients of the reduced Hamiltonian and the centrifugal distortion constants τ in equation (2.21). The correlation for conversion can be found in [48].

S-reduced Hamiltonian In a complete analysis, the choice of the five quartic centrifugal distortion constants can be made in an infinite number of ways. At first Carpenter [24] pointed out that a judicious choice of representation is important. This situation will occur when the molecule is accidentally very close to a symmetric top. For this reason, an alternate reduction of $\mathcal{H}_d^{(4)}$ has been proposed by Winnewisser [122] and Van Eijck [136]. Typke [109] extended the results to $\mathcal{H}_d^{(6)}$ and demonstrated that a more satisfying analysis can be obtained for slightly asymmetric tops with the following reduction

$$\mathcal{H}^{(S)} = \mathcal{H}_r + \mathcal{H}_d^{(4)} + \mathcal{H}_d^{(6)} \quad (2.34)$$

⁵Employing the I' representation the rotational constants $B_x, B_y,$ and B_z stand for $B, C,$ and $A,$ respectively.

with

$$\begin{aligned}\mathcal{H}_r &= B_x \hat{J}_x^2 + B_y \hat{J}_y^2 + B_z \hat{J}_z^2 \\ &= \left(\frac{B_x + B_y}{2} \right) \hat{J}^2 + \left(B_z - \frac{B_x + B_y}{2} \right) \hat{J}_z^2 + \left(\frac{B_x - B_y}{4} \right) (\hat{J}_+^2 + \hat{J}_-^2)\end{aligned}\quad (2.35)$$

$$\begin{aligned}\mathcal{H}_d^{(4)} &= -D_J \hat{J}^4 - D_{JK} \hat{J}^2 \hat{J}_z^2 - D_K \hat{J}_z^4 \\ &\quad + d_1 \hat{J}^2 (\hat{J}_+^2 + \hat{J}_-^2) + d_2 (\hat{J}_+^4 + \hat{J}_-^4)\end{aligned}\quad (2.36)$$

$$\begin{aligned}\mathcal{H}_d^{(6)} &= H_J \hat{J}^6 + H_{JK} \hat{J}^4 \hat{J}_z^2 + H_{KJ} \hat{J}^2 \hat{J}_z^4 + H_K \hat{J}_z^6 \\ &\quad + h_1 \hat{J}^4 (\hat{J}_+^2 + \hat{J}_-^2) + h_2 \hat{J}^2 (\hat{J}_+^4 + \hat{J}_-^4) + h_3 (\hat{J}_+^6 + \hat{J}_-^6)\end{aligned}\quad (2.37)$$

where

$$\begin{aligned}B_x, B_y, B_z &: \text{rotational constants}^5 \\ \hat{J}_z &: \text{operator of the } z\text{-component} \\ &\quad \text{of the angular momentum} \\ \hat{J}_+, \hat{J}_- &: \text{lowering and raising operator} \quad (2.38) \\ D_J, D_{JK}, D_K, d_1, d_2 &: \text{quartic distortion coefficients} \\ H_J, H_{JK}, H_{KJ}, H_K, h_1, h_2, h_3 &: \text{sextic distortion coefficients.}\end{aligned}$$

The coefficients in $\mathcal{H}^{(S)}$ and $\mathcal{H}^{(A)}$ can be related to each other (see Table 2.2) and the coefficients of the two reduced Hamiltonians provide the same information.

Table 2.2: Relations between the distortion coefficients of the A and S reduced Hamiltonians^a

$B_x^{(A)} = B_x^{(S)} - 4(2\sigma + 1)d_2$	$B_y^{(A)} = B_y^{(S)} + 4(2\sigma - 1)d_2$	$B_z^{(A)} = B_z^{(S)} + 10d_2$
$\Delta_J = D_J - 2d_2$	$\Delta_{JK} = D_{JK} + 12d_2$	$\Delta_K = D_K - 10d_2$
$\delta_J = -d_1$	$\delta_K = -4\sigma d_2$	
$\Phi_J = H_J + 2h_2$	$\Phi_{JK} = H_{JK} - 12h_2 + 16\sigma h_3$	
$\Phi_{KJ} = H_{KJ} + 10h_2 - (160\sigma/3)h_3$		$\Phi_k = H_K + (112\sigma/3)h_3$
$\phi_J = h_1 + h_3$		
$\phi_{JK} = 4\sigma h_2 - 10h_3 - 8d_2(D_{JK} + 2\sigma d_1 + 4d_2) / (B_x - B_y)$		
$\phi_K = (32\sigma^2/3 + 9)h_3 - 16d_2(D_K + 2(\sigma^2 - 2)d_2) / (B_x - B_y)$		
^a $\sigma = (2B_z - B_x - B_y) / (B_x - B_y)$ See reference [114]		

Selection Rules

The allowed changes in J for dipole absorption are $\Delta J = 0, \pm 1$. This has to be expected since the asymmetric rotor wave functions are expressed in form of linear combinations of symmetric wave functions. In addition to this selection rule for J , there are restrictions on changes that occur in the subscripts of J , in the pseudo quantum numbers. In general, an arbitrary molecule has three dipole moment components μ_a , μ_b , and μ_c along the principal axes. Each nonvanishing dipole moment component allows for a certain set of transitions and leads to an additional set of selection rules for K_a and K_c as summarized in Table 2.3.

The common notation for groups of transitions (*sub-bands*) occurring in the spectrum is:

$$\Delta K \Delta J_{K''} \text{ -band} \quad (2.39)$$

with $\Delta J = -1, 0$, and $+1$ is related to the characters P , Q , and R , respectively; while $\Delta K = -1, 0$, and $+1$ is related to p , q , and r , respectively. K'' stands for the quantum number K of the lower energy state.

Table 2.3: Selection rules for asymmetric top molecules.

Dipole component	ΔK_a	ΔK_c
along a -axis, a -type	0 ($, \pm 2, \pm 4, \dots$)	± 1 ($, \pm 3, \pm 5, \dots$)
along b -axis, b -type	± 1 ($, \pm 3, \pm 5, \dots$)	± 1 ($, \pm 3, \pm 5, \dots$)
along c -axis, c -type	± 1 ($, \pm 3, \pm 5, \dots$)	0 ($, \pm 2, \pm 4, \dots$)

Transitions in brackets are much weaker than the main ones.

2.1.3 Spectral line intensities

The transition dipole moment $\vec{\mu}$ is a theoretical quantity, but how is it related to the measured intensity of a spectral line? The basic relation is the *Lambert-Beer* law:

$$I_l = I_0 e^{-\alpha C l} \quad (2.40)$$

relating the intensities of the light before (I_0) and after (I_l) it has passed through a length l of a sample of absorbing species at a concentration C . The frequency dependent quantity α is the absorption coefficient and can be measured by forming $\ln(I_l/I_0)$. The product $A = \alpha C l$ is called the absorbance of the sample. The absorption coefficient and the absorbance depend on the frequency of the incident light. The total intensity of the transition is obtained as the integral of the absorption coefficient over the entire range of frequencies it spans. Therefore the integrated absorption coefficient

$$\mathcal{A} = \int \alpha \nu \quad (2.41)$$

is

$$\mathcal{A} = \frac{\pi\nu_{fi}}{3\epsilon_0\hbar c}L|\vec{\mu}_{fi}|^2, \quad (2.42)$$

which is a direct link between the measurable quantity \mathcal{A} and the calculable quantity $\vec{\mu}$. ν_{fi} is the exact frequency related to a transition between an initial state i and a final state f , while $\vec{\mu}_{fi}$ is the corresponding transition dipole moment.⁶

⁶A detailed derivation of the Lambert-Beer law, as well as the integrated absorption coefficient \mathcal{A} is given e.g. in the textbook by Atkins [5]

2.2 Vibrational Spectroscopy

The vibration of polyatomic molecules affects the entire molecule. The potential energy of a polyatomic molecule depends on every displacement of each atom from its equilibrium position. Therefore, to express the actual potential energy of the molecule in terms of all displacements ξ_i from the equilibrium, one receives

$$V = V(0) + \sum_i \left(\frac{\partial}{\partial \xi_i} V \right)_0 \xi_i + \frac{1}{2} \sum_{i,j} \left(\frac{\partial^2}{\partial \xi_i \partial \xi_j} V \right)_0 \xi_i \xi_j + \dots \quad (2.43)$$

The subscript 0 denotes that the derivatives are evaluated at the equilibrium configuration. The constant $V(0)$ may be set to zero and the first derivatives all equal zero at $\xi = 0$. This discussion is based on the harmonic approximation for the potential energy, neglecting terms in the expansion (2.43) with powers higher than two. Therefore

$$V = \frac{1}{2} \sum_{i,j} k_{ij} \xi_i \xi_j, \quad (2.44)$$

with k_{ij} being

$$k_{ij} = \left(\frac{\partial^2}{\partial \xi_i \partial \xi_j} V \right)_0 \quad (2.45)$$

is a generalized force constant. Not all displacements ξ_i correspond to vibrations. In a polyatomic molecule there are $3N$ independent displacements of the N atoms it is built from. Three of these displacements (or three linear combinations of them) are simply translations of the entire unit in the x , y , or z direction. Three other ones (two in case of a linear molecule) correspond to rotational displacements about three mutually perpendicular axes passing through the center of mass of the molecule. Therefore, of the $3N$ displacements overall, only $3N - 6$ ($3N - 5$ for linear species) correspond to vibrational displacements, where one part of the molecule moves relative to some other part. Hence six (or five) displacements in equation (2.44) do not affect the potential energy of the molecule; the generalized force constants are zero for the translation and rotation. The form of the potential in equation (2.44) also reflects the way that a vibration in one part of the molecule (i.e. displacement i) may affect a vibration elsewhere (i.e. displacement j) because the potential depends on both displacements: k_{ij} links displacements and that way couples together vibrations.

In the following the theoretical treatment of vibrational spectroscopy is reduced on asymmetric top molecules and therefore $3N - 6$ displacements correspond to vibrational displacements.

2.2.1 Normal Coordinates of Vibration

Instead of treating the vibrational problem in the representation of the $3N$ coordinates ξ_i , it is often more convenient to work with $3N - 6$ independent

internal vibration coordinates Q_i corresponding to the vibrational degrees of freedom of the molecule. As a first step to simplify the problem, mass-weighted coordinates q_i are introduced

$$q_i = \sqrt{m_i} \xi_i. \quad (2.46)$$

Here m_i is the mass of the atom displaced by ξ_i . The potential energy becomes

$$V = \frac{1}{2} \sum_{i,j} K_{ij} q_i q_j, \quad K_{ij} = \left(\frac{1}{m_i m_j} \right)^{\frac{1}{2}} \cdot k_{ij} = \left(\frac{\partial}{\partial q_i \partial q_j} V \right)_0, \quad (2.47)$$

the kinetic energy

$$T = \frac{1}{2} \sum_i m_i \dot{\xi}_i^2 = \frac{1}{2} \sum_i \dot{q}_i^2, \quad (2.48)$$

and the total energy

$$E = \frac{1}{2} \sum_i \dot{q}_i^2 + \frac{1}{2} \sum_{i,j} K_{ij} q_i q_j. \quad (2.49)$$

The non-trivial quantities in the potential energy are the cross terms ($i \neq j$). Thus, the question arises whether it is possible to find linear combinations Q_i of the mass-weighted coordinates q_i so that the total energy can be written in the form

$$E = \frac{1}{2} \sum_i \dot{Q}_i^2 + \sum_i \kappa_i Q_i^2 \quad (2.50)$$

without cross terms. Linear combinations of this type, the *normal coordinates*, do exist⁷. Thus, both the kinetic and the potential energy terms have no cross terms connecting different coordinates. The system therefore behaves like a set of $3N - 6$ independent harmonic oscillators, each oscillating without interaction with the others.

However, a real system has cubic, quartic, and higher terms in its potential energy expansion. For a real molecule the normal coordinates are still defined in the previous mentioned way, using only the harmonic terms. But because the real potential is anharmonic, it is impossible to completely uncouple the resulting $3N$ differential equations. The anharmonic terms in the potential energy expansion are then said to couple the normal modes, so that the normal mode approximation is not completely valid (see Section 8.2).

2.2.2 Quantum Mechanical Description

The classical expression for the total energy (equation (2.49)) consists of a sum of terms. The Hamiltonian is constructed in the same way

$$\mathcal{H} = \sum_i \mathcal{H}_i, \quad \mathcal{H}_i = -\frac{\hbar^2}{2} \frac{\partial^2}{\partial Q_i^2} + \frac{1}{2} \kappa_i Q_i^2. \quad (2.51)$$

⁷For a detailed description on deriving normal coordinates the textbooks by Bernath [15], Herzberg [59] as well as Papoušek and Aliev [92] are recommended.

The entire molecule's wavefunction is therefore also factorizable into a product of wavefunctions for each mode

$$\psi = \psi_{v_1}(Q_1) \cdot \psi_{v_2}(Q_2) \dots, \quad (2.52)$$

with $3N - 6$ factors for a polyatomic molecule composed of N atoms. Each factor satisfies the stationary Schrödinger equation

$$\begin{aligned} \mathcal{H}_i \psi(Q_i) &= E \psi(Q_i), & \text{or} \\ -\frac{\hbar^2}{2} \frac{\partial^2}{\partial Q_i^2} \psi + \frac{1}{2} \kappa_i Q_i^2 \psi &= E \psi \end{aligned} \quad (2.53)$$

which is the Schrödinger equation for a harmonic oscillator of unit mass undergoing vibration along the coordinate Q_i . Therefore the energies and eigenfunctions for each mode are

$$\begin{aligned} E &= \left(v_i + \frac{1}{2} \right) \hbar \omega_i, & \omega_i &= \sqrt{\kappa_i}; & v_i &= 0, 1, 2, \dots \\ \psi_i &= C_{v_i} H_{v_i}(y_i) e^{-\frac{1}{2} y_i^2}, & y_i &= \left(\frac{\omega_i}{\hbar} \right)^{\frac{1}{2}} Q_i, \end{aligned} \quad (2.54)$$

with C_{v_i} being a normalization constant and H_{v_i} the Hermite polynomials. Hence, the total vibrational energy of a molecule is

$$E = \sum_i \left(v_i + \frac{1}{2} \right) \hbar \omega_i, \quad i = 1, 2, \dots, (3N - 6) \text{ or } (3N - 5) \quad (2.55)$$

and the total wavefunction is the product of the wavefunctions given in equation (2.54). The minimum vibrational energy of a molecule is the sum of the zero-point energies of all modes

$$E_0 = \frac{\hbar}{2} \sum_i \omega_i. \quad (2.56)$$

2.2.3 Selection Rules

According to classical electrodynamics any motion of an atomic system connected to a change of its dipole moment leads to emission or absorption of radiation. During the vibrational motion of a molecule the charge distribution undergoes a periodic change, and therefore generally the dipole moment changes periodically. Since, in the harmonic oscillator approximation, any vibrational motion of the molecule may be resolved into a sum of normal vibrations with appropriate amplitudes, and since the normal modes are the only simple periodic motions, the normal frequencies are those that are emitted or absorbed by the molecule.

Normal vibrations that are connected to a change of dipole moment and, thus, appear in the infrared are called *infrared active*. Vibrations for which the change of charge distribution (which always occur) is such that no change

of dipole moment arises and which, therefore, do not appear in the infrared, are called *infrared inactive*.

In molecules without any geometrical symmetry, every normal vibration is connected to a change of dipole moment; and therefore, all normal vibrations are infrared active. Only in symmetrical molecules there may be vibrations during which the change of dipole moment is exactly zero and which are infrared inactive, hence.

As a direct consequence, the selection rules for the electric dipole transitions of a harmonic oscillator are $\Delta v = \pm 1$, and each normal mode satisfies the same selection rule independently. If anharmonic wavefunctions are used, transitions with $\Delta v = \pm 2, \pm 3, \dots$ also become allowed because each anharmonic wavefunction can be represented by an expansion of harmonic oscillator wavefunctions.

The various types of infrared transitions have are associated to specific names: Any $v = 1 \leftarrow 0$ transition is called *fundamental*, while any transition with $v'' \neq 0$ is called *hot band*. The *first overtone* is the $v = 2 \leftarrow 0$ transition, the *second overtone* has $v = 3 \leftarrow 0$, and so on. Transitions in which the quantum numbers change simultaneously in two or more modes are called *combination bands*.

2.2.4 Anharmonicities

As mentioned before, the concept of normal vibrations is based on the assumption of sufficiently small amplitudes of the oscillations (i.e., infinitesimal amplitudes). In this case only the quadratic terms in the potential energy need to be considered. Actually the amplitudes of the quantized oscillations, though usually small, are not infinitesimal and therefore (for accurate calculations) cubic, quartic, and higher terms of the form

$$V_{\text{anharmonic}} = \left(\frac{1}{3!}\right) \sum_{i,j,k} \left(\frac{\partial^3}{\partial q_i \partial q_j \partial q_k} V\right)_0 q_i q_j q_k + \left(\frac{1}{4!}\right) \sum_{i,j,k,l} \left(\frac{\partial^4}{\partial q_i \partial q_j \partial q_k \partial q_l} V\right)_0 q_i q_j q_k q_l + \dots \quad (2.57)$$

have to be considered in the potential energy.

The presence of these terms nullify the independence of the normal modes of vibration, because although the quadratic part of the potential can be diagonalized, the normal coordinates do not simultaneously diagonalize the cubic and higher orders. Therefore the Hamiltonian does not separate, and the wavefunctions consequently do not factorize into independent components, one for each mode.

Energy Levels

Taking into account cross terms and using wavenumber units (cm^{-1}) for the vibrational energy, one receives

$$G(v_1, v_2, \dots) = \sum_i \omega_i \left(v_i + \frac{1}{2} \right) + \sum_i \sum_{k \geq i} x_{ik} \left(v_i + \frac{1}{2} \right) \left(v_k + \frac{1}{2} \right) + \dots \quad (2.58)$$

Here ω_i are the frequencies (in cm^{-1}) of the infinitesimal amplitudes of the $3N - 6$ normal vibrations. The x_{ik} are the anharmonicity constants, and v_i the vibrational quantum numbers corresponding to the $3N - 6$ normal vibrations.

Often the vibrational energy (instead of being referred to the minimum of the potential surface as in equation (2.58)), is attributed to the lowest vibrational state ($v_i = 0, i = 1, 2, \dots, (3N - 6)$) with energy of

$$G(v_1 = 0, v_2 = 0, \dots) = \frac{1}{2} \sum_i \omega_i + \frac{1}{4} \sum_{ij} x_{ij} \quad (2.59)$$

above the zero-point energy. One gets

$$\begin{aligned} G_0(v_1, v_2, \dots) &= G(v_1, v_2, \dots) - G(v_1 = 0, v_2 = 0, \dots) \\ &= \sum_i \omega_i^0 v_i + \sum_i \sum_{k \geq i} x_{ik}^0 v_i v_k + \dots, \end{aligned} \quad (2.60)$$

where

$$\omega_i = \omega_i + x_{ii} + \frac{1}{2} \sum_{i \neq k} x_{ik} + \dots, \quad (2.61)$$

with $x_{ik} = x_{ki}$, and if higher powers are neglected, $x_{ik}^0 = x_{ik}$.

Like mentioned before, the fundamentals v_i correspond to the transition from a state with $v_i = 0$ to the $v_i = 1$ state, where all other $v_k = 0$. Therefore from equation (2.60) and (2.61) one derives,

$$\begin{aligned} v_i &= \omega_i^0 + x_{ii} \\ &= \omega_i + 2x_{ii} + \frac{1}{2} \sum_{k \neq i} x_{ik} + \dots \end{aligned} \quad (2.62)$$

Usually most of the x_{ik} are negative and therefore the ω_i are slightly larger than v_i .

2.2.5 Internal Coordinates

The use of force constants k_{ij} associated with mass weighted Cartesian coordinates is mathematically very convenient, but they are difficult to associate with specific internal motions such as bond stretching. It is preferable to

describe the vibrational motion of a molecule in terms of the readily recognizable structural features, i.e. the bond lengths and angles. For example in the HSOH molecule six internal coordinates r_{SH} , r_{OH} , r_{SO} , $\delta(\text{HSO})$, $\delta(\text{SOH})$, and $\tau(\text{HSOH})$ are required to describe the relative positions of the atoms (see Chapter 7). There are also $3N - 6 = 6$ vibrational modes, that must be related in some manner to changes in r_{SH} , r_{OH} , r_{SO} , $\delta(\text{HSO})$, $\delta(\text{SOH})$, and $\tau(\text{HSOH})$. It is convenient to define the internal displacement coordinates Δr_{SH} , Δr_{OH} , Δr_{SO} , $\Delta\delta(\text{HSO})$, $\Delta\delta(\text{SOH})$, and $\Delta\tau(\text{HSOH})$ to correspond to bond-stretching and bond-bending motions.

2.2.6 Vibration-Rotation

In a zero order approximation the energy of a simultaneously vibrating and rotating asymmetric top is simply the sum of its vibrational and rotational energy. In higher approximation one has to take into account that the moments of inertia I_a , I_b , and I_c change periodically during the vibration and thus the formula for a rigid asymmetric top has to be modified in the way that average values A_v , B_v , and C_v during a vibration are used (see Section 2.4). The total energy of vibration and rotation of an asymmetric top molecule (as long as the vibrational state is non-degenerate) is therefore given by

$$T = G(v_1, v_2, \dots) + F_v(J, K_a, K_c), \quad (2.63)$$

where $G(v_1, v_2, \dots)$ is given by the previous equation (2.58), and $F_v(J, K_a, K_c)$ denotes the pure rotational energy of an asymmetric top molecule.

Selection Rules

If, as it is usually the case, the interaction of vibration and rotation is small, the selection rules for the infrared rotational-vibrational spectrum are the same as those given previously for the rotational spectrum (see Section 2.1.2) and vibrational spectrum (see Section 2.2.3). The only difference is that it is the direction of the change of dipole moment during the vibration that matters for the rotational selection rules.

Since the selection rules are different for the different orientations of the transition dipole moment the spectrum of an asymmetric top molecule consists generally of a superposition of sub-bands (hybrid bands), called *a*-type, *b*-type, or *c*-type bands depending on whether the change of the dipole moment is in the direction of the axis of least, intermediate, or largest moment of inertia.

In case of an accidental symmetric prolate top molecule, like HSOH, *a*-type transitions occur only within a K_a -stack. The resulting sub-bands are therefore called *parallel* bands (see Figure 2.2). In case of *b*- and *c*-type transitions ΔK_a equals ± 1 and therefore transitions between the K_a stacks occur. These

sub-bands are called *perpendicular* bands (see Figure 2.2).⁸

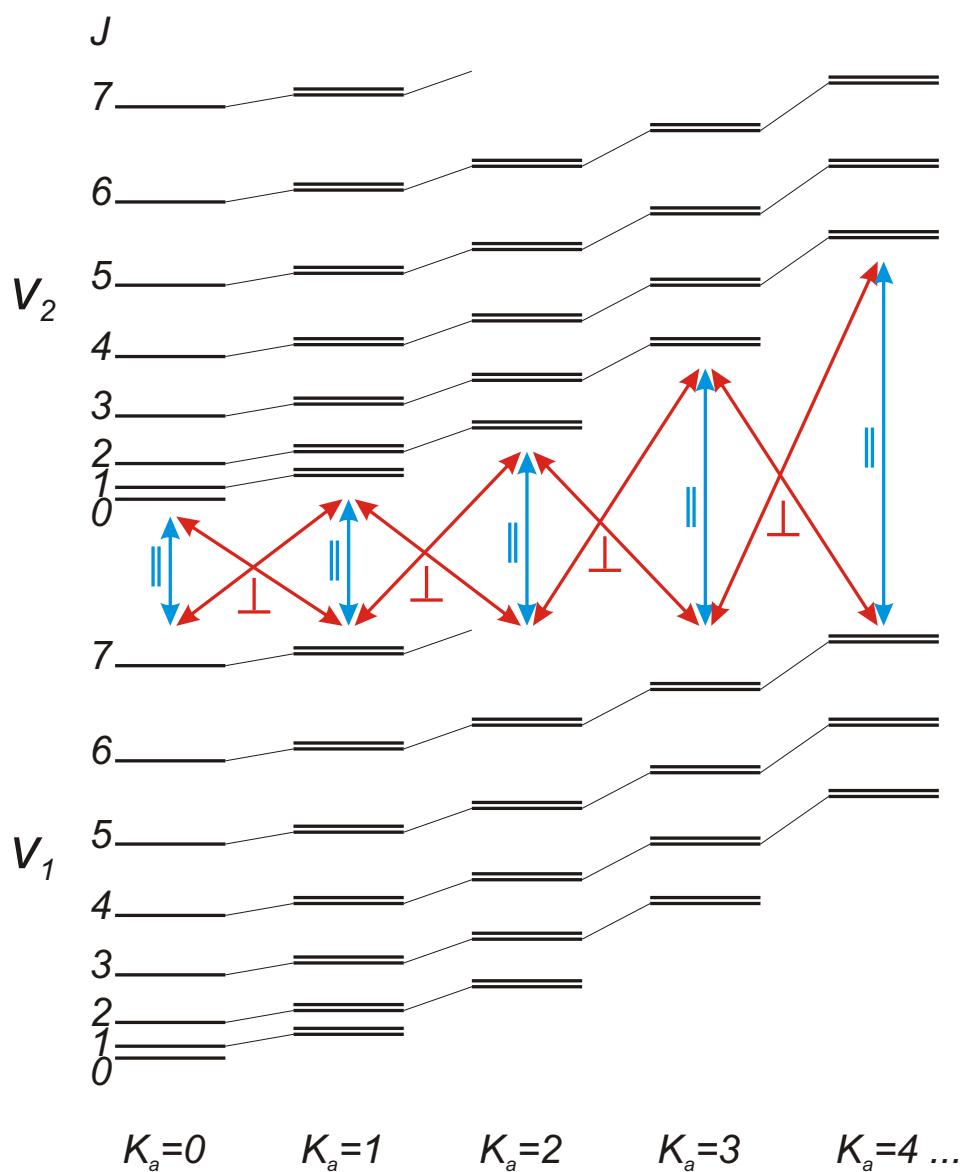


Figure 2.2: Scheme of two vibrational levels of an accidentally symmetric prolate top molecule and possible transitions. Each energy level for $K_a > 0$ occurs as doublet due to the asymmetry splitting. The sub-bands occurring for transitions with $\Delta K_a = 0$ are called *parallel*-type sub-bands, while those with $\Delta K_a = \pm 1$ are *perpendicular*-type sub-bands.

⁸A detailed analysis of a vibrational-rotational spectrum (and the appearance of the different sub-bands) of the accidental symmetric prolate top molecule HSOH is given in the experimental part of this thesis (see Section 8.1).

2.3 Internal motions

For many years the phenomenon of internal motions has been subject of considerable interest to both chemists and physicists. For over 70 years the method of microwave spectroscopy has been employed to study the problem of hindered internal motions. Examples for hindered internal motions are internal rotation, ring puckering, and inversion motion.

The study of internal rotation in microwave spectroscopy is the most active of these areas. For molecules which consist of two groups connected by a single bond, the groups can rotate with respect to one another on the single bond. For a long time, this rotation about a single bond was believed to be completely free because it had been impossible to separate any isomers which could arise from different orientations of one part of the molecule relative to the other. In 1936 Kemp and Pitzer [69, 68] concluded, on the basis of thermodynamic evidence, that the relative rotation of the two methyl groups in ethane is not entirely free but restricted by a potential barrier. Soon after the work of Kemp and Pitzer it became apparent that rotation about single bonds is restricted in many molecules, although the barriers are not large enough to permit chemical isolation.

The effect of internal rotation on the rotational spectrum is that each rotational transition will exhibit a fine structure caused by the interaction of internal and overall rotation. This fine structure depends on the height of the potential barrier hindering internal rotation. Analysis of this fine structure with the high resolution accurate measurements of microwave spectroscopy leads to either the evaluation of the potential barrier or opens the chance to study potential functions, stability of rotational isomers and ring conformations. Studies on this topics will provide basic information for testing and improving predictive methods and for understanding the origin of barriers and the forces responsible for conformational preference.

In course of this thesis the internal rotation tunneling in HSOH has been investigated. With two different rotor bars SH and OH, HSOH represents the most general case of internal rotation in four atomic skew chain molecules. For a general discussion of the field of internal rotation in molecules the textbooks by Mizushima [86] and Orville-Thomas [90] are recommended. In the next Section 2.3.1 the basic ideas and the results of the mathematical treatment by Yamada *et al.* [130] (*Yamada-Winnewisser-Jensen* model) of the internal rotation dynamics in HSOH are given.

2.3.1 *Yamada-Winnewisser-Jensen* model

For the molecules H_2S_2 and H_2O_2 , which are analogous to HSOH but are of higher symmetry (see Chapter 7), and for the structurally similar molecule HNCNH, it has been found [120, 95, 65] that the amount of observed torsional splittings alternate with the parity of the rotational quantum number K_a . This phenomenon can be explained in terms of a relatively simple model proposed by Hougen [63] (see also Hougen and DeKoven [62]). To apply Hougen's theory, one does not need to know the torsional potential energy function $V(\tau)$; Hougen expresses the energy splittings in terms of molecular parameters that can be determined directly from experimental data. The torsional splittings observed experimentally for HSOH vary with K_a in a more complicated manner than found for H_2S_2 , H_2O_2 , and HNCNH. The *Yamada-Winnewisser-Jensen* model [130] extends the Hougen model and intends to give a mathematical treatment of the internal rotation dynamics which points to a more general description of this kind of problem.

The molecule HSOH has two equivalent equilibrium conformations which are enantiomers. The two equivalent equilibrium configurations for HSOH are shown schematically in Figure 2.3. The tunnelling between the two cor-

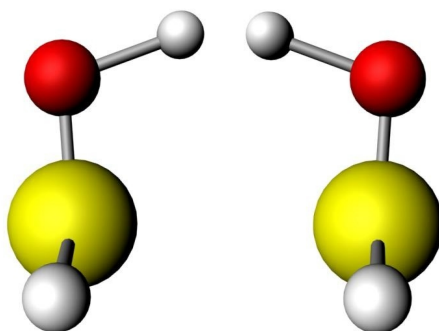


Figure 2.3: The two equivalent equilibrium configurations of HSOH.

responding minima on the potential energy surface is an internal rotation (torsion) about the heavy-atom bond (i.e. the S–O bond in HSOH). Recent *ab initio* calculations [123] at the CCSD(T)/cc-pCVQZ level of theory gives values of 2216 cm^{-1} and 1579 cm^{-1} for the *cis*- and *trans*-barrier heights in HSOH. The *cis*- and *trans*-tunnelling cause the observed transitions of HSOH to split into doublets. To explain the observed alternation of the torsional splittings a 6π period for the torsional potential energy and the torsional wavefunctions is postulated in the *Yamada-Winnewisser-Jensen* (YWJ) model.

Separation of K -rotation and internal rotation

As a first step in the YWJ-model the K -rotation and the internal rotation are separated. Let I_1 and I_2 be the moments of inertia of the SH and OH parts, respectively, with respect to the z -axis⁹. Furthermore an over-all rotation angle χ and an internal rotation angle τ are introduced:

$$\chi = \frac{I_1}{I_1 + I_2} \chi_1 + \frac{I_2}{I_1 + I_2} \chi_2 \quad (2.64)$$

$$\tau = \chi_2 - \chi_1. \quad (2.65)$$

χ_1 and χ_2 are the rotation angles of the SH and OH group (see Figure 2.4), respectively, defined as Euler angles (see Figure 10-1 of reference [20]).

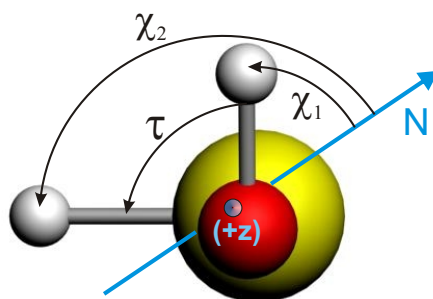


Figure 2.4: Rotation angles χ_1 , χ_2 , and internal rotation angle τ of HSOH.

The kinetic energy operator expressed in terms of χ and τ is

$$T = \frac{1}{2} (I_z \dot{\chi}^2 + I_r \dot{\tau}^2), \quad (2.66)$$

where I_z is the moment of inertia of the molecule about the z -axis, and I_r is the reduced moment of inertia for the internal rotation:

$$I_z = I_1 + I_2 \quad (2.67)$$

$$I_r = \frac{I_1 I_2}{I_1 + I_2}. \quad (2.68)$$

The first term of equation (2.66) represents the kinetic energy of the over-all rotation, and the angle χ represents the direction of the molecule-fixed y -axis in the plane vertical to the z -axis as shown in Figure 10-1 of reference [20].

Introducing the conjugate momenta for χ and τ ,

$$J_z = \frac{\partial T}{\partial \dot{\chi}} = I_z \dot{\chi} \quad (2.69)$$

$$J_\tau = \frac{\partial T}{\partial \dot{\tau}} = I_r \dot{\tau} \quad (2.70)$$

⁹The z -axis in HSOH is almost coincident with the S-O bond (see Chapter 7) and in the I' representation it is identified with the a -axis (see Table 2.1).

the Hamiltonian of the system can be expressed as

$$\mathcal{H} = A\hat{J}_z^2 + F\hat{J}_\tau^2 + V(\tau) \quad (2.71)$$

where $V(\tau)$ is the potential energy for internal rotation.

In general, for an unsymmetrical molecule like HSOH, the moment-of-inertia ratio I_2/I_1 is not a simple rational number. In the case of HSOH, however, this ratio is accidentally close to $1/2$ as suggested by the fact that $B = 284$ GHz for the SH radical [87] and 556 GHz for the OH radical [17] (the ratio is 1.96). Therefore, $I_2 = I_1/2 = I_z/3$ is approximated in the model. The small residual can be treated as a perturbation and thus a torsion-rotation cross term remains in the Hamiltonian¹⁰:

$$\mathcal{H} = A\hat{J}_z^2 + F'\hat{J}_\tau^2 + \xi\hat{J}_z\hat{J}_\tau + V(\tau). \quad (2.72)$$

Extending the Hamiltonian in equation (2.72) with zero-order terms describing end-over-end rotation (i.e. the rotation about the x and y molecule fixed axes) gives:

$$\mathcal{H}_{rt} = A\hat{J}_z^2 + F'\hat{J}_\tau^2 + B_x(\tau)\hat{J}_x^2 + B_y(\tau)\hat{J}_y^2 + \xi\hat{J}_z\hat{J}_\tau + V(\tau) \quad (2.73)$$

where $B_x(\tau)$ and $B_y(\tau)$ are functions of τ .

Torsional splittings of HSOH

In the period of $-\pi < \tau \leq \pi$, the torsional potential energy function has one minimum at $\tau \approx -\pi/2$ and another equivalent one at $\tau \approx +\pi/2$. The molecular geometry at $\tau \approx -\pi/2$ is denoted as L_0 and that at $\tau \approx +\pi/2$ as R_0 , where L stands for 'Left' and R for 'Right'. The two forms are enantiomers, i.e. they are energetically equivalent¹¹ but chirally different.

With the approximation $I_2 = I_1/2 = I_z/3$ the above given equations (2.64) & (2.65) are simplified:

$$\chi = \frac{2}{3}\chi_1 + \frac{1}{3}\chi_2 \quad (2.74)$$

$$\tau = \chi_2 - \chi_1. \quad (2.75)$$

Rotation of the OH moiety by 360° relative to the SH moiety gives

$$\chi \rightarrow \chi + 2\pi/3. \quad (2.76)$$

¹⁰For more details see Section 3.3. in reference [130]

¹¹At least if the extremely small effects of the weak interaction force are neglected.

This means, that the molecule-fixed y -axis is rotated by $2\pi/3$ about the z -axis. However, this rotation changes neither the molecular geometry nor the orientation of the molecule in space. It follows, that the χ -values χ_0 , $\chi_0 + 2\pi/3$, and $\chi_0 + 4\pi/3$ describe the same molecular geometry -meaning χ is *triple valued* for HSOH. Thus, in the YWJ-model a 6π periodicity for τ is postulated and the range of distinct τ values is extended to $-3\pi < \tau \leq 3\pi$. In consequence four additional energetically equivalent localized states have to be considered as illustrated in Figure 2.5: L_{-1} at $\tau \approx -5\pi/2$, R_{-1} at $\tau \approx -3\pi/2$, L_1 at $\tau \approx 3\pi/2$, and R_1 at $\tau \approx 5\pi/2$.

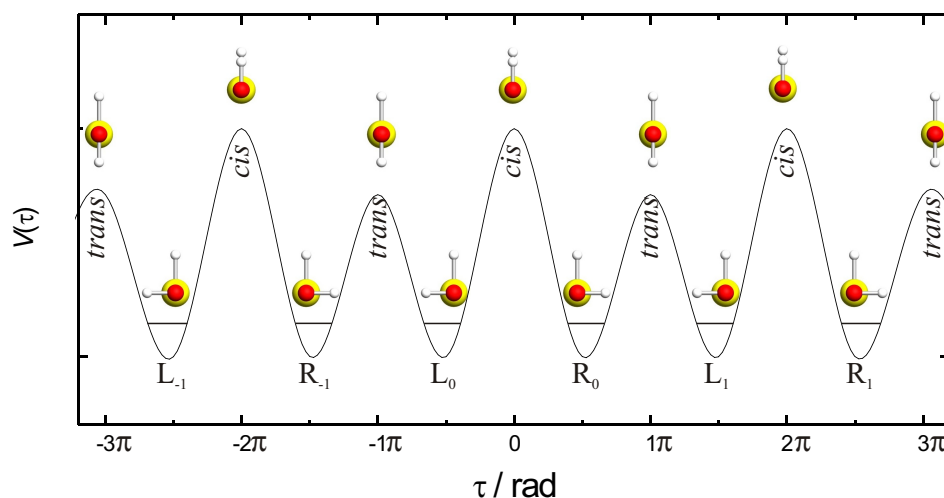


Figure 2.5: The 6π -periodic potential $V(\tau)$ ($-3\pi < \tau \leq 3\pi$; see text) for HSOH is shown in the situation where the *cis*-barrier is higher than the *trans*-barrier. The ratio between the two barrier heights is taken to be 0.71 as obtained from *ab initio* results in [123]. The six equivalent minima are indicated by the labels L_i and R_i , $i = -1, 0, \text{ and } 1$.

For each of the six minima L_{-1} , R_{-1} , L_0 , R_0 , L_1 , and R_1 , a localized torsional wavefunction is introduced and so the six torsional wavefunctions are

$$(\phi_{L_{-1}}(\tau), \phi_{R_{-1}}(\tau), \phi_{L_0}(\tau), \phi_{R_0}(\tau), \phi_{L_1}(\tau), \phi_{R_1}(\tau)). \quad (2.77)$$

These wavefunctions are equivalent in that they can be transformed into each other by inversion and/or displacement along the τ axis. The phases of the functions are chosen in the following way (see Figure 2.5 for the locations of the minima)

$$\phi_{L_0}(\tau) = \phi_{R_0}(-\tau) = \phi_{L_{-1}}(\tau - 2\pi) = \phi_{R_1}(-\tau + 2\pi) = \phi_{L_1}(\tau + 2\pi) = \phi_{R_{-1}}(-\tau - 2\pi). \quad (2.78)$$

In the *Yamada – Winnewisser – Jensen* model a matrix representation of the torsional Hamiltonian

$$\mathcal{H}_{tors} = F' \hat{J}_\tau^2 + V(\tau) \quad (2.79)$$

is introduced. Since the six basis functions are equivalent, the six diagonal elements are equal and given by the value Q . 'Neighboring' basis functions

interacting through the *trans*-barrier are taken to be connected by an off-diagonal matrix element W_t and basis functions interacting through the *cis*-barrier are taken to be connected by an off-diagonal matrix element W_c . The following matrix is obtained

$$\begin{pmatrix} Q & W_c & 0 & 0 & 0 & W_t \\ W_c & Q & W_t & 0 & 0 & 0 \\ 0 & W_t & Q & W_c & 0 & 0 \\ 0 & 0 & W_c & Q & W_t & 0 \\ 0 & 0 & 0 & W_t & Q & W_c \\ W_t & 0 & 0 & 0 & W_c & Q \end{pmatrix} \quad (2.80)$$

where for simplicity, W_t and W_c are assumed to be real.

The crux of the matter in equation (2.73) is that, due to the perturbation term $\xi \hat{J}_z \hat{J}_\tau$ -unlike in the case of HSSH and HOOH- the torsion and rotation cannot really be separated in HSOH. The interaction creeps in again for the case of $K = 3t \pm 1 = 1, 2, 4, 5, \dots$ showing that for these K -levels the allowed rotation torsion functions cannot be written as simple products of rotational and torsional functions. This spoils the separation of these two types of motion. Hence, the two cases of $K_a = 3t = 0, 3, 6, \dots$ and $K_a = 3 \pm 1 = 1, 2, 4, 5, \dots$ are considered separately.

First Case: $K = 3t = 0, 3, 6, 9, \dots$

A sketch of the pattern of torsional energy-level splittings for states with $K = 3t > 0$ (where t is an integer) for HSOH are depicted in Figure 2.6. When

Figure 2.6: The pattern of torsional energy-level splittings for states with $K = 3t > 0$ (where t is an integer) for HSOH.

there is no torsional tunneling, the molecule has the energies states $E_{rot}^{(0)} + Q$ and $E_{rot}^{(1)} + Q$ as shown on the left hand side of Figure 2.6. These two states correspond to the rotational states $J_{K_a, K_c} = J_{K, J-K+1}$ and $J_{K_a, K_c} = J_{K, J-K}$. Torsional tunneling causes each of the two rotational states to combine with the two torsional wavefunctions. These two torsional states have opposite parities and the energies split by the amount

$$\Delta_{3t} = 2 |W_c + W_t|. \quad (2.81)$$

The two rotational wavefunctions corresponding to the energies $E_{rot}^{(0)}$ and $E_{rot}^{(1)}$ also have opposite parities, and so the parities of the rotation-torsion states will be as indicated by the + and – signs to the right of the torsion-split energy levels. The ‘outer’ rotation-torsion states (i.e. the states with the highest and lowest energies, respectively) always have the same parity (here +), and the common parity of the two ‘inner’ states (here –) is opposite to that of the outer states.

The splitting given in equation (2.81) is independent of J .

Second Case: $K = 3t \pm 1 = 1, 2, 4, 5, 6, 7, \dots$

In Figure 2.7 the pattern of torsional energy-level splittings for states with $K = 3t \pm 1$ (where t is an integer) is shown for HSOH. When there is no torsional tunnelling, the molecule has the energies $E_{rot}^{(0)} + Q$ and $E_{rot}^{(1)} + Q$ as shown on the left hand side of Figure 2.7. These two states correspond to the rotational states $J_{K_a, K_c} = J_{K, J-K+1}$ and $J_{K, J-K}$. The effect of torsional tunneling is mathematically described as the splitting of a hypothetical, 4-fold degenerate, ‘average’ state with energy $(E_{rot}^{(0)} + E_{rot}^{(1)})/2 + Q$ into the four sub-levels on the right hand side of the figure. The absolute value of the torsional splittings is

$$\Delta_{3t\pm 1} = \left| |H_{ab}^{(0)}| - |H_{ab}^{(1)}| \right|. \quad (2.82)$$

In equation (2.82) $|H_{ab}^{(P)}|$ is given by

$$\left| H_{ab}^{(P)} \right| = \sqrt{\left((-1)^P \Delta_{rot}^{(JK)} + W_c - W_t/2 + W_{JK}^{(P)} \right)^2 + 3W_t^2/4} \quad (2.83)$$

with

$$\Delta_{rot}^{(JK)} = \frac{1}{2} \left(E_{rot}^{(0)} - E_{rot}^{(1)} \right), \quad (2.84)$$

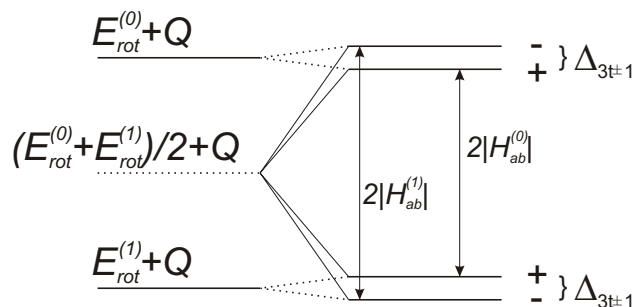


Figure 2.7: The pattern of torsional energy-level splittings for states with $K = 3t \pm 1$ (where t is an integer) for HSOH.

which is the amplitude of the splitting due to the asymmetry splitting, and

$$W_{JK}^{(P)} = 2B_{ab}(J(J+1) - K^2) + D_{ab}qK - \delta_{P1}(-1)^{J+P}C_{ab}J(J+1).^{12} \quad (2.85)$$

When the amplitude

$$|\Delta_{rot}^{(JK)}| = \left| \frac{1}{2} (E_{rot}^{(0)} - E_{rot}^{(1)}) \right| \quad (2.86)$$

of the splitting due to the asymmetry of the molecule is much larger than $|W_c - W_t/2 + W_{JK}^{(P)}|$, the sizes of the splittings are such that the net effect can be understood as a splitting of each of the rotational levels $E_{rot}^{(0)} + Q$ and $E_{rot}^{(1)} + Q$ into two sub-levels with wavefunctions of opposite parity. The + and - signs to the right of the torsion-split energy levels define the parities of the states. The torsional splittings $\Delta_{3t\pm 1}$ (equation (2.82)) are indicated in Figure 2.7.

In the limit of $J = 0$ one gets

$$\lim_{J \rightarrow 0} W_{JK}^{(P)} = -2B_{ab}K^2 + D_{ab}qK \quad (2.87)$$

$$\lim_{J \rightarrow 0} \Delta_{rot}^{(JK)} = \Delta_K^{(0)} \quad (2.88)$$

and with these results

$$\begin{aligned} \Delta_{3t\pm 1}^{(0)} = & \left| \sqrt{\left(+\Delta_K^{(0)} + W_c - W_t/2 - 2B_{ab}K^2 + D_{ab}qK\right)^2 + 3W_t^2/4} \right. \\ & \left. - \sqrt{\left(-\Delta_K^{(0)} + W_c - W_t/2 - 2B_{ab}K^2 + D_{ab}qK\right)^2 + 3W_t^2/4} \right|. \end{aligned} \quad (2.89)$$

The other limiting case, the 'symmetric top limit' is attained when $|\Delta^{(JK)}| \rightarrow 0$ so that $|\Delta_K^{(0)}| \rightarrow 0$. According to rigid-rotor theory, this limit is reached for high K , which means $K > 3$ in case of HSOH. In the symmetric top limit, $E_{rot}^{(0)} = E_{rot}^{(1)}$, the situation is as depicted in Figure 2.8. In the absence of torsional tunneling, the molecule has one 4-fold degenerate state with energy $E_{rot}^{(0)} + Q = E_{rot}^{(1)} + Q$ as shown on the left hand side of Figure 2.8. Torsional tunneling causes this state to split into two doubly degenerate states; each of these states has a wavefunction component with + parity and one with - parity as indicated by the + and - signs to the right of the torsional-split energy levels. In this case, the torsional splitting for $J \rightarrow 0$ is defined as

$$\Delta_{3t\pm 1}^{(sym-top)} = 2\sqrt{(W_c - W_t/2 - 2B_{ab}K^2 + D_{ab}qK)^2 + 3W_t^2/4} \quad (2.90)$$

where the limiting value of $2|H_{ab}^{(0)}| = 2|H_{ab}^{(0)}|$ is obtained from equations (2.83) and (2.87) and from the fact that $|\Delta_{rot}^{(JK)}| \rightarrow 0$ in the symmetric top limit.

¹² B_{ab} , C_{ab} , and D_{ab} are coefficients of higher order, $q = +1$ or -1 depending on whether $K_a = 3t + 1$ or $K_a = 3t - 1$, and the Kronecker $\delta_{P1} = 1(0)$ for $P = 1(0)$. For more details see reference [130].

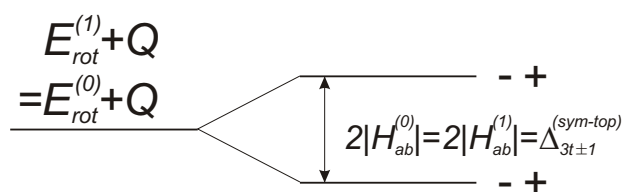


Figure 2.8: The pattern of torsional energy-level splittings for states with $K = 3t \pm 1$ in the symmetric top limit (where t is an integer) for HSOH.

States with $K = 3t > 0$ show the same splitting pattern as shown here in the symmetric top limit, but in this case the tunneling splitting is

$$\Delta_{3t}^{(sym-top)} = 2|W_c + W_t|. \quad (2.91)$$

2.4 Derivation of Molecular Structures

One of the most important aims of spectroscopy is the accurate determination of the geometric structure of molecules. The Hamiltonian used to analyze the rotational spectra of most molecules consists of some collection of the following terms:

$$\mathcal{H} = \mathcal{H}_r + \mathcal{H}_d + \mathcal{H}_Q + \mathcal{H}_I + \mathcal{H}_{IR} + \dots \quad (2.92)$$

in which \mathcal{H}_r is the rigid rotor Hamiltonian, \mathcal{H}_d is the contribution from centrifugal distortion, \mathcal{H}_Q describes the nuclear quadrupole interaction, \mathcal{H}_I contains the internal rotation energy, and \mathcal{H}_{IR} describes the interaction of internal and overall rotation. Once the major work of identifying the spectrum of a molecule is performed, it is possible to calculate the rotational constants of the molecule, and from these the molecular moments of inertia. Thus, for the purpose of distance and angle determination the most important part in equation (2.92) is

$$\hbar^2 \mathcal{H}_r = A\hat{J}_a^2 + B\hat{J}_b^2 + C\hat{J}_c^2 \quad (2.93)$$

in which \hat{J}_a , \hat{J}_b , and \hat{J}_c are the components of the rotational angular momentum in the description of the molecule fixed a , b , and c principal axes, and A , B , and C are the rotational constants.

However, all spectroscopic measurements have to be performed on vibrating molecules; even in the ground state the molecules have a certain amount of vibrational energy, the zero-point energy (see e.g. Section 2.2.4). Anharmonicities of the molecular potential cause the rotational constants to change with vibrational excitation (see Figure 2.9). For this reason, the primary source of problems appearing when evaluating structural parameters from the rotational constants is the fact that the dimensions of a molecule

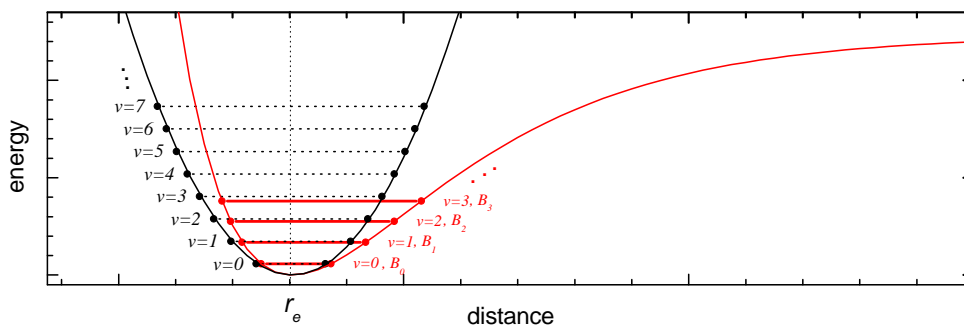


Figure 2.9: Sketch of a harmonic and an anharmonic potential of a diatomic molecule. Each vibrational level has its own rotational constant B_v .

are affected by its vibrational energy state¹³.

Different procedures have been introduced that correct vibrational effects to various degrees and lead to different conceptions of interatomic distance. In particular, five types of bond lengths have been defined:

r_e , the equilibrium bond lengths for the hypothetical vibrationless state, evaluated by correcting the effects of vibration including zero-point vibration.

r_0 , the effective bond lengths for the vibrational ground state, calculated from rotational constants $B_{v=0}$ or moments of inertia $I^{v=0}$.

r_s , the substitution bond lengths, derived from the isotopic substitution method.

$\langle r \rangle$ (or r_z), the average bond lengths associated to the average configuration of the atoms, evaluated by a partial correction for the effects of vibration.

r_m , the mass-dependence bond lengths, derived from a large number of isotopic species by a first-order treatment of isotopic effects.

In the course of this work an empirical equilibrium structure of HSOH was determined. Therefore a brief discussion of the r_e structure is given in the following¹⁴.

2.4.1 Evaluation of Equilibrium Structures

A general and very convenient method for the determination of molecular structure from equilibrium constants has been given by Kraitchman [76]. Provided that the Born-Oppenheimer approximation holds true, the r_e equilibrium geometry is the same for all isotopologues. Hence, after an isotopic substitution has been made on an atom in the molecule, the coordinates of that atom can be determined directly with respect to the principal axes of the original molecule. When coordinates of a sufficient number of atoms have been determined via isotopic substitution, they are substituted into the equations for the moments of inertia to solve for the remaining coordinates. In the case of a nonplanar asymmetric top molecule, having N atoms, all nine moment equations are available, i.e. those from (2.3) and the three center-of-mass equations. Therefore, if $N - 3$ substitutions are made, the three Cartesian coordinates of each of the substituted atoms can be determined.

¹³Note that the uncertainties are not arising from the uncertainties in Planck's constant or the atomic mass.

¹⁴For further information on the determination of molecular structure the textbook of Gordy and Cook [48] is recommended. A comparison of the different types of parameters for representative molecules has been given e.g. in [27, 58, 77].

The signs of the coordinates have to be determined from other sources (e.g. electron diffraction measurements, or theoretical chemistry). Substitution of these data into the nine moment equations yields nine equations in nine unknowns -the unknowns being the coordinates of the remaining three unsubstituted atoms. Since six of these equations are of the second degree and three of the first degree, an exact solution of these equations would be quite difficult. It is expedient to use a numerical technique to solve these equations and hence to determine a completely structural configuration from only $N - 3$ substitutions. Obviously if measurements of $N - 2$ substitutions were available, the determination becomes fairly simpler and the need for accurate data from other sources is immensely reduced. When information of $N - 1$ substitutions is available, the determination becomes even simpler; in this case data from other sources may be helpful aids but are not strictly necessary.

If effective moments of inertia are used an exact agreement should not be expected unless the effects of zero-point vibrations are taken into account, because anharmonicities of the molecular potential cause the rotational constants to change with vibrational excitation. Applying perturbation theory to the vibration-rotation Hamiltonian expressed in normal coordinates leads to an expansion of the rotational constants A_v , B_v , and C_v of the v^{th} vibrational state r in powers of $(v + 1/2)$ which are linear to second order perturbation.

$$A_v = A_{(v_1, v_2, \dots, v_{3N-6})} = A_e - \sum_r \alpha_r^A \left(v_r + \frac{1}{2} \right) \quad (2.94)$$

$$B_v = B_{(v_1, v_2, \dots, v_{3N-6})} = B_e - \sum_r \alpha_r^B \left(v_r + \frac{1}{2} \right) \quad (2.95)$$

$$C_v = C_{(v_1, v_2, \dots, v_{3N-6})} = C_e - \sum_r \alpha_r^C \left(v_r + \frac{1}{2} \right) \quad (2.96)$$

Dependencies of the rotational constants on the vibrational quantum numbers v are conventionally denoted by α_r^A , α_r^B , and α_r^C where the subscript refers to the r normal coordinate. In this approximation the molecular rotational constants for the vibrational ground state A_0 , B_0 , and C_0 are related to their equilibrium rotational constants A_e , B_e , and C_e via

$$A_e = A_0 + \frac{1}{2} \sum_r \alpha_r^A. \quad (2.97)$$

$$B_e = B_0 + \frac{1}{2} \sum_r \alpha_r^B. \quad (2.98)$$

$$C_e = C_0 + \frac{1}{2} \sum_r \alpha_r^C. \quad (2.99)$$

For a nonlinear molecule counting N atoms one has to sum up over the $r = 3N - 6$ vibrational modes.

The rotational constants A_e , B_e , and C_e are related to the principal moments of inertia I_a , I_b , and I_c ¹⁵ by

$$A_e = h/(8\pi^2 c I_a) \quad (2.100)$$

$$B_e = h/(8\pi^2 c I_b) \quad (2.101)$$

$$C_e = h/(8\pi^2 c I_c) \quad (2.102)$$

and thus can be used to determine the molecular structure. As mentioned above the r_e equilibrium geometry is the same for all isotopologues¹⁶ and can therefore be derived from a least-squares fit of molecular bond distances and angles to a set of rotational constants or moments of inertia. The vibration-rotation correction terms α_r^A , α_r^B , and α_r^C can be derived experimentally from the rotation constants A_{v_r} , B_{v_r} , and C_{v_r} ¹⁷ of vibrational level v_r by

$$\alpha_r^A = (A_0 - A_{v_r})/v_r \quad (2.103)$$

$$\alpha_r^B = (B_0 - B_{v_r})/v_r \quad (2.104)$$

$$\alpha_r^C = (C_0 - C_{v_r})/v_r. \quad (2.105)$$

When rotational constants of certain vibrational states are not available from experiments, calculated α_r values can be used instead to derive an *empirical* equilibrium structure r_e^{emp} . A detailed study of the accuracy of molecular equilibrium geometries obtained from least squares fits involving experimental rotational constants A_0 , B_0 , and C_0 and sums of *ab initio* vibration-rotation interaction constants α_r^A , α_r^B , and α_r^C is given by Pawłowski *et al.* [94]. As a result they obtained relative errors from 0.02% – 0.06% of the *empirical* bond distances determined from interaction constants at the CCSD(T)/cc-PVQZ level, surpassing the accuracy obtained either by purely experimental techniques (except for the smallest systems such as diatomics) or by pure *ab initio* methods.

¹⁵Note, the principal moments of inertia are related to the equilibrium structure of the molecule.

¹⁶Under the assumption that the Born-Oppenheimer approximation applies.

¹⁷ $A_{v_r} = A_{(0,\dots,0,v_r,0,\dots,0)}$, similar for B_{v_r} and C_{v_r}

3

Basics on Quantum Chemical Calculations

The detection of new molecular species by rotational spectroscopy critically depends on the availability of accurate predictions of the corresponding spectroscopic parameters. HSOH for example is obtained in reaction mixtures (i.e. via pyrolytic reactions or gas discharges (see Chapter 5)) and thus the observed spectra are very dense and contain transitions of all species present. The key to the successful identification of HSOH among the pyrolysis products of $(t\text{-Bu})_2\text{SO}$ ¹ has been the availability of accurate predictions of the structure and rotational constants of HSOH based on high-level quantum-chemical calculations using state-of-the art coupled-cluster techniques (see reference [123]). In the same way, calculations were essential to guide the first detection of the corresponding isotopologues HSOD via its rotational spectrum (see Chapter 6), presented in this thesis. The spectroscopic investigations on HSOH in the IR-region were assisted by high level *ab initio* calculations, too (see Chapter 8).

Because rotational constants of all vibrational states of HSOH are not available from experiments, calculated rotational vibrational interaction constants α_r^B have been used instead to derive an empirical equilibrium structure r_e^{emp} (see Chapter 7).

Furthermore, the interpretation of the torsional splittings observed in the HSOH spectra is considerably simplified by high quality quantum chemistry calculations presented in this thesis (see Section 8.2 and Chapter 9).

Due to the close combination of quantum chemistry and spectroscopy in this thesis, the basic ideas on *ab initio* molecular orbital theory and the numerical approach 'TROVE'² -to calculate rovibrational energies for polyatomic molecules- are introduced below.

¹For details on the chemistry see Chapter 5

²Theoretical ROVibrational Energies (TROVE) see reference [132]

3.1 *Ab initio* Molecular Orbital Theory

In this section a brief description of the fundamental concepts that underlie the algorithms of typical off-the-shelf *ab initio* molecular orbital software is given. The summary presented here is mainly based on an article by Dorsett and White [35]; more comprehensive discussion of molecular orbital theory may be found in references [5, 4, 26, 54, 80, 104].

3.1.1 The physicochemical model

The basis of electronic structure methods is the assumption that all chemistry can be described in terms of the interactions between electronic charges within molecules. Hence, chemical bonds can be loosely defined as a redistribution of electronic charge that stabilizes the molecule with respect to a collection of its (isolated) constituent atoms. Relative stabilities are expressed in terms of the total energy of the system, which is defined by a differential equation,

$$\mathcal{H} = \hat{T} + \hat{V}. \quad (3.1)$$

\mathcal{H} is the Hamiltonian operator representing the sum of kinetic (\hat{T}) and potential (\hat{V}) energies. In quantum mechanical systems, the kinetic energy of a particle is

$$\hat{T} = \frac{-\hbar^2}{2m} \nabla^2, \quad (3.2)$$

where m is the mass of the particle, h is Planck's constant, and

$$\nabla^2 = \frac{\partial^2}{\partial x^2} + \frac{\partial^2}{\partial y^2} + \frac{\partial^2}{\partial z^2}. \quad (3.3)$$

For electrostatic systems, the potential energy is generally expressed in terms of pairwise interactions between charged particles:

$$\hat{V} = \frac{q_1 q_2}{4\pi\epsilon_0} \frac{1}{|\vec{r}_2 - \vec{r}_1|}, \quad (3.4)$$

where ϵ_0 is the permittivity of free space, and $|\vec{r}_2 - \vec{r}_1|$ is the distance between charges q_1 and q_2 .

The molecular Hamiltonian

Under the basic assumption of electronic structure methods, a molecule is a collection of charged quantum particles. The molecular Hamiltonian has the form of equation (3.1) above, however the kinetic energy is now a summation over all the particles i in the molecule,

$$\hat{T} = \frac{-\hbar^2}{2m} \sum_i \frac{1}{m_i} \left(\frac{\partial^2}{\partial x_i^2} + \frac{\partial^2}{\partial y_i^2} + \frac{\partial^2}{\partial z_i^2} \right), \quad (3.5)$$

and the potential energy is the Coulomb interaction between each pair of charged particles (electron-nucleus attraction, nucleus-nucleus repulsion, and electron-electron repulsion):

$$\hat{V} = \frac{1}{4\pi\epsilon_0} \sum_j \sum_{k < j} \frac{q_j q_k}{|\vec{r}_k - \vec{r}_j|}. \quad (3.6)$$

For electrons, q equals $-e$, and for nuclei of atomic number Z , $q = +Ze$.

3.1.2 Hartree-Fock theory

The Schrödinger equation

The quantum mechanical description of chemical bonds is given by a space- and time-dependent probability distribution: the molecular wavefunction, $\psi(t)$. The molecular wavefunction is defined by the Schrodinger equation

$$\mathcal{H}\psi(t) = i\hbar \frac{\partial \psi(t)}{\partial t}. \quad (3.7)$$

If the potential energy operator is time-independent the solution obtained by separation of variables leads to the molecular wavefunction

$$\psi(t) = \psi e^{-iEt/\hbar}, \quad (3.8)$$

where ψ satisfies the time-independent Schrödinger equation

$$\mathcal{H}\psi = E\psi, \quad (3.9)$$

and E is the total energy of the molecule. Solutions of the time-independent Schrodinger equation represent various stationary states of the molecule (corresponding to stable or meta-stable electronic configurations). The set of wavefunctions ψ which satisfy equation (3.9) are its eigenfunctions, and the energies of the molecule E in each stationary state are its eigenvalues. The stationary state with the lowest energy is called the *ground state*.

Antisymmetry and electron spin

Standard electronic structure methods assume that the molecular wavefunction describing several electrons can be written as a product of single-electron wavefunctions called *orbitals*; that is, for a molecule containing n electrons,

$$\psi(1, 2, \dots, n) = \psi(1)\psi(2)\dots\psi(n). \quad (3.10)$$

Electrons possess an intrinsic angular momentum or *spin* with a value of $\pm\frac{1}{2}$. A halfinteger spin quantum number implies that electrons i and j are antisymmetric with respect to exchange:

$$\psi(i, j) = -\psi(j, i). \quad (3.11)$$

The simplest antisymmetric combination of molecular orbitals (MOs) is a matrix determinant. A Hartree-Fock (HF) wavefunction is constructed by assigning electrons to molecular orbitals $\phi(\vec{r})$ in pairs of opposite spin, and then forming a determinant using two spin functions α and β , where

$$\alpha(\uparrow) = 1 \quad \alpha(\downarrow) = 0 \quad (3.12)$$

$$\beta(\uparrow) = 0 \quad \beta(\downarrow) = 1. \quad (3.13)$$

For two electrons i and j , the total wavefunction takes the form:

$$\psi(i, j) = \phi(\vec{r}) \begin{vmatrix} \alpha(i) & \beta(i) \\ \alpha(j) & \beta(j) \end{vmatrix} \quad (3.14)$$

with a determinant

$$\psi(i, j) = \frac{\phi(\vec{r})}{\sqrt{2}} (\alpha(i)\beta(j) - \beta(i)\alpha(j)) \quad (3.15)$$

which satisfies the antisymmetrisation condition of equation (3.11). For a molecule containing n electrons, the wavefunction is referred to as a *Slater determinant*, and takes the form:

$$\psi = \frac{1}{\sqrt{n!}} \begin{vmatrix} \phi_1(1)\alpha(1) & \phi_1(1)\beta(1) & \phi_2(1)\alpha(1) & \phi_2(1)\beta(1) & \dots & \phi_{n/2}(1)\alpha(1) & \phi_{n/2}(1)\beta(1) \\ \phi_1(2)\alpha(2) & \phi_1(2)\beta(2) & \phi_2(2)\alpha(2) & \phi_2(2)\beta(2) & \dots & \phi_{n/2}(2)\alpha(2) & \phi_{n/2}(2)\beta(2) \\ \vdots & \vdots & \vdots & \vdots & \dots & \vdots & \vdots \\ \vdots & \vdots & \vdots & \vdots & \dots & \vdots & \vdots \\ \phi_1(n)\alpha(n) & \phi_1(n)\beta(n) & \phi_2(n)\alpha(n) & \phi_2(n)\beta(n) & \dots & \phi_{n/2}(n)\alpha(n) & \phi_{n/2}(n)\beta(n) \end{vmatrix}. \quad (3.16)$$

Ab initio essentials

For systems of more than two interacting particles, the Schrödinger equation cannot be solved exactly³. Therefore, all *ab initio* calculations for many-body systems (e.g. molecules) involve some level of approximation. Nevertheless, *ab initio* methods for molecular calculations must satisfy a set of stringent criteria:

- Solutions must be well defined and specified by both the structure and the electronic states of the molecule.
- The potential energy of the molecule must vary smoothly and continuously with respect to displacements of the atomic nuclei.
- The model must contain no bias (e.g., assuming a chemical bond exists between two atoms.)

³This holds true for any system, quantum mechanical or classical.

- The model must be *size-consistent* -that is, solutions and their associated errors must scale in proportion to the size of the molecule⁴.
- The model must be *variational* -that is, approximate solutions must provide an upper bound to the *true* energy of the system. Consequently, the approximate solution having the lowest energy represents the closest fit to the true wavefunction, within the constraints of the method.

Approximations

Non-relativistic solutions

Typical *ab initio* electronic structure methods are time-independent, solving only the spatial wavefunction, $\Psi(\vec{r})$. This approximation is reasonable for most chemical systems, but breaks down in calculations involving large atoms (late transition metals, lanthanides, etc.), whose inner-shell electrons have velocities approaching the speed of light.

Born-Oppenheimer approximation

Electrons in molecules are much lighter than nuclei, and therefore generally have much higher velocities. Hence, under most circumstances, one can assume that electrons respond instantaneously to nuclear displacements. In practice, this means that the molecular Hamiltonian \mathcal{H} can be written assuming the nuclear positions are fixed (i.e., neglecting nuclear kinetic energy terms):

$$\mathcal{H} = \hat{T}_{\text{electrons}} + V = \frac{-\hbar^2}{2m_e} \sum_i^{\text{electrons}} \nabla_i^2 + \frac{1}{4\pi\epsilon_0} \sum_j \sum_{j < k} \frac{q_j q_k}{|\vec{r}_k - \vec{r}_j|}. \quad (3.17)$$

Most *ab initio* calculations solve only the electronic part of the molecular wavefunction, and therefore cannot account for systems where the electronic states are strongly coupled to nuclear vibrations.

Single particle approximation

As mentioned before, standard electronic structure methods approximate the total wavefunction of a many-electron system as the product of single-electron wavefunctions (equation (3.11)). This is the essence of Hartree-Fock (HF) theory, which describes each electron in a molecule as moving in the average electric field generated by the other electrons and nuclei. As a single-particle theory, HF theory systematically overestimates molecular energies because it neglects the correlated motion of electrons resulting from Coulomb interactions.

⁴Size-consistency allows direct comparison between molecules of different sizes, and is therefore an important consideration for studies of chemical reactions.

Linear combinations of atomic orbitals (LCAO)

Although there is no exact analytical solution to the time-independent molecular Schrödinger equation (equation (3.9)) for systems containing more than one electron, approximate solutions can be obtained using standard numerical techniques. The approach of all *ab initio* techniques is to build the total wavefunction from a *basis* set of mathematical functions capable of reproducing critical properties of the system. An individual molecular orbital may then be expressed as

$$\phi_i(\vec{r}) = \sum_{\mu=1}^N c_{\mu i} \chi_{\mu}(\vec{r}), \quad (3.18)$$

where $\chi_{\mu}(\vec{r})$ are the basis functions, and the coefficients $c_{\mu i}$ are adjustable parameters. For a molecular wavefunction, the electronic orbitals of the constituent atoms form a natural set of basis functions. These atomic orbitals can in turn be represented by different types of mathematical functions. A highly accurate set of atomic orbitals (Slater-type orbitals or STOs) are based on hydrogenic wavefunctions having the form

$$\chi_{\text{STO}}(\vec{r}) \sim C e^{-\alpha r}. \quad (3.19)$$

Exponential functions are not well suited to numerical manipulation, so most electronic structure calculations approximate STOs with a linear combination of gaussian-type functions,

$$\chi_{\text{STO}}(\vec{r}) \sim \chi_{\mu} = \sum_{\nu} d_{\mu\nu} e^{-\alpha_{\nu} r^2}, \quad (3.20)$$

where $d_{\mu\nu}$ and α_{ν} are adjustable parameters. As can be seen from Figure 3.1, gaussian-type functions provide reasonable approximations of STOs, except at very small or very large electron-nucleus separations. Linear combinations of *primitive* gaussian functions are referred to as *contracted* gaussians. Standard *ab initio* software packages offer a choice of basis sets containing contracted gaussians optimised to reproduce the chemistry of a large range of molecular systems. A more detailed discussion of molecular basis sets is provided in Section 3.1.3.

The variational principle and Roothan-Hall equations.

The sections above describe a method for constructing a determinantal wavefunction from a set of LCAO-MOs. It remains now to define a method to determine the MO expansion coefficients $c_{\mu i}$ (equation (3.18)) which optimize the molecular wavefunction for a particular system. The variational nature of the model guarantees that the energy eigenvalue solution for any approximate wavefunction is always larger than the energy obtained using the exact wavefunction. It follows that the set of coefficients minimizing the energy of the resultant wavefunction will give the best approximation to the exact wavefunction from a chosen basis set. The variational constraint leads

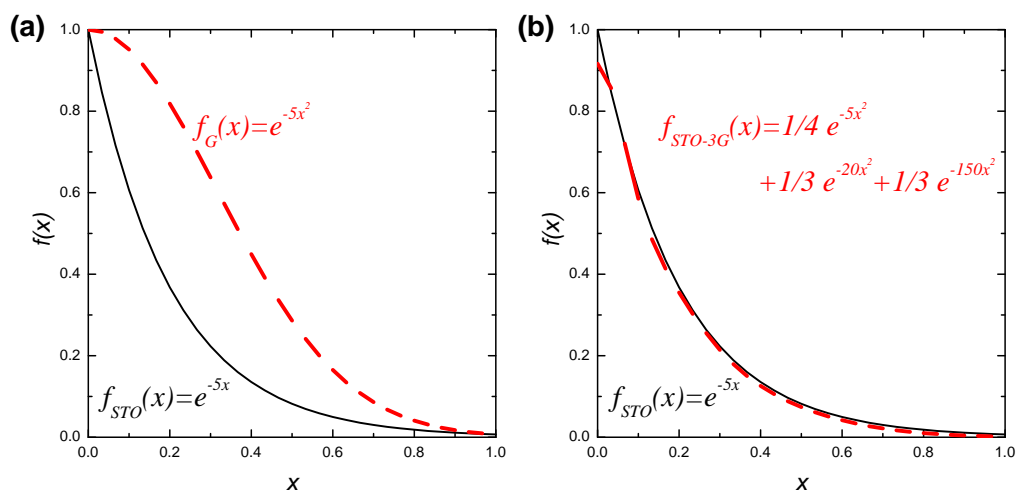


Figure 3.1: (a) Comparison of exponential and gaussian functions. (b) Comparison of the same exponential function and a sum of three gaussians.

to a set of algebraic equations (Roothan-Hall) for $c_{\mu i}$, expressed in matrix form as

$$\mathbf{FC} = \mathbf{SC}\boldsymbol{\varepsilon} \quad (3.21)$$

where

\mathbf{C} is the matrix of MO expansion coefficients;

\mathbf{F} is the Fock matrix, which is the sum of a term representing the energy of a single electron in the field of the bare atomic nuclei and a term describing electron-electron repulsion within an averaged field of electron density;

\mathbf{S} is a matrix describing the overlap of molecular orbitals; and

$\boldsymbol{\varepsilon}$ is a diagonal matrix containing the one-electron energies of each molecular orbital χ_{μ} .

Since the terms within the Fock matrix \mathbf{F} depend upon the electron density, which in turn depends upon molecular wavefunctions defined by the matrix of MO expansion coefficients \mathbf{C} , the Roothan-Hall equations are nonlinear, and must be solved by an iterative procedure termed the *self-consistent field* (SCF) method. Upon convergence of the SCF method, the minimum-energy MOs produce the electric field which generate the same orbitals (hence, the self-consistency).

3.1.3 Basis Sets

In general, a basis set is an assortment of mathematical functions used to solve a differential equation. In quantum chemical calculations, the term *basis set* is applied to a collection of contracted gaussians representing atomic orbitals, which are optimized to reproduce the desired chemical properties of a system. Standard *ab initio* software packages generally provide a choice of basis sets that vary both in size and in their description of the electrons in different atomic orbitals. Larger basis sets include more and a greater range of basis functions. Therefore, larger basis sets can better refine the approximation to the *true* molecular wavefunction, but require correspondingly more computer resources. Alternatively, accurate wavefunctions may be obtained from different treatments of electrons in atoms. For instance, molecules containing large atoms ($Z > 30$) are often modelled using basis sets incorporating approximate treatments of inner-shell electrons which account for relativistic phenomena.

Minimal basis sets contain the minimum number of AO basis functions needed to describe each atom (e.g., $1s$ for H and He; $1s, 2s, 2p_x, 2p_y, 2p_z$ for Li to Ne). An example of a minimal basis set is STO-3G, which uses three gaussian-type functions (3G) per basis function to approximate the atomic Slater-type orbitals (see Figure 3.1 (b)). Although minimal basis sets are not recommended for consistent and accurate predictions of molecular energies, their simple structure provides a good tool for visualising qualitative aspects of chemical bonding. Improvements on minimal basis sets are described below.

Split valence basis sets

In split valence basis sets, additional basis functions (one contracted gaussian plus some primitive gaussians) are allocated to each valence atomic orbital. The resultant linear combination allows the atomic orbitals to adjust independently for a given molecular environment. Split valence basis sets are characterised by the number of functions assigned to valence orbitals. *Double zeta* basis sets use two basis functions to describe valence electrons, *triple zeta* use three functions, and so forth.

Polarised basis sets

Polarisation functions can be added to basis sets to allow for non-uniform displacement of charge away from atomic nuclei, thereby improving descriptions of chemical bonding. Polarisation functions describe orbitals of higher angular momentum quantum number than those required for the isolated atom (e.g., *p*-type functions for H and He, and *d*-type functions for atoms with $Z > 2$), and are added to the valence electron shells. The addition of *p*-orbitals to hydrogen is particularly important in systems where hydrogen is a bridging atom.

Diffuse basis sets

Species with significant electron density far removed from the nuclear centers (e.g., anions, lone pairs and excited states) require diffuse functions to account for the outermost weakly bound electrons. Diffuse basis sets are recommended for calculations of electron affinities, proton affinities, inversion barriers and bond angles in anions.

High angular momentum basis sets

Basis sets with multiple polarisation functions are now practical for many systems and, although not generally required for Hartree-Fock calculations, are useful for describing the interactions between electrons in electron correlation methods (see Section 3.1.4). High angular momentum basis sets augmented with diffuse functions represent the most sophisticated basis sets available.

Examples of basis sets

In the literature, there is a number of established basis sets. In the following some typical examples are given.

Basis sets of Pople *et al.*

STO-3G minimum basis (3 GTOs per STO),

3-21G small 'split-valence' basis (double-zeta valence AO),

6-31G* large 'split-valence' basis, polarized at $X \neq H$,

6-311+G** polarized triple-zeta basis with diffuse functions.

Basis sets of Dunning *et al.*

DZP polarized double-zeta basis,

TZP polarized triple-zeta basis,

TZ2P triple-zeta basis with 2 sets of polarization functions,

TZ2Pf TZ2P + additional f polarization functions.

Correlation-consistent basis sets

cc-pVTZ multiply polarized triple-zeta basis,

cc-pVQZ multiply polarized quadruple-zeta basis,

aug-cc-pVQZ cc-pVQZ + additional diffuse functions.

3.1.4 Electron correlation

Hartree-Fock theory is a single-particle approximation, and therefore cannot adequately treat the correlated motion of electrons that occurs due to electron-electron interactions. Neglect of electron correlation has been blamed for systematic HF errors such as underestimated bond lengths and overestimated vibrational frequencies. Calculations added to HF-SCF theory to remedy these errors are termed *electron correlation* or *post-HF* methods. There are different general types of electron correlation treatments: configuration-interaction (CI) methods, Møller-Plesset (MP) perturbation theory, coupled cluster (CC) theory, and density functional theory (DFT).

Configuration-interaction

A HF wavefunction of a molecule has one determinant; therefore, it can describe only one electronic configuration in a molecule. This approximation is so restrictive that HF theory cannot predict the dissociation of even the simplest molecule, the hydrogen dimer, into its neutral atomic components. However, correct dissociation behaviour is restored when extra configurations, corresponding to electronically excited states, are added to the wavefunction. Configuration-interaction methods incorporate excited state configurations into the wavefunction by constructing new determinants from the original HF determinant. New determinants are created by replacing one or more occupied orbitals with unoccupied (virtual) orbitals of higher energy. The number of replacements within the determinants designates the level of CI. For instance, single substitution (CIS) switches one pair of occupied and virtual orbitals,

$$\begin{aligned}\Psi_{HF} &= |\phi_1, \dots, \phi_j, \dots, \phi_{HOMO}, \phi_{LUMO}, \dots, \phi_i, \dots, \phi_n| \\ \rightarrow \Psi_{CIS} &= |\phi_1, \dots, \phi_i, \dots, \phi_{HOMO}, \phi_{LUMO}, \dots, \phi_j, \dots, \phi_n| \quad (3.22)\end{aligned}$$

and is equivalent to a one-electron excitation⁵. Higher-order calculations include CID (double substitutions), generating determinants where two orbital pairs are switched; CISD, adding singly and double-substituted determinants;

⁵Note, HOMO refers to the Highest Occupied Molecular Orbital, whereas LUMO denotes the Lowest Unoccupied MO.

and CISDT, with single, double and triple excitations. The theoretical limit of this expansion - a full CI calculation - forms the molecular wavefunction as a linear combination of the HF determinant and all possible substituted determinants:

$$\Psi_{full-CI} = a_0 \Psi_{HF} + \sum_{n>0} a_n \Psi_{S,D,T,\dots} \quad (3.23)$$

where the coefficients a_i are determined by minimizing the energy of the total wavefunction. Full CI provides the most complete non-relativistic treatment possible for a molecular system; however, it is extremely computation-intensive, and generally untenable for all but the simplest molecules described by small basis sets.

Møller-Plesset perturbation

For typical molecules, most of the ground-state energy originates from one-electron HF contributions. Møller-Plesset perturbation theory assumes that the effects of electron correlation are minor, and can be described by small corrections (perturbations) to the HF solution. Essentially, MP methods assume that the true molecular Hamiltonian can be divided into two parts:

$$\mathcal{H} = \mathcal{H}_{one-e} + \lambda \hat{P}_{many-e} \quad (3.24)$$

where \mathcal{H}_{one-e} denotes single-electron energy contributions that can be solved exactly by HF-SCF, and \hat{P}_{many-e} represents contributions due to electron correlation. The coefficient λ is used to generate power series expansions of the energy and the molecular wavefunction:

$$E = E^{(0)} + \lambda E^{(1)} + \lambda^2 E^{(2)} + \lambda^3 E^{(3)} + \dots \quad (3.25)$$

$$\Psi = \Psi^{(0)} + \lambda \Psi^{(1)} + \lambda^2 \Psi^{(2)} + \lambda^3 \Psi^{(3)} + \dots \quad (3.26)$$

These series are then substituted back into the molecular Schrödinger equation with the modified Hamiltonian (equation (3.24)), and each term is evaluated in turn. The first two energy terms constitute the HF energy

$$E_{HF} = E^{(0)} + E^{(1)}, \quad (3.27)$$

and are used to evaluate $\Psi^{(1)}$, which is composed of a linear combination of substituted determinants

$$\Psi^{(1)} = \sum_n b_n \Psi_{S,D,T,\dots}, \quad (3.28)$$

with coefficients b_i that are inversely proportional to the difference in energy between the ground state and the associated excited states. That is, substituted wavefunctions close in energy to the ground state make larger contributions to the perturbation expansion. The first-order correction to the wavefunction, $\Psi^{(1)}$, is then used to calculate the second-order correction to the total energy $E^{(2)}$, and so on, back and forth, until the desired order of correction is achieved. Møller-Plesset theory is designated by the order of the perturbative corrections. Since the second-order energy term $E^{(2)}$ is the first-order correction to the HF energy, the designation begins at MP2, and continues with MP3, MP4, MP5, and so forth.

Coupled-Cluster theory

With the innovation of Coupled-Cluster (CC) theory some elegant concepts have been introduced into the quantum chemistry. The essential difference compared to the CI-method is given by the exponential approach for the exact wavefunction:

$$\psi_{CC} = e^{\hat{T}} \psi_{HF}. \quad (3.29)$$

The operator (cluster operator)

$$\hat{T} = \sum_i \hat{T}_i = \hat{T}_1 + \hat{T}_2 + \hat{T}_3 + \dots \quad (3.30)$$

acts on the Hartree-Fock wavefunction ψ_{HF} and generates substitutions of i^{th} order of the reference wavefunction. The operators are defined using creation and annihilation operators (in the language of second quantization). Their operation on ψ_{HF} yields the corresponding p-fold excitations including the associated amplitudes:

$$\hat{T}_1 \psi_{HF} = \sum_a \sum_r t_a^{(r)} \psi_a^{(r)} \quad (3.31)$$

$$\hat{T}_2 \psi_{HF} = \sum_a \sum_{b>a} \sum_r \sum_{s>r} t_{ab}^{(rs)} \psi_{ab}^{(rs)} \quad (3.32)$$

$$\hat{T}_3 \psi_{HF} = \sum_a \sum_{b>a} \sum_{c>b} \sum_r \sum_{s>r} \sum_{t>s} t_{abc}^{(rst)} \psi_{abc}^{(rst)} \quad (3.33)$$

Due to the exponential character of the wavefunction the obtained results are always size-consistent even if the substitution is limited to a certain order (e.g. CCSD account only single and double substitutions through $\hat{T} = \hat{T}_1 + \hat{T}_2$). The CC-theory can be seen as a method adding systematically terms of the perturbation theory. Compared to the pure perturbative approaches -adding all terms up to a certain order- the CC theory combines certain terms of all orders.

CCSD is the standard approach in the field of coupled-cluster theory. The dominant correlation effects are taken into account by the double (D) excitations, and the cost is relatively low to include the single (S) excitations in addition. CCSDT including all triple (T) excitations is the next logical step of approximation. However, the computational effort increases drastically when going from CCSD to CCSDT. Therefore, at present the triple excitations are usually taken into account in approximate forms. Among the many investigated variants the most successful form is CCSD(T): CCSD plus a perturbative treatment of triple excitations, retaining fourth-order terms (MP4) and certain S-T interaction terms of fifth order (MP5)⁶.

Density-functional theory

DFT theory models electron correlation as a functional of the electron density, ρ . The functional employed by current DFT methods partitions the

⁶Note, CCSD(T) is size-consistent, too.

electronic energy via the Kohn-Sham equations [67, 93] into several terms

$$E = E^T + E^V + E^J + E^{XC} \quad (3.34)$$

where E^T is the kinetic energy term (arising from the motion of the electrons), E^V is the potential energy term that includes nuclear-electron and nuclear-nuclear interactions, E^J is the electron-electron repulsion term and E^{XC} is the electron correlation term. All terms except nuclear-nuclear repulsions are functions of the electron density. The terms $E^T + E^V + E^J$ represent the classical energy of the electron distribution, while E^{XC} represents both the quantum mechanical exchange energy, which accounts for electron spin, and the dynamic correlation energy due to the concerted motion of individual electrons. Pure DFT methods calculate E^{XC} by pairing an exchange functional with a correlation functional and so are designated by the choice of combination. For example, BLYP combines Becke's gradient-corrected exchange functional with the gradient-corrected correlation functional of Lee, Yang and Parr [78]. DFT calculations fall into three general categories: local density approximations (LDA), generalized gradient approximations (GGA), and *hybrid* combinations of DFT and Hartree-Fock terms. LDA exchange and correlation functionals only contain terms related to electron density -an approach that works for some bulk materials, but fails to accurately predict properties in isolated molecules. GGA ('nonlocal') functionals contain terms that depend upon both the electron density and the density gradients. The gradient-corrected density functional method BLYP is capable of predicting intramolecular bond dissociation energies to within a few kJ/mol [73]. However, the generalized gradient approximation severely underestimates activation barriers for some reactions due to neglecting of Coulomb *self-interaction* of the electrons [37]. This problem is remedied with hybrid methods that combine Hartree-Fock self-interaction corrections with density functional exchange and correlation. Examples of hybrid methods are B3LYP and B3PW91, where B3 denotes Becke's three-parameter hybrid functional [7], while PW91 and LYP are gradient-corrected correlation functionals of Perdew and Wang [97] and, as above, Lee, Yang and Parr.

Caveats for post-HF methods

Although post-SCF treatments should improve upon Hartree-Fock theory, each of these techniques violates at least one of the fundamental criteria that define *ab initio* methodology. Truncated CI calculations (i.e., anything less than full configuration interaction) are not size-consistent, so comparative CI studies should include added corrections⁷. MP perturbation theory is not a variational technique, and as such does not provide an upper bound

⁷One method, quadratic configuration interaction (QCI), restores size consistency by adding terms, with corrections available up to quadruply excited states: QCISD, QCISD(T) and QCISD(TQ). Coupled cluster methods correct for size-consistency by accounting for simultaneous substitutions in different molecules -a technique useful for modelling chemical reactions.

to the true molecular energy⁸. Finally, DFT contains a bias: the exact functional dependence of E^{XC} upon the electron density is unknown and must be approximated by assuming that ρ has certain properties (e.g., it behaves like a uniform electron gas). Excited-state DFT calculations, which require the application of linear response theory, so far has been limited to atomic systems. These caveats serve as a reminder that although *ab initio* methods are capable of yielding predictions close to experimental results, many of the approximations that make quantum chemical computations feasible are wholly nonphysical. Hence, even the most sophisticated *ab initio* software packages should not be treated simply as *black boxes*.

⁸The second-order term (MP2) is always negative and often overcorrects for electron correlation.

3.2 Theoretical ROVibrational Energies (TROVE)

Very recently Yurchenko *et al.* [132] presented new computational method with an associated computer program TROVE (Theoretical ROVibrational Energies). The program TROVE performs variational calculations of rovibrational energies for general polyatomic molecules of arbitrary structure in isolated electronic states.

Briefly, the Schrödinger equation for the translation, rotation, and vibration of a polyatomic molecule, obtained in the Born-Oppenheimer approximation, expressed in terms of the Cartesian coordinates of the nuclei in a laboratory-fixed axis system, has a very simple form

$$\mathcal{H} = \frac{-\hbar^2}{2m_e} \sum_i \nabla_i^2 + V. \quad (3.35)$$

Here, nucleus i has the mass m_i and the coordinates (R_{iX}, R_{iY}, R_{iZ}) in the chosen laboratory-fixed axis system XYZ , and ∇_i^2 is as given in equation (3.3). V is the Born-Oppenheimer potential energy function and ψ_{trv} is the translation-rotation-vibration wavefunction with the associated translation-rotation-vibration energy E_{trv} . Even though the Schrödinger equation in equation (3.35) has a mathematically simple form, it is very badly suited for actual solution and hence normal- or internal-coordinates are introduced (see Sections 2.2.1 & 2.2.5). However, molecules differing by their number of nuclei and/or by their structure require different internal coordinates to describe their vibrational motion. Therefore, such molecules have very different rotation-vibration Hamiltonian operators. One can hardly imagine a universal set of internal coordinates capable of properly representing arbitrary vibrational motions. It would seem that each type of molecule requires a specific coordinate choice and, consequently, a specific kinetic energy operator and, finally, a specific computer program for computing its rotation-vibration energies. The only coordinates that can be defined in a general manner are the normal coordinates, but they are mostly suited for describing small-amplitude vibrations around a single potential energy minimum and so their applicability is limited.

TROVE is the development of a general computational paradigm, which can be used in a *black box* fashion, for calculating rotation-vibration energies for molecules in isolated electronic states. This computational scheme is applicable for a general molecule of arbitrary structure. It allows the user to make an arbitrary choice of the vibrational coordinates to be used in the kinetic energy operator. This generality is achieved by including the coordinate transformation into the computational process as a numerical procedure.

In TROVE the Hamiltonian operator is expressed as a Taylor series in terms of the internal coordinates, and its eigenvalues and eigenfunctions are obtained in the finite basis representation in terms of a basis set that can be arbitrarily chosen. The coordinate transformation, or rather the momentum transformation, from Cartesian coordinates to the chosen set of vibrational

coordinates is made with the help of Taylor series whose expansion coefficients are computed numerically in a recursive procedure. The scheme is self-contained, i.e., it requires no analytical pre-derivation of the kinetic energy operator.

An important application of the energies and wavefunctions resulting from solutions of the molecular rotation-vibration Schrödinger equation is the simulation of rotation-vibration spectra. To provide this type of theoretical support for experimental high-resolution molecular spectroscopy it is obviously not sufficient to calculate only the molecular vibrational energies. Rotation-vibration energies and wavefunctions must be calculated and, furthermore, these calculations must be carried out for a rotational excitation (given by the angular momentum quantum number J) sufficiently high that experimental spectra can be simulated. In TROVE maximum separation between rotation and vibration is achieved through the use of Eckart conditions [20, 38]. The approach is designed with the aim to be able to access high J values and thus provide energies and wavefunctions for the simulations of realistic rotation-vibration spectra.

In course of this thesis such simulations have been carried out for HSOH in a collaboration with Yurchenko and co-workers. The results aid the interpretation of the torsional splittings observed in the rotational spectra of HSOH as given in Chapter 9.

4

Laboratory Spectroscopy

In course of the investigations presented in this thesis, mainly two experimental setups were employed, the Cologne Terahertz Spectrometer and a commercially available Fourier Transform Infrared (FT-IR) Spectrometer.

The Cologne Terahertz Spectrometer, as described in Section 4.1, is a typical absorption spectrometer with a tunable radiation source, an absorption cell, and a broadband detector. More details concerning this spectrometer can be found for example in [124, 125].

To enhance the operating frequency range of the Cologne Terahertz Spectrometer up to 1.4 THz, a multiplier chain was introduced as part of this work. An introduction to the multiplier principle is given in Section 4.2.

Unlike in conventional spectroscopy, in a FT-IR Spectrometer all frequencies emanating from the IR source impinge simultaneously on the detector. The recorded data must be converted into a spectrum by means of a mathematical operation called Fourier transformation (FT). The principles of the used FT-IR Spectrometer will be described in Section 4.3. Further details on FT-IR Spectroscopy can also be found in the textbooks by Bell [12], Smith [106], as well as Griffiths and de Haseth [51].

4.1 The Cologne Terahertz Spectrometer

The crucial parts of the Cologne Terahertz Spectrometer are the tunable radiation source (Backward Wave Oscillator (BWO)), the harmonic-mixer, the tunable millimeter-wave frequency synthesizer (KVARZ, Nizhnii Novgorod, Russia), and the liquid-He cooled InSb detector (QMC Instruments, Cardiff, UK). A schematic overview of the spectrometer is given in Figure 4.1.

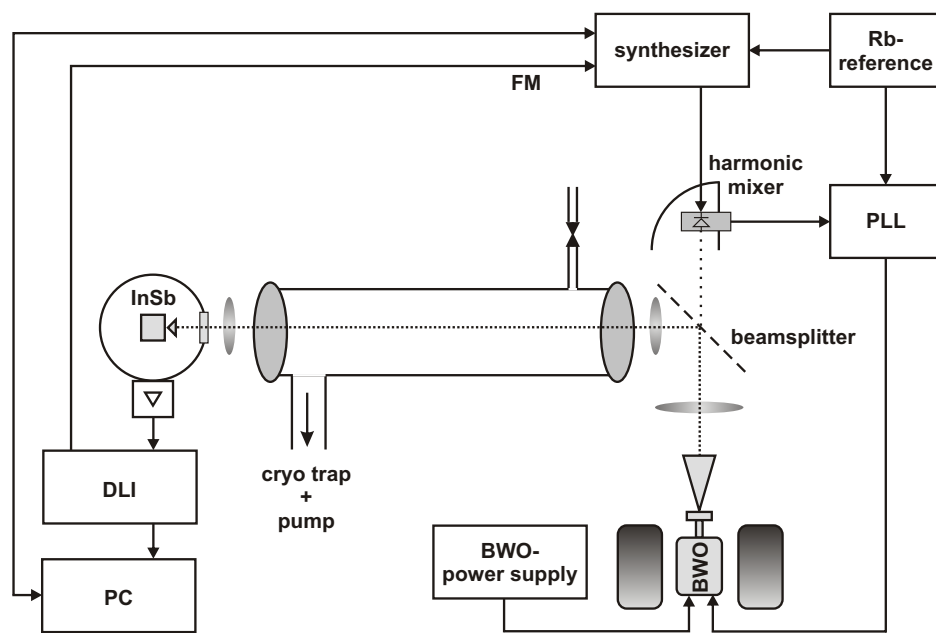


Figure 4.1: Schematic of the Cologne Terahertz Spectrometer. Radiation emitted by the BWO is guided through an absorption cell and detected on a liquid-He cooled InSb hot electron bolometer. Part of the radiation is coupled out and used for frequency stabilization using a phase lock loop.

Backward Wave Oscillators

Backward Wave Oscillators (BWOs) distinguish themselves as radiation sources because of two properties, the wide tunability by about 30% of their nominal frequency and the fairly constant high output power of order 0.5 to 100 mW. The principle of a BWO is briefly explained in the following¹.

Figure 4.2 shows a scheme of a BWO. Inside a BWO an electron beam, emit-

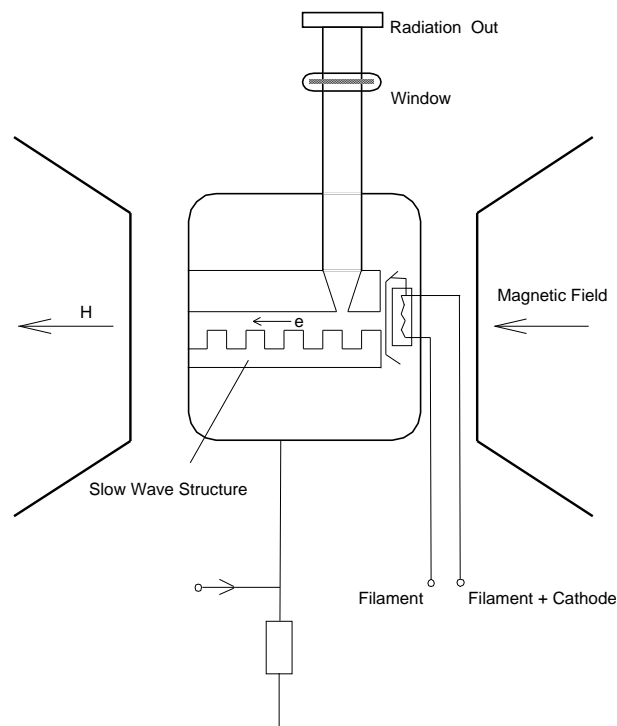


Figure 4.2: Schematic drawing of a Backward-Wave-Oscillator.

ted by a cathode, is guided along a slow-wave microstructure. The beam is focussed by a strong magnetic field generated by placement of the tube between the poles of an electromagnet. While the electrons pass the periodic potential they are accelerated and decelerated and thus electromagnetic radiation is generated. This radiation is coupled out through a small coupling hole into an overmoded waveguide which is directly connected to the radiation output, a conical horn antenna.

The frequency emission of a free running BWO varies from the favored frequency by several MHz on a timescale of approximately 1 minute. This is by far more than the desired precision of a high resolution spectrometer. Thus, a phase stabilization of the BWO has been applied to the Cologne spectrometer setup.

¹For further information see [45, 53, 66, 74]

Phase-Lock-Loop

For phase stabilization and therefore frequency stabilization as well, a small part of the radiation, about 10%, is coupled out by a beamsplitter into a harmonic mixer device. The multiplier-mixer consists of a planar Schottky diode which generates harmonics of two input frequencies

$$\nu_{IF} = \pm m \cdot \nu_{BWO} \pm n \cdot \nu_{Synthesizer}. \quad (4.1)$$

As a frequency reference, a commercially available KVARZ millimeter wave synthesizer is connected to the harmonic mixer. If n and $\nu_{Synthesizer}$ are chosen in an appropriate way, an intermediate frequency ν_{IF} of 350 MHz for the favored BWO frequency ν_{BWO} ($m = 1$) is generated. This intermediate frequency is compared via a Phase Lock Loop (PLL) in phase to a reference signal given by an atomic clock (rubidium (Rb) reference, $\Delta\nu/\nu = 10^{-11}$). Any change in phase causes a voltage error signal which is returned to the BWO by the PLL. In this way of stabilizing an accuracy of a few Hz can be achieved for the desired frequency.

Absorption cell, pumping system and windows

As absorption cells, typically pyrex glass tubes of lengths 1–3 m were used. The deployed windows and lenses consist of Teflon or High Density Polyethylene (HDPE) which have low absorption coefficients in the THz region.

The pumping system consists in general of a rotary vane pump followed by a turbo molecular pump, and pressures of $8 \cdot 10^{-3}$ Pa are possible.

Detectors

As detectors broadband liquid He cooled InSb Hot Electron Bolometers (HEBs) (QMC instruments Ltd., Cardiff, UK) were used. The relaxation time is approximately $1 \mu\text{s}$ enabling a frequency-modulation of the radiation source up to 500 kHz, where 7–20 kHz are typically used during the measurements. Spectra are usually recorded in $2f$ -modulation mode employing a digital lock-in amplifier (DLI) for demodulating the signal. Depending on the expected line width and intensity the amplitude of the modulation frequency has to be optimized.

4.2 Frequency Multipliers

In principle, any nonlinear electronic device could be used as mixer or multiplier. However, in order to achieve reasonable conversion efficiencies and low noise in the terahertz band, only a few types of devices are feasible. GaAs Schottky barrier diodes are at present the best room-temperature solid-state devices for this application². Components based on these devices have set the performance standard for the past several decades. Schottky barrier diodes are preferred due to their inherent simplicity and their lack of any minority carrier storage effects. GaAs is used because it offers an excellent combination of: 1) high mobility, required for terahertz response; 2) a sufficiently large bandgap (and therefore barrier height) to reduce leakage currents; and 3) a fairly mature and cost efficient processing technology.

4.2.1 Design of Frequency Multipliers

The typical design of a frequency multiplier is given by a symmetrically splitted waveguide-block with a diode structure in the middle (splitblock-techniques). The pumping power of the diode is applied through a waveguide network and picked up at the area of maximum field intensity by an antenna (E-probe). The generated harmonics are injected into the output waveguide through a second antenna. A low-pass between the antenna and the diode avoids the propagation of the harmonics in the input waveguide and the resulting power losses.

The first terahertz diodes were Whisker contacted devices, as pioneered by Young and Irwin [131] and later Schneider [81] and Mattauch [111]. More recently planar diodes [25, 61, 83] have successfully been developed and integrated diode circuits are now available. There are also other materials and diode structures beginning to occupy niche applications within the terahertz frequency band. For example, heterostructure barrier varactor (HBV) diodes based on InAlAs/InP materials have been used to achieve frequency multiplication in the 100–500 GHz frequency band [31, 88, 128]. Also, a group at the TU Munich in Germany has recently developed a tripler circuit with excellent performance using nonuniform doping profiles and a blocking barrier contact [75].

However, in the experimental part of this thesis a chain of planar diodes has been employed. Hence, only some introductory information on this device is given.

²If cryogenic cooling is allowed, superconductive mixers yield far better noise performance than is possible with a semiconductor diode.

Planar Diodes

In the planar mounting form the filter and diode structures are built by photolithographic processes. Below the filters the substrate is partly removed to minimize dielectric losses. The structure is held by two $1\ \mu\text{m}$ thick wing-pairs of gold (beam-leads). During the construction of the multiplier these pairs are conductive clamped in-between the waveguide-blocks. As components of the filter structure the beam-leads are well defined in their lengths and precisely adjusted to suppress the undesired harmonics (Idler-frequencies); as a result the width of the substrate-channel is also specified. In Figure 4.3 the basic model of a planar Schottky diode is depicted.

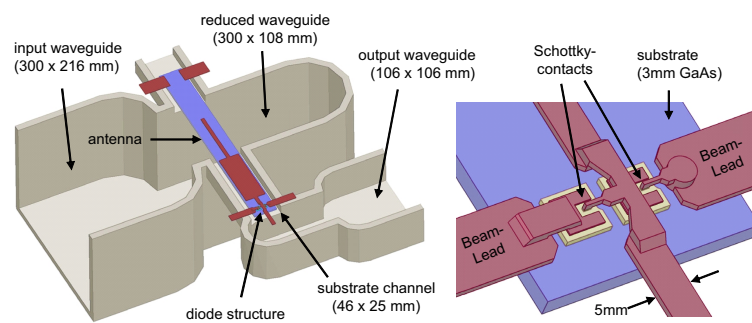


Figure 4.3: Example of a planar multiplier based on two Schottky diodes optimized for the frequency of 1.9 THz [84, 98]. On the right hand side the diode structure is shown (enlarged by a factor of 10). By reducing the height of the waveguide the impedance adaption between waveguide and antenna is optimized.

Multiplier Chain for the THz-region

For the measurements in Section 9.1 an active multiplier chain³ (see Figure 4.4) with an output reaching from 1.1 to 1.7 THz, has been introduced. This chain is commercially available and has been manufactured by Virginia Diodes, Inc.. The input SMA connector requires a signal of only a few milliwatts near 18 GHz. The signal is at first frequency doubled and amplified. It is then multiplied by a factor of four by a pair of doublers integrated into a single housing and then by a factor of nine by a pair of frequency triplers. The output is therefore 72 times the input frequency. Typical power levels are of order 10–25 μW , depending on the exact frequency⁴.

³The design of this multiplier chain is in the planar mounting form.

⁴For further information on this multiplier device see [28, 61].

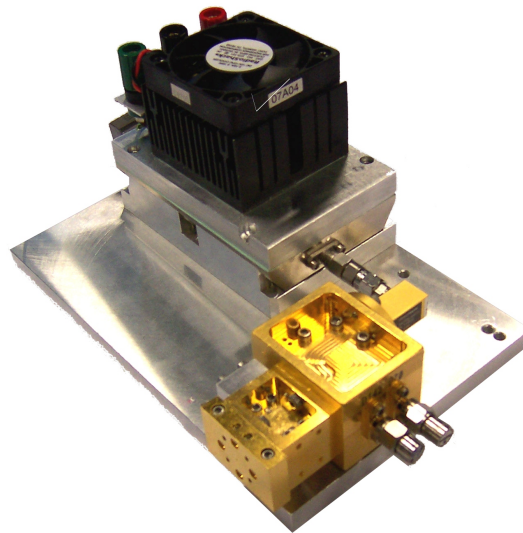


Figure 4.4: All-solid-state terahertz source. The active multiplier chain increases the frequency of a standard commercial sweeper to the terahertz band through a single power amplification and a series of multiplication steps. The final multiplication factor is 72 and power levels of 10–25 μW are achieved (1.1–1.7 THz).

4.3 Fourier Transform Infrared Spectrometer

The working principle of a Fourier Transform (FT) Spectrometer is completely different to the one introduced in the Cologne Terahertz Spectrometer (see Section 4.1). In a FT Spectrometer not only a simple frequency element is recorded at a time but all wavelengths of light are allowed to pass through the sample at the same time and are recorded simultaneously. The basic principles of a FT instrument and how a spectrum is obtained from the detector signal is briefly discussed in the following.

The essential part of optical hardware in a Fourier Transform Infrared (FT-IR) Spectrometer is the interferometer (see Figure 4.5). The main compo-

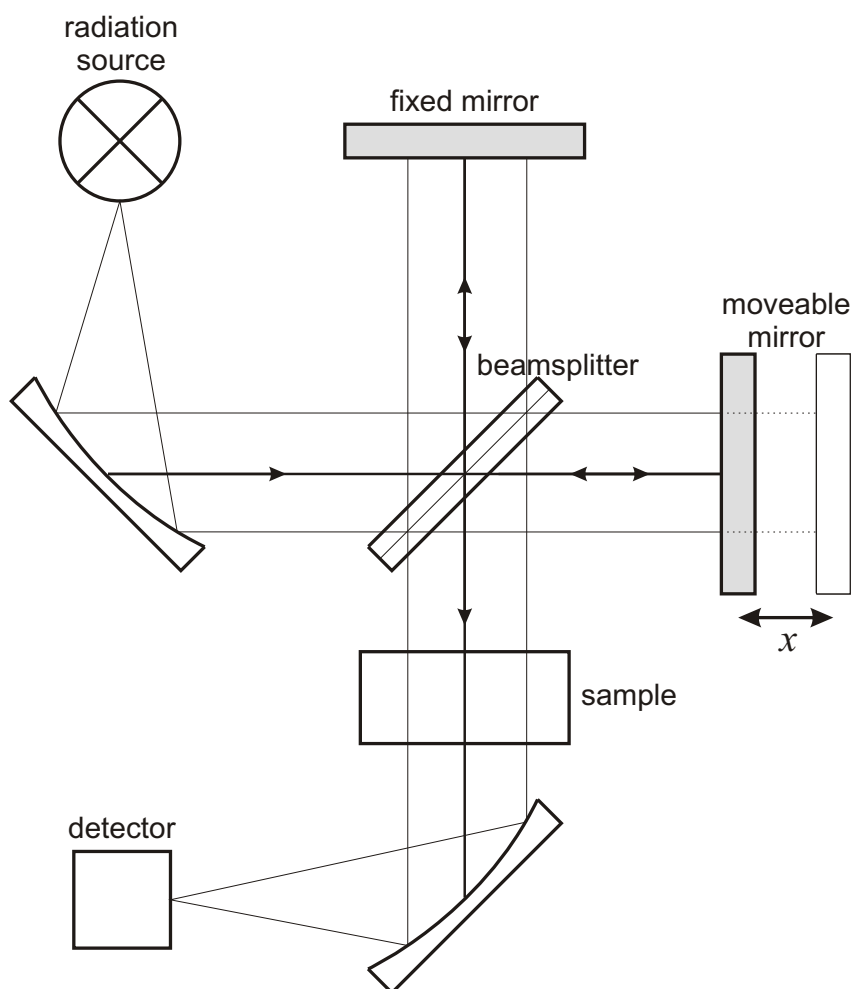


Figure 4.5: Optical schematic of a classic Michelson interferometer, which consists of a fixed, a movable mirror, and a beamsplitter.

nents of an interferometer are the beam splitter, a fixed, and a moving mirror, as well as a detector. Radiation emitted from the source is partly transmitted through the beamsplitter to a movable mirror. The other part of the radi-

ation is reflected onto a fixed mirror. These two beams are reflected from the mirrors and recombined at the beamsplitter. The beam from the moving mirror has traveled a different distance than the beam from the fixed mirror. When the beams are combined an interference pattern is created, since some of the wavelengths recombine constructively and some destructively. The beam leaving the interferometer passes through a sample compartment and is finally focussed onto the detector. The quantity actually measured by the detector is thus the intensity $I(x)$ of the combined IR beams as a function of the moving mirror displacement x , the so called interferogram

$$I(x) = \int_0^{\infty} S(\nu) \cos(2\pi\nu x) d\nu, \quad (4.2)$$

where $\nu = \frac{1}{\lambda}$ is the wavenumber and $S(\nu)$ is the intensity of the monochromatic line located at wavenumber ν .

However, the interferogram is sampled (see Figure 4.6) and consists of N

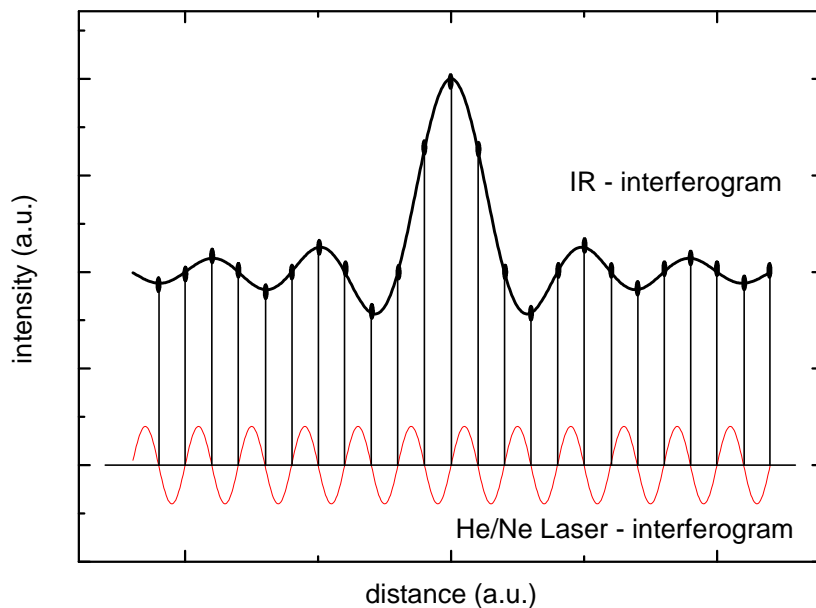


Figure 4.6: Schematic of data acquisition: The zero crossing of the interference pattern of a laser source define the positions where the IR-interferogram is sampled.

discrete, equidistant points

$$I(n \cdot \Delta x) = \frac{1}{N} \sum_{n=0}^{N-1} S(k \cdot \Delta \nu) \exp(-i2\pi nk/N) \quad (4.3)$$

where the continuous variables x and ν have been replaced by $n \cdot \Delta x$ and $k \cdot \Delta \nu$, respectively. The spacing $\Delta \nu$ in the spectrum is related to Δx by⁵

$$\Delta \nu = \frac{1}{N \cdot \Delta x}. \quad (4.4)$$

The interferogram contains the basic information on frequencies and intensities characteristic of a certain spectrum but in a form that is not directly interpretable. Thus, the information is converted to a more familiar form, the power spectrum $S(k \cdot \Delta \nu)$, using Discrete Fourier Transform methods

$$S(k \cdot \Delta \nu) = \sum_{n=0}^{N-1} I(n \cdot \Delta x) \exp(i2\pi nk/N). \quad (4.5)$$

4.3.1 Resolution

In a FT-IR spectrometer, the resolution is increased by increasing the optical retardation, that is, by increasing the moving distance of the second mirror. A relationship between resolution and optical retardation can empirically be derived by considering a spectrum made up of two sharp bands. Each band is at a distinct frequency and generates a sinusoidal signal. The total signal at the detector is the sum of the two signals. If the two spectral frequencies are relatively far apart, the resulting signals are quite different and only a short movement of the mirror is needed to measure a complete cycle of the pattern created by the addition of the two waveforms. On the other hand, if the two frequencies are closer together, the interferometer needs to scan a larger distance to measure a full cycle of the addition pattern. The relationship between spectral line spacing and the interferogram is $R = 1/d$ where R is the spectral resolution in wavenumbers and d is the optical retardation in centimeters. Thus, the distance of mirror travel (retardation) must be doubled to improve the instrument's resolution by a factor of two.

4.3.2 Apodization

It is obvious, that the scanning distance of the moving mirror is limited. Since the collected data set is finite, the transformation of that data set contains the effects of the data set start and end. The data set beginning and ending correspond to what is known as a boxcar function. This boxcar function is part of the collected data and is therefore transformed along with the spectral information in the interferogram. The transformation of the boxcar function is a $\text{sinc}(x)$ function. When the $\text{sinc}(x)$ function is convolved with

⁵Note, that the resolution $\Delta \nu$ is not enhanced by reducing the distance of succeeding sampling points Δx but by increasing the number N of points (see Section 4.3.1). The distance of succeeding sampling points is related to the free spectral range of the spectrometer.

the spectral data by the Fast Fourier Transform (FFT), ringing at the edges of spectral absorption bands results. Assigning less weight to the data set start and end with, for example, a triangular function, can reduce this baseline ringing. The tradeoff is a reduction in the resolution of the spectrum. The effects of apodization during the Fourier transformation require that all spectra are processed by the same function when quantitative measurements, such as spectral subtraction, are performed.

For more details on the mathematics involved in the classical and discrete Fourier transformation, Resolution, and Apodization, as well as details on here not discussed topics such as Zerofilling, Undersampling, Aliasing, etc. the textbooks by Bell [12], Smith [106], and Griffiths and de Haseth [51] present a thorough and rigorous treatment.

4.3.3 Bruker IFS 120HR

For the spectra measured in course of this thesis, a Bruker IFS 120HR has been employed. The schematical setup of this FT Spectrometer is shown in Figure 4.7.

The best resolution achievable is 0.002 cm^{-1} . Depending on the radiation source, windows, beamsplitter, and detector used the frequency range in between $20\text{--}42000\text{ cm}^{-1}$ can be covered. A broad overview on the best choice for the experimental equipment of the experimental setup in different frequency ranges is given amongst others in [135].

In course of this work data points have been covered in four spectral regions, $380\text{--}825\text{ cm}^{-1}$, $600\text{--}1400\text{ cm}^{-1}$, $2000\text{--}2900\text{ cm}^{-1}$, and $1800\text{--}3850\text{ cm}^{-1}$. An overview how the Bruker 120HR interferometer was equipped in the different spectral regions is given in Table 4.1.

To enhance the sensitivity of the experiment a White-type [117] multireflection cell with a total pathlength adjusted to 40 m was attached to the FT-IR Spectrometer. This cell was equipped with KBr windows. As pumping system a two-stage rotary pump ($65\text{ m}^3\text{h}^{-1}$) has been employed.

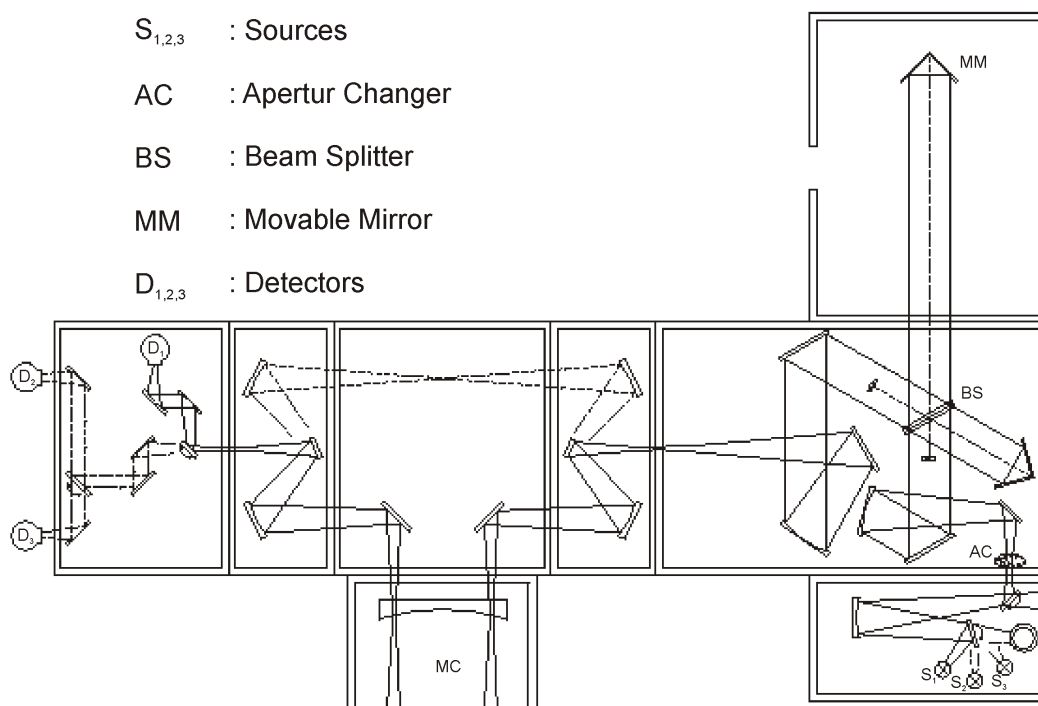


Figure 4.7: Schematic sketch of the Bruker IFS 120HR [18]. Polychromatic radiation from a suitable source $S_{1,2,3}$ enters a Michelson interferometer where it is split (BS) into two coherent beams. One of these beams reaches a moveable mirror (MM). During the movement the optical path difference of the two beams is scanned between 0 and the maximum optical path difference. The two re-combined beams interfere, pass either through the internal sample compartment or through an external absorption cell (MC) with the gaseous sample. Finally the radiation reaches one of the different detectors $D_{1,2,3}$ and an interferogram is recorded.

Table 4.1: Equipment employed in the experimental part of this work for the FT-IR Spectrometer IFS 120HR at different spectral regions.

spectral region	radiation source	beamsplitter	detector
1800–3850 cm^{-1}	100 W tungsten halogen	KBr	1-N ₂ cooled InSb
2000–2900 cm^{-1}	100 W tungsten halogen	CaF ₂	1-N ₂ cooled InSb
600–1400 cm^{-1}	globar	KBr	1-N ₂ cooled MCT600
380–825 cm^{-1}	globar	3.5 mm Mylar	1-He cooled Cu/Ge

5

Synthesis of 1-oxadisulfane (HSOH) and its isotopologues

The first evidence on the formation of HSOH, either known as 1-oxadisulfane or hydrogen thio-peroxide, was obtained by matrix IR-spectroscopy [105], where the molecule was synthesized by photolysis of ozone (O_3) and hydrogen sulfide (H_2S). In addition, HSOH was generated from a H_2S/N_2O mixture in a chemical ionization source and detected in neutralization-reionization mass spectrometric (NR-MS) experiments [64].

Nevertheless, gas-phase studies on HSOH were long time impeded due to the problem of synthesizing this unstable species in sufficient amounts. As recently as in 2001, the breakthrough for gas-phase detection in the microwave and mid-infrared region was achieved by finding a synthesis for HSOH via flash vacuum pyrolysis of di-*tert*-butyl sulfoxide [8, 10, 123] and for the doubly deuterated species DSOD via *rf*-discharge of D_2O and D_2S [9, 19]. In the following, the synthesis of HSOH via pyrolysis of di-*tert*-butyl sulfoxide and the production of HSOD via *rf*-discharge of pure sulfur (S_8) and HDO are explained briefly. A detailed overview of the different pathways for synthesizing HSOH and its isotopologues is given in the PhD-thesis by Esser [39]. The discussion on the interstellar chemistry presented in Section 5.3 is based on unpublished results by Herbst *et al.* [55].

5.1 Synthesis of 1-oxadisulfane by flash vacuum pyrolysis of di-*tert*-butyl sulfoxide

The synthesis of HSOH by flash vacuum pyrolysis of di-*tert*-butyl sulfoxide proceeds in two steps (see Figure 5.1). Beckers *et al.* [8] reported the formation of *tert*-butyl acid (*t*BuSOH) by elimination of 2-methylpropene (C_4H_8) being the dominant reaction up to $500^\circ C$. By increasing the pyrolysis temperature from $500^\circ C$ to $1100^\circ C$ the intermediate *t*BuSOH may decompose by 2-methylpropene elimination into HSOH.

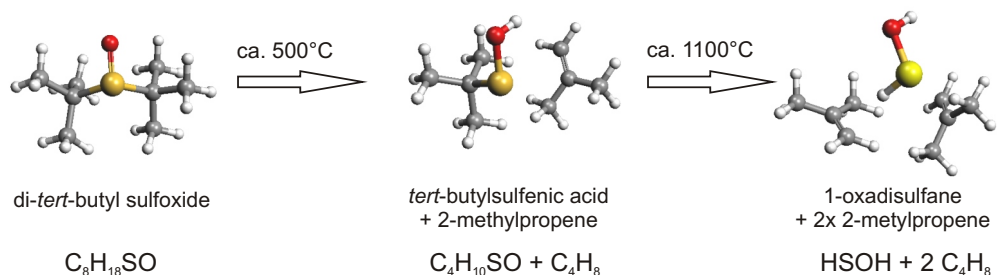


Figure 5.1: Synthesis of HSOH via pyrolysis of di-*tert*-butyl sulfoxide.

In the first step no evidence for the formation of the elusive S-protonated isomer *t*Bu(H)SO has been found. This result is in contrast to previous reports by Davis and Billmers [32] but in agreement with the results of the quantum chemical calculations by Beckers *et al* [8]. In the second step not only HSOH is formed but also its energetically least stable isomer H₂OS. H₂OS may either reversibly rearrange into HSOH or decompose into H₂O and most probably S(¹D) (see Figure 5.2). The reversible rearrangement between HSOH and H₂OS also opens an unimolecular decomposition channel for HSOH.

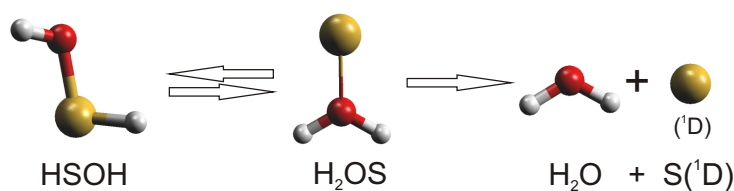


Figure 5.2: Decomposition route of HSOH. (see [8])

The precursor di-*tert*-butyl sulfoxide has been synthesized by selective oxidation of di-*tert*-butyl sulfide with hydrogen peroxide/selenium dioxide (see Drabowicz and Mikolajczyk [30]).

5.2 Synthesis of the single deuterated 1-oxadisulfane (HSOD) by *rf*-discharge of pure sulfur (S₈) and HDO

In course of the present work on HSOD, a novel pathway of synthesizing the single deuterated species was introduced. A constant flow of HDO, from a stoichiometric mixture of H₂O and D₂O leading to a ratio H₂O:HDO:D₂O = 1:2:1, was used and a small vessel containing elementary sulfur powder was inserted into the glas-tube near a *rf*-discharge region. HSOD was measured *in-situ* through the resulting *rf*-discharge plasma. During the experiments it was found that the amount of HSOD tremendously increased at zero gas flow. For most of the measurements the cell was thus filled to constant water pressures of 2-3 Pa and highest yields of HSOD were achieved at a discharge power of 25 W. The absorption signals disappeared immediately after switching off the *rf*-plasma and appeared as soon as the discharge was switched on, indicating the residence time of HSOD to be fairly short -less than some hundred milliseconds- under these conditions. Recently, Beckers *et al.* discussed various thermal decomposition routes of HSOH and found H₂O and elementary sulfur to be the by far favored products of the bidirectional reaction $\text{HSOH} \rightleftharpoons \text{H}_2\text{O} + \text{S}$ [8]. This also seems to hold true for HSOD produced in a *rf*-plasma and leads to a constant concentration of HSOD over hours, supposed that stable plasma conditions are achieved.

5.3 Synthesis of HSOH in the interstellar medium

The HSOH molecule can be thought of as a hydrogenated form of the SO radical. This radical is a common molecule in dense interstellar clouds (see Table 5.2), of which the gas-phase mainly consist of molecular hydrogen. In Table 5.2 it becomes apparent that the compounds containing sulfur are over-represented, taking into account that sulfur occupies the 10th place in the cosmical abundance -after Fe, Si, and Mg (see Table 5.1).

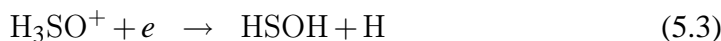
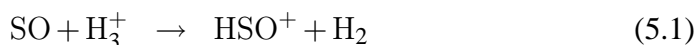
Since oxadisulfane is built of only four atoms -it bears two atoms of hydrogen (1st abundant element), then oxygen (3rd abundant element), and the very sulfur- there is some evidence that HSOH is build in sulfur containing regions of the interstellar medium [33, 34].

Table 5.1: Cosmic abundance of the elements normalized to Si = 1.00×10^6 (see reference [23]).

Element	Symbol	Abundance
Hydrogen	H	3.18×10^{10}
Helium	He	2.21×10^9
Oxygen	O	2.15×10^7
Carbon	C	1.18×10^7
Nitrogen	N	3.74×10^6
Neon	Ne	3.44×10^6
Magnesium	Mg	1.016×10^6
Silicon	Si	1.00×10^6
Iron	Fe	8.3×10^5
Sulfur	S	5.0×10^5
Argon	Ar	1.172×10^5
Calcium	Ca	7.21×10^4
Aluminium	Al	8.5×10^4
Sodium	Na	6.0×10^4
Nickel	Ni	4.80×10^4
Chromium	Cr	1.27×10^4
Phosphorus	P	9600
Manganese	Mn	9300
Chlorine	Cl	5700
Potassium	K	4200
Titanium	Ti	2775
Fluorine	F	2450
All other elements		5069

Note that interstellar chemistry can not be assumed to obey the laws of classical organic chemistry; the gas-phase chemistry that occurs under the low temperatures (typically 10 K) of interstellar clouds is dominated by ion-molecule reactions, although neutral-neutral reactions involving at least one radical can also be important [56]. Reactions requiring the overcoming of activation energy barriers as well as all endothermic reactions do not play a significant role in this chemistry, thus.

Ions are produced via cosmic ray bombardment of the clouds. The initial ionization of molecular hydrogen to form H_2^+ is followed immediately by reaction of this ion with H_2 to form H_3^+ , which is an abundant interstellar ion. One possibility for building HSOH is the sequence of reactions:



but this pathway is uncertain due to the lack of knowledge on the structure, energetics, and reactivity of the ions HSO^+ and H_3SO^+ . In addition, the radiative association to form H_3SO^+ is undoubtedly a slow reaction. Still, unless it is three-body reaction in nature, the production of HSOH in a laboratory discharge argues that there is some effective route to the formation of this species in the weak plasma of interstellar clouds.

Another possibility is a synthesis on the *surface* of interstellar dust particles or grains. Such particles, which are approximately $0.1 \mu\text{m}$ in size and constitute approximately 1% of the mass of interstellar clouds, are either siliceous or carbonaceous in nature. They are known to provide a surface on which atomic hydrogen is converted into its molecular form, most likely via a diffusive, or Langmuir-Hinshelwood, mechanism in which weakly bound H atoms manage to find one another and to form a chemical bond by release of energy to the dust particle [126]. It is entirely possible that HSOH can be produced from gas-phase SO, landing on an interstellar grain, via successive addition of H atoms adsorbed on the same grain. Hydrogen atoms are also present in clouds, despite the greater abundance of the molecular form, since cosmic rays convert a small portion of the latter back to the atomic form. The first hydrogenation produces a mixture of two radicals:



which is presumably analogous to the better studied hydrogenation of CO into the HCO radical [126]. In course of this thesis the structure and energy of both HOS and HSO have been calculated and the former is found to be lower in energy by approximately 10 kcal/mol^1 . The HOS and HSO radicals can be further hydrogenated into HSOH:



¹Calculated by employing the program package Gaussian [43] at the MP2/cc-pVTZ level of theory.

Table 5.2: Interstellar and circumstellar molecules (as of 06/2008).

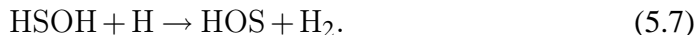
2 atoms	3 atoms	4 atoms	5 atoms	6 atoms
H ₂	C ₃	c-C ₃ H	C ₅	C ₅ H
AlF	C ₂ H	l-C ₃ H	C ₄ H	l-H ₂ C ₄
AlCl	C ₂ O	C ₃ N	C ₄ Si	C ₂ H ₄
C ₂	C ₂ S	C ₃ O	l-C ₃ H ₂	CH ₃ CN
CH	CH ₂	C ₃ S	c-C ₃ H ₂	CH ₃ NC
CH ⁺	HCN	C ₂ H ₂	H ₂ CCN	CH ₃ OH
CN	HCO	NH ₃	CH ₄	CH ₃ SH
CO	HCO ⁺	HCCN	HC ₃ N	HC ₃ NH ⁺
CO ⁺	HCS ⁺	HCNH ⁺	HC ₂ NC	HC ₂ CHO
CP	HOC ⁺	HNCO	HCOOH	NH ₂ CHO
SiC	H ₂ O	HNCS	H ₂ CNH	C ₅ N
HCl	H ₂ S	HOCO ⁺	H ₂ C ₂ O	l-HC ₄ H (?)
KCl	HNC	H ₂ CO	H ₂ NCN	l-HC ₄ N
NH	HNO	H ₂ CN	HNC ₃	c-H ₂ C ₃ O
NO	MgCN	H ₂ CS	SiH ₄	H ₂ CCNH (?)
NS	MgNC	H ₃ O ⁺	H ₂ COH ⁺	
NaCl	N ₂ H ⁺	c-SiC ₃	C ₄ H ⁻	
OH	N ₂ O	CH ₃	HC(O)CN	
PN	NaCN	C ₃ N ⁻		
SO	OCS	PH ₃ (?)		
SO ⁺	SO ₂			
SiN	c-SiC ₂			
SiO	CO ₂			
SiS	NH ₂			
CS	H ₃ ⁺			
HF	H ₂ D ⁺ , HD ₂ ⁺			
SH	SiCN			
HD	AlNC			
FeO (?)	SiNC			
O ₂	HCP			
CF ⁺	CCP			
SiH (?)				
PO				
7 atoms	8 atoms	9 atoms	10 atoms	11–13 atoms
C ₆ H	CH ₃ C ₃ N	CH ₃ C ₄ H	CH ₃ C ₅ N	HC ₉ N
CH ₂ CHCN	HC(O)OCH ₃	CH ₃ CH ₂ CN	(CH ₃) ₂ CO	CH ₃ C ₆ H
HC ₅ N	CH ₃ COOH	(CH ₃) ₂ O	(CH ₂ OH) ₂	C ₆ H ₆ (?)
CH ₃ CHO	C ₇ H	CH ₃ CH ₂ OH	CH ₃ CH ₂ CHO	C ₂ H ₅ OCH ₃ (?)
CH ₃ NH ₂	H ₂ C ₆	HC ₇ N		HC ₁₁ N
c-C ₂ H ₄ O	CH ₂ OHCHO	C ₈ H		
H ₂ CCHOH	l-HC ₆ H (?)	CH ₃ C(O)NH ₂		
C ₆ H ⁻	CH ₂ CHCHO (?)	C ₈ H ⁻		
CH ₃ C ₂ H	CH ₂ CCHCN	C ₃ H ₆		
	H ₂ NCH ₂ CN			

l indicates linear molecules; c indicates cyclic molecules.

? indicates a questionable or (probable) tentative detection.

Species containing sulfur are marked in yellow.

Although HSOH can probably be synthesized in this manner, it is likely destroyed rapidly by a subsequent exothermic reaction with atomic H:



In addition, for gas-phase detection the HSOH molecule must desorb from the surface of a dust particle. Although such desorption is facile for H₂, which is able to evaporate at 10 K given its weak binding, it is not at all clear that the same holds true for HSOH. Indeed, it is likely that any HSOH produced on the surfaces of dust particles can only desorb efficiently when temperatures rise due to the onset of star formation in the interstellar clouds.

5.4 Conclusion and Discussion

Besides the well established way of synthesizing HSOH via the pyrolysis of di-*tert*-butyl sulfoxide a new production method for HSOH and its isotopologues via *rf*-discharge of water (H₂O, D₂O, and HDO) and pure sulfur (S₈) has been introduced. Surprisingly, no evidence for the production of the second single deuterated isotopologue DSOH was found.

The mechanism involved in the *rf*-discharge reaction $\text{HSOH} \rightleftharpoons \text{H}_2\text{O} + \text{S}(^1\text{D})$ is not clarified in detail. Goumri *et al.* [50] found no evidence for barriers to the following insertion reaction:



In Figure 5.3 the potential energy surface -based on total energies that exclude zero point energies- calculated at the UMP2=full/6-31G(d) level of theory (see [50]) is depicted. If the assumption of H₂OS being an intermediate state in the *rf*-discharge reaction $\text{HSOH} \rightleftharpoons \text{H}_2\text{O} + \text{S}(^1\text{D})$ holds true, there is a reaction-barrier of 43 kJ/mol for the formation of HSOH². Taking into account quantum mechanical tunneling it is well known (see e.g. [71, 82]), that the reaction rate $k(\text{H})$ for the 1,2-H migration is significantly enhanced compared to the rate $k(\text{D})$ for the 1,2-D shift. Therefore the production of HSOD should be favored by this synthesis pathway. Obviously one has to verify H₂OS as an intermediate in the reaction path. It is hoped that this study will stimulate further investigations in this field.

In Section 5.3 possible synthesis pathways for HSOH in the interstellar medium are discussed. Following the given argumentation the most likely place to search for HSOH in the interstellar medium is in a star-forming region. Based on similar arguments for HOOH [52], Herbst *et al.* [55] estimated that a gas-phase fractional abundance of HSOH of up to 10⁻¹⁰ of the abundance of H₂ can be found in selected star-forming regions known as hot cores; such an abundance might be detectable by sensitive methods.

²Calculations carried out in course of this thesis show that the activation barriers for the reactions HDOS → HSOD, DSOH are of same order.

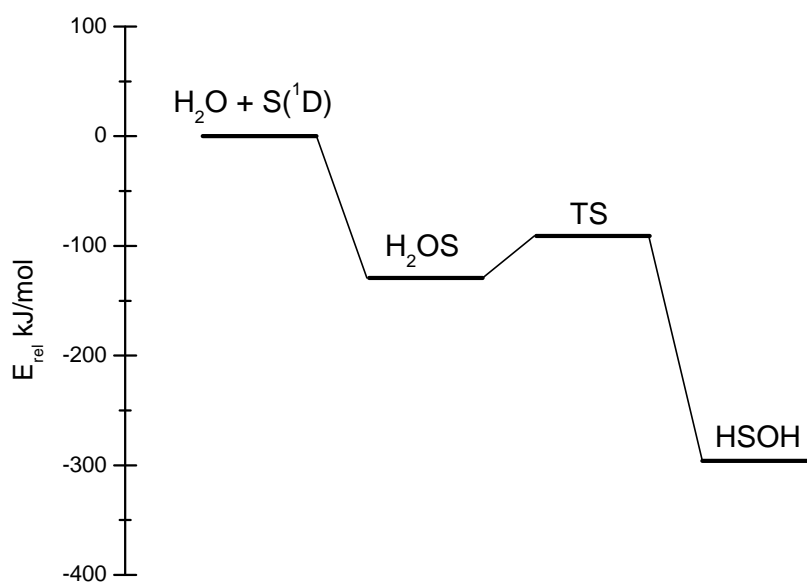


Figure 5.3: Potential energy surface, showing energies relative to $\text{H}_2\text{O} + \text{S}(^1\text{D})$. By TS the transition state is denoted. The energy values are taken from reference [50].

6

Rotational torsional spectrum of singly deuterated 1-oxadisulfane, HSOD

In this chapter the first high resolution measurements on singly deuterated 1-oxadisulfane, HSOD, are reported. As pointed out in Section 2.4 it is necessary to have data from at least $(N - 1)$ isotopologues of an N atom counting molecule to be able to determine the molecular structure without the need of supplementary data from other sources.

In 2003 Winnewisser *et al.* [123] recorded the first rotationally resolved spectra of HSOH and its isotopologue H^{34}SOH in natural abundance. In the same year, the authors also succeeded in recording the first gas phase spectra of the doubly deuterated species DSOD [9]. The experimental studies on DSOD were extended to higher frequencies by Brünken *et al.* [19] who measured the transitions of the rQ_3 -branch at 653 GHz.

In course of this work spectroscopic data of HSOD have been recorded -by employing the Cologne Terahertz Spectrometer (see Section 4.1)- with the aim to derive precise molecular parameters and hence to be able to determine the molecular structure of 1-oxadisulfane for the first time¹.

6.1 Synthesis of HSOD: Elimination of by-products

As discussed in Chapter 5, HSOD has been synthesized in a *rf*-plasma of HDO and pure sulfur. The investigation of this novel way to synthesize the elusive species HSOH and its deuterated isotopologues was a part of this thesis in a collaboration with the Chemistry Department of the University of Cologne (see on this [39]). Apart from HSOD many other species are formed in the *rf*-plasma, among them are mainly sulfur containing molecules

¹For structure calculation the new HSOD data as well as the data of HSOH, H^{34}SOH (see Section 9.1), and previously published data from DSOD [19] have been used (see Chapter 7).

such as H_2S , S_2O , SO_2 , SO but also HSOH and DSOD due to the presence of H_2O and D_2O . To assign spectral lines of HSOD, spectra with pure H_2O and D_2O , respectively, have been recorded to distinguish solely hydrogen and deuterium containing molecules from mixed products.

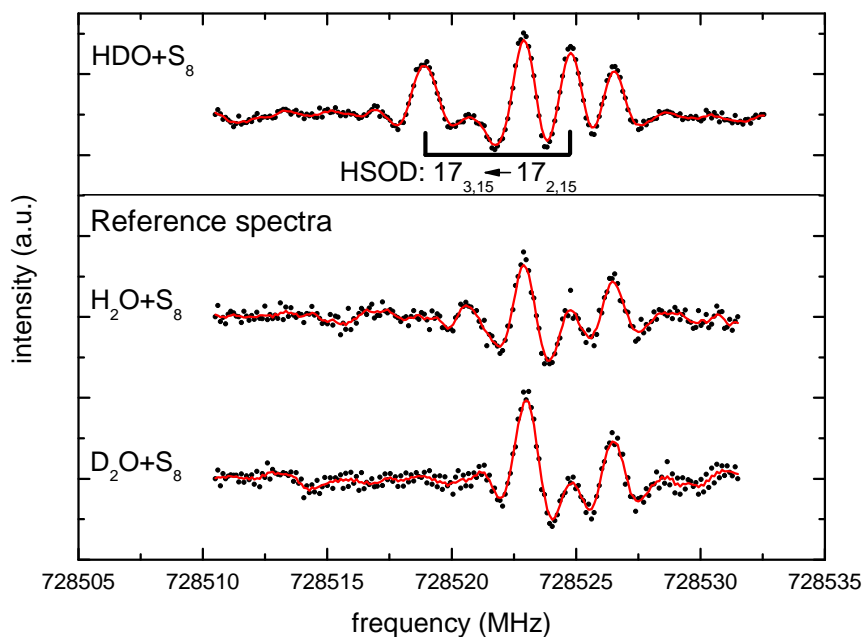


Figure 6.1: Spectrum and reference spectra of discharge generated HSOD. In the upper trace the discharge spectrum of HDO and pure sulfur is depicted. By comparing this spectrum to the reference spectra byproducts could be assigned. The lines not belonging to by-products are the $17_{3,15} \leftarrow 17_{2,15}$ transition of HSOD which splits into a doublet due to the internal rotation tunneling.

Transitions which belong to HSOD disappeared completely under these conditions. Figure 6.1 shows a typical part of the recorded discharge spectra. At the top the spectrum received with the discharge of HDO and pure sulfur is depicted, while on the lower traces the reference spectra recorded with H_2O and D_2O , respectively, are shown. The displayed lines which do not belong to byproducts are assigned to the $17_{3,15} \leftarrow 17_{3,15}$ transition of HSOD splitting into a doublet due to the internal rotation tunneling.

6.2 rQ_2 -branch of HSOD at 729 GHz

The $rQ_{K_a''}$ -branches of an asymmetric rotor exhibit characteristic patterns which allow for the unambiguous identification of new molecular species. The

perpendicular spectrum of an almost accidental symmetric rotor has prominent Q -branches at frequencies of approximately $(A - (B + C)/2)(2K_a'' + 1)$, where K_a'' has the values $0, 1, 2, \dots$. The location of the bandheads of the lowest branches of HSOD $-rQ_{0,1,2}$ - were derived from *ab initio* calculations to be at around 146, 438 and 729 GHz, respectively. In course of this thesis, the spectral range from 716 to 772 GHz has been searched for rQ_2 transitions of HSOD employing the Cologne Terahertz Spectrometer (see Section 4.1). Figure 6.2 shows measured c -type transitions near the band center of the rQ_2 -branch.

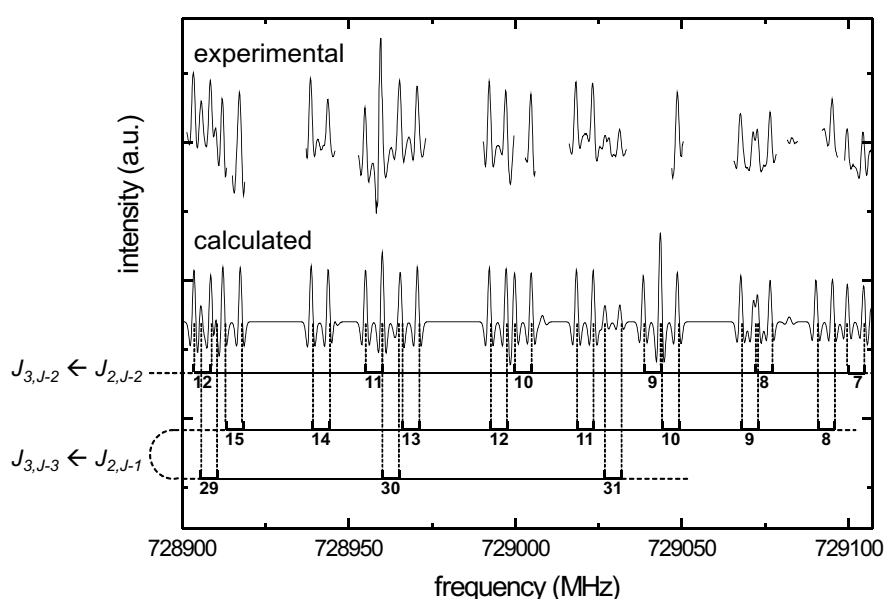


Figure 6.2: Band-head region of the rQ_2 -branch of HSOD. At the top experimental data are shown. A calculated spectrum and the assignment of the c -type transitions for both asymmetry components ($J_{3,J-2} \leftarrow J_{2,J-2}$ in the upper trace, $J_{3,J-3} \leftarrow J_{2,J-1}$ in the lower trace) are mapped below the experimental data. The J -independent torsional splitting for each transition is clearly to see.

b -Type transitions are too weak to be seen in the spectra. In some cases, lines could not be seen in the recorded spectra, because they were overlapped by stronger transitions of synthesis by-products and are thus not depicted in Figure 6.2. A calculated spectrum is shown in the lower trace and has been derived from a least squares fit analysis. The numbers below the calculated spectrum give the J rotational quantum numbers of the c -type transitions. Each line is split by internal rotation into two equally spaced components separated by ~ 4.5 MHz. The upper row J -quantum numbers belong to the asymmetry component $J_{3,J-2} \leftarrow J_{2,J-1}$ while the two lower rows show transitions belonging to the asymmetry component $J_{3,J-3} \leftarrow J_{2,J-1}$. As can be seen from the Fortrat diagram in Figure 6.3, the asymmetry component with

$J_{3,J-3} \leftarrow J_{2,J-1}$ turns from higher to lower frequencies for J up to 23 and then turns back to higher frequencies at higher J values. This behavior can also be seen in Figure 6.2, where the transitions with $J = 29, 30, 31$ follow increasing frequencies.

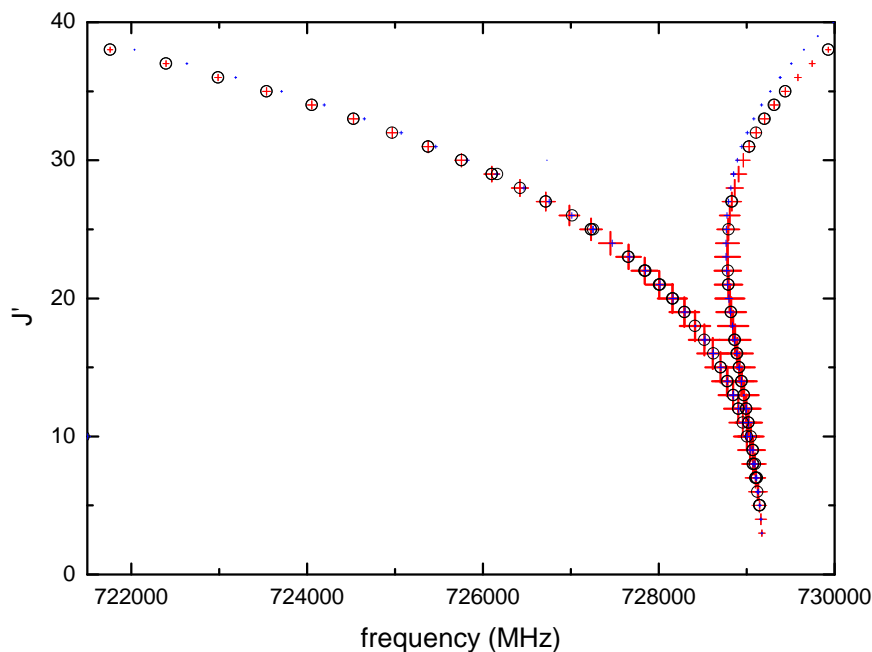


Figure 6.3: Fortrat diagram of the HSOD Q_2 -branch at 729 GHz. With increasing J rotational quantum numbers the lines split into a series of additional components, caused by two effects: (i) the inertial asymmetry splitting (larger splitting) and (ii) the separation into b - and c -type transitions (smaller splitting). Assigned transitions are marked by circles, where the size of the crosses indicates their intensities.

6.3 Molecular Parameters

In total, 118 Q -branch rotational transitions of HSOD were measured. 94 lines have been assigned to c -type and 12 to b -type transitions. Line frequencies could be derived to accuracies between 100 and 300 kHz. The c -type transitions are stronger than the b -types according to the two times stronger dipole moment component in the c -axis direction. From the analysis of the Q -branch transitions, molecular spectroscopic parameters have been obtained which allowed for the prediction of accurate P - and R -branch

transition frequencies. 12 transitions have been assigned within the spectral range of measurements presented here which belong to transitions of the rR_0 - and rR_1 -branch. While Q -branch transitions allow only for determination of the molecular constants $A - (B + C)/2$ and $(B - C)/4$, additional R - or P -branch transitions reveal the constants A , B , and C , separately. Pickett's program package *spfit/spcat* [99] has been used by employing a standard Watson type Hamiltonian in S -reduction (see Section 2.1.2) to fit the data. Due to the high accuracy of the measurements all quartic centrifugal distortion constants D and the sextic constants H_{JK} and H_K as well as h_2 and h_3 were determined. A weak Coriolis interaction of closely related states was found and has been considered by the G Coriolis interaction term. The two components due to tunneling splitting were treated as two separate states and the ΔE gives the energy separation of the two states for $K_a = 0$. The weighted root mean-squares deviation (wrms) of all fitted lines is found to be 0.996, which indicates that all measured transitions can be reproduced to their experimental uncertainties. All constants of the fit are given in Table 6.1. Instead of giving the parameters for the upper and lower torsional state, the average constant and half of the difference between the upper and the lower sub-state is given.

6.4 Conclusion and Discussion

Precise spectroscopic data of HSOD have been obtained. The experimentally derived parameters are in excellent agreement with the theoretically predicted values (see Table 6.1). The line splitting due to the tunneling effect has been measured to be about 4.5 MHz for all c -type transitions of the rQ_2 -band and less than 300 kHz for b -types which corresponds to the Doppler limited resolution of the Cologne Terahertz Spectrometer. Both b - and c -type transitions obey the selection rule $\Delta K_a = \pm 1$ and thus carry information on the tunneling splitting $\delta_{K'_a}$ and $\delta_{K''_a}$ of upper K'_a and lower K''_a state levels. For c -type transitions the two components of line doublets are separated by $\Delta \nu_c = \delta_{K'_a} + \delta_{K''_a}$, whereas the corresponding line splitting of b -type transitions is calculated from $\Delta \nu_b = |\delta_{K'_a} - \delta_{K''_a}|$ (see e.g. [130]). The line splitting $\Delta \nu_{1,0} = \delta_1 + \delta_0$ for all rR_0 c -type transitions was found to be 3.4 MHz, the splitting of rR_1 c -types is $\Delta \nu_{2,1} = \delta_2 + \delta_1 = 2.2$ MHz and for the rQ_2 doublets we found $\Delta \nu_{3,2} = \delta_3 + \delta_2 = 4.5$ MHz. On the other hand none doublets of b -type ${}^rR_{0,1}$ and rQ_2 transitions are resolved and thus the terms $\Delta \nu_b = |\delta_{K'_a} - \delta_{K''_a}|$ are small in all cases, indicating that the δ_{K_a} have to be almost equivalent for all K_a and in the order of 2 MHz, which is in good agreement to the K_a independent value of 3.4 MHz obtained by Quack et al. [102] from *ab initio* calculations.

The ratio of measured line intensities of transitions belonging to c -type and b -type transitions have been used to derive the ratio of the dipole components μ_c/μ_b . For the intensities of b -type transitions it has been taken into

account that the torsional splitting is not resolved and thus *b*-type transitions gain in intensities by overlapping of lines. A ratio of $\mu_c/\mu_b = 2.4(3)$ has been obtained from the measurements, which is in good agreement with the theoretically predicted value of 1.9 ($\mu_c = 1.4908 D, \mu_b = 0.7854 D$).

Table 6.1: Ground state molecular parameters (MHz) of HSOD

Parameter	Theoretical value ^a	Scaled theoretical value ^b	Experimental value
<i>A</i>	159973.5	159903.7	159965.19(45)
$\Delta A/2$			2.375(248)
<i>B</i>	14133.1	14134.9	14132.202(40)
$\Delta B/2$			0.00259(82)
<i>C</i>	14023.5	14021.9	14020.683(41)
$\Delta C/2$			-0.00314(85)
<i>D_J</i> × 10 ³	19.7471	20.7196	20.729(52)
$\Delta D_J/2 \times 10^3$			-0.183(84)
<i>D_{JK}</i> × 10 ³	277.779	292.706	290.639(45)
<i>D_K</i>	3.57255	4.02488	3.289(86)
$\Delta D_K/2$			0.786(74)
<i>d₁</i> × 10 ³	-0.13776	-0.15047	-0.1530(42)
$\Delta d_1/2 \times 10^3$			-0.00219(68)
<i>d₂</i> × 10 ³	0.39006	0.51376	0.509411(93)
$\Delta d_2/2 \times 10^3$			0.000161(85)
<i>H_{JK}</i> × 10 ⁶			-2.378(68)
<i>H_K</i>			-0.1178(109)
<i>h₂</i> × 10 ⁹			-6.66(43)
<i>h₃</i> × 10 ⁹			3.945(235)
ΔE	3.45 ^c		3.36(36)
<i>G_a</i>			0.3567(147)
wrms ^d			0.996
μ_c/μ_b ^d	1.9		2.4(3)

^a *A, B, C*: CCSD(T)/cc-pCVQZ + CCSD(T)/cc-pVTZ vibrational corrections; centrifugal distortion parameters: CCSD(T)/cc-pVTZ; dipole moment: MP2/cc-pVTZ.
^b scaled with the experimental to theoretical ratios taken from HSOH and DSOD in order to improve the predictions.
^c calculated by Quack and Willke [102] (RPH with aug-cc-pVTZ basis set).
^d Dimensionless.

Empirical equilibrium structure of HSOH

Hydrogen peroxide (HOOH), disulfane (HSSH), and oxadisulfane (HSOH) belong to a family of molecules possessing a simple skew-chain geometry. In Figure 7.1 the three kin molecules are depicted, the structural parameters are given in Table 7.3.

The two bond angles as well as the dihedral angle are relatively close to 90° . While HOOH and HSSH have a C_2 symmetry axis oriented perpendicular to the bond of the two heavy atoms and bisecting the dihedral angle, the equilibrium structure of HSOH has no geometrical symmetry at all. The principal axis corresponding to the smallest moment of inertia, the a -axis, is almost identical with the bond between the two heavy atoms in all three cases. Despite their asymmetric structure these molecules are nearly accidental prolate symmetric tops with rotational constants $B \approx C$ corresponding to almost identical momenta of inertia $I_b \approx I_c$.

In 1989 Flaud *et al.* [41] reported for the first time a r_0 structure of HOOH, two years later Behrend *et al.* [11] have determined an experimentally “partial equilibrium” structure of HSSH. To derive this “partial equilibrium” structure they have taken the rotational vibrational contributions of the torsional motion into account and removed them.

In course of this thesis, for the first time an empirical equilibrium structure of oxadisulfane has been derived. Oxadisulfane is the simplest molecule that possesses a classical S-O single bond. The S-O bond in molecules such as HSO, SO, or SO₂ is known to exhibit multibond character with a bond length of approximately 1.45 Å, whereas classical S-O single bonds have lengths around 1.66 Å. Hence, HSOH is a testbed for high level *ab initio* calculations of S-O single bond molecules and of geometrical structure calculations in general¹.

¹see e.g. [1, 2, 3, 79, 85, 112, 123]

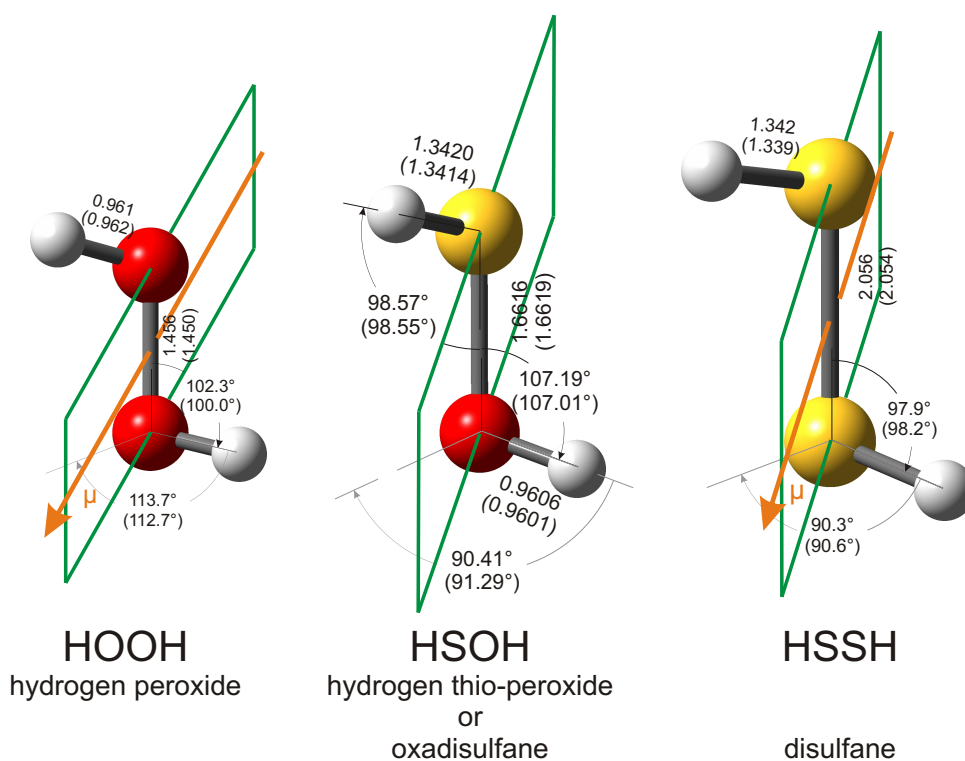


Figure 7.1: Comparison between the experimental (for HOOH and HSSH see [41, 11]) and theoretical (in parentheses; CCSD(T)/cc-pCVQZ [123]) geometrical structures of the three kin molecules HOOH, HSOH, and HSSH. Bond lengths are given in Å. Planes shown bisect torsional angles. For HOOH and HSSH, the dipole moment μ lies in the plane.

7.1 Geometrical parameters of HSOH

An accurate theoretical structure of HSOH has been obtained from CCSD(T)/cc-pCVQZ *ab initio* calculations [123]. All structural parameters are given in Table 7.1. To derive an empirical equilibrium structure of HSOH the

Table 7.1: Geometrical parameters (distances in Å, angles in degrees) for HSOH

Geometrical parameter	CCSD(T)/ cc-pCVQZ [123]	empirical r_e^{emp} [this work]
$R(\text{SO})$	1.6619	1.6616(1)
$R(\text{SH})$	1.3414	1.3420(2)
$R(\text{OH})$	0.9601	0.9606(3)
$\alpha(\text{OSH})$	98.55	98.57(5)
$\alpha(\text{SOH})$	107.01	107.19(3)
$\tau(\text{HSOH})$	91.29	90.41(11)

rotational constants A_0, B_0 , and C_0 of HSOD (see Chapter 6) together with rotational constants of HSOH, H^{34}SOH (see Section 9.1), and DSOD [9] have been used. Empirical equilibrium constants A_e^{emp}, B_e^{emp} , and C_e^{emp} according to equations (2.97)-(2.99) have been derived for these isotopologues using vibration-rotation correction terms obtained from CCSD(T)/cc-pVTZ calculations of the harmonic and anharmonic force fields (see Table 7.2).

The three bond lengths $R(\text{OH})$, $R(\text{SH})$ and $R(\text{SO})$ as well as the bond angles $\alpha(\text{OSH})$, $\alpha(\text{SOH})$, and the dihedral angle $\tau(\text{HSOH})$ were fitted to the empirical equilibrium constants of the four isotopologues using a least-squares fit analysis by Pawlowski *et al.* [94]. All results of the fit are shown in Table 7.1.

7.2 Conclusion and Discussion

The data obtained in course of this work on HSOD, HSOH, and H^{34}SOH have been used together with previously published experimental results on DSOD to derive for the first time structural parameters of HSOH in an empirical approach. The agreement between experimentally and theoretically obtained values is excellent and emphasizes the high quality of the *ab initio* calculations. On the other hand it shows the superb quality of the high resolution data recorded in course of this work with the Cologne Terahertz Spectrometer.

The structure of HSOH fits smoothly into those of its kin molecules HSSH and HOOH (see Table 7.3 and Figure 7.1).

Table 7.2: Rotational constants and vibrational corrections (MHz) for HSOH and its isotopologues

Parameter	experimental value v=0	$\frac{1}{2} \sum_r \alpha_r^a$ (CCSD(T)/cc-pVTZ)
HSOH [this work] ^b		
<i>A</i>	202069.04428(118)	1431.9
<i>B</i>	15281.956038(115)	118.7
<i>C</i>	14840.215621(114)	136.3
H ³⁴ SOH [this work] ^b		
<i>A</i>	201739.7540(172)	1431.1
<i>B</i>	15001.43809(64)	116.0
<i>C</i>	14573.77801(58)	133.1
DSOD [19]		
<i>A</i>	106850.4937(55)	513.9
<i>B</i>	13865.38319(173)	89.1
<i>C</i>	13173.54491(227)	106.8
HSOD [this work] ^c		
<i>A</i>	159965.20(44)	946.2
<i>B</i>	14132.204(40)	107.5
<i>C</i>	14020.685(41)	111.6

^a α_r are the vibration rotation interaction constants for all normal modes *r*.
^b see Section 9.1.
^c see Chapter 6.

Table 7.3: Geometrical parameters (distances in Å, angles in degrees) for HOOH, HSOH, and HSSH

Geometrical Parameter	HOOH Flaud <i>et al.</i> [41]	HSOH [this work]	HSSH Behrend <i>et al.</i> [11]
<i>R</i> (<i>XX</i>)	1.456	1.6616(1)	2.056
<i>R</i> (<i>SH</i>)	---	1.3420(2)	1.342
<i>R</i> (<i>OH</i>)	0.961	0.9606(3)	---
α (<i>XSH</i>)	---	98.57(5)	97.9
α (<i>XOH</i>)	102.3	107.19(3)	---
τ (<i>HXXH</i>)	113.7	90.41(11)	90.3

X=S, O

For HSOH, the corresponding *a* principle axis almost coincides with the S-O bond, while the S-H bond lies in the plane spanned of the *a*- and *b*-principle axis and the O-H bond in the plane spanned of the *a*- and *c*-principal axis. Figure 7.2 shows the equilibrium structure and the direction of the three principal axes of HSOH.

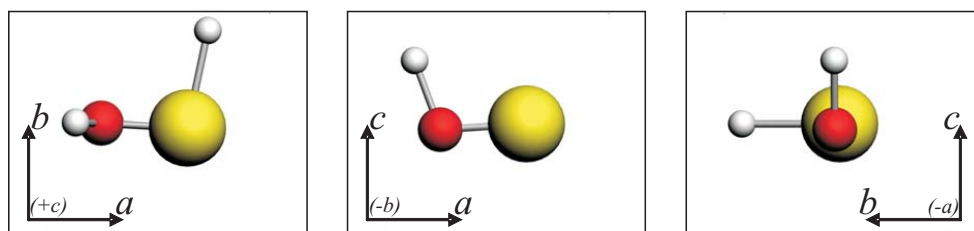


Figure 7.2: Equilibrium configuration and direction of the three principal axes of HSOH.

In Sections 8.1 and 8.2 the first high resolution infrared measurements on HSOH are presented. The measurements of vibrationally excited states of HSOH and its isotopologues yield experimental values on the vibration-rotation interaction constants α_r and hence, the in this section used theoretical α_r are compared to the derived experimental values available.

High Resolution Infrared Measurements on HSOH

In this chapter the first high resolution infrared measurements on HSOH are analyzed. The dynamics in HSOH itself are of great interest because of its large amplitude motion (see also Section 9.2), the torsional mode $\tau(\text{HSOH})$. Also -as mentioned in Section 2.4- the calculation of molecular structure is somewhat involved due to the fact that vibrational effects have to be taken into account. Consequently not only the pure rotation of a certain species has to be studied but also its vibrational spectra.

Guided by high level *ab initio* calculations [8, 10] and Matrix measurements by Smardzewski and Lin [105] and also Beckers *et al.* [8] (see Table 8.1) spectra in the range between $380\text{--}1400\text{ cm}^{-1}$ and $1850\text{--}3800\text{ cm}^{-1}$ have been recorded by employing a high resolution Fourier Transform spectrometer (Bruker IFS 120 HR at University of Wuppertal)¹.

Since the most efficient synthesis of HSOH is the pyrolysis of di-*tert*-butyl sulfoxide (see Chapter 5) this method was employed during the measurements in the IR-region. The collected data are mapped in Figure 8.1. As described in Chapter 5 the pyrolysis is supposed to be a promising simple thermal decomposition of *tert*-butylsulfenic acid to produce HSOH and H₂O simultaneously along with 2-methylpropene by competing unimolecular routes. In contrast to this, the IR-spectra (see Figure 8.1) of the gaseous pyrolysis products revealed a much more complex thermal behavior of *tert*-butylsulfenic acid.

The analysis of the IR spectra of the pyrolysis products obtained at 1150°C shows, that main products of the low-pressure pyrolysis of *tert*-butylsulfenic acid are in fact H₂O, S₂O, SO₂, and 2-methylpropene. In addition to those, traces of several hydrocarbons, produced by thermal decomposition of 2-methylpropene (CH₄, 1,2-propadiene (C₃H₄), propyne (C₃H₄), and ethyne (C₂H₂)) were also identified in the final gaseous pyrolysis products via comparison to reference spectra. A detailed discussion about the pyrolysis prod-

¹More details on the introduced experimental setup are given in Section 4.3.

Table 8.1: Calculated and experimental Matrix vibrational modes (cm^{-1}) (relative intensities in parentheses)

vibrational mode	theoretical value ^a [8, 10]	Ar-Matrix [8]	Ar-Matrix [105]
$\nu(\text{OH})$	3657.2 (92)	3608.3 (43)	3606.0 ^b (26)
$\nu(\text{SH})$	2536.9 (22)	2550.1 (8)	
$\delta(\text{SOH})$	1188.1 (54)	1175.7 (53)	1177 (56)
$\delta(\text{OSH})$	1004.6 (3)		
$\nu(\text{SO})$	756.7 (66)	762.5 (100)	763 (100)
$\tau(\text{HSOH})$	451.7 (100)	445.3 (54)	444.8 (44)

^a CCSD(T)/cc-pVQZ + CCSD(T)/cc-pVTZ anharmonic correction
^b Band was attributed to HOOH in reference [105] and has been reassigned by Beckers *et al.* to the O–H stretch of HSOH [8].

ucts is given by Beckers *et al.* [8].

Due to a comparatively large amount of supplementary pyrolysis products formed at 1150°C as well as the nevertheless low abundance of transient HSOH in the gaseous pyrolysis products, the assignment of spectral features from HSOH in the 400 to 1400 cm^{-1} region proved to be difficult. At least the four fundamental bands of HSOH expected in this spectral region (see Table 8.1) were found to interfere strongly with bands of several supplementary pyrolysis products (i.e. S_2O and accompanying hydrocarbons) or are by far too weak in intensity and thus have not been assigned.

In the spectral range from 1800 to 3850 cm^{-1} the two fundamental stretching modes $\nu(\text{SH})$ and $\nu(\text{OH})$ are expected to occur. Even though the $\nu(\text{OH})$ is located where strong transitions of gaseous water appear the band has been assigned. A detailed analysis of this band is given in Section 8.1. The $\nu(\text{SH})$ has also been assigned and is located at approximately 2538 cm^{-1} which is slightly above the $(\nu_1 + \nu_3)$ combination band of the by-product SO_2 . More details on this fundamental vibrational motion are given in Section 8.2.

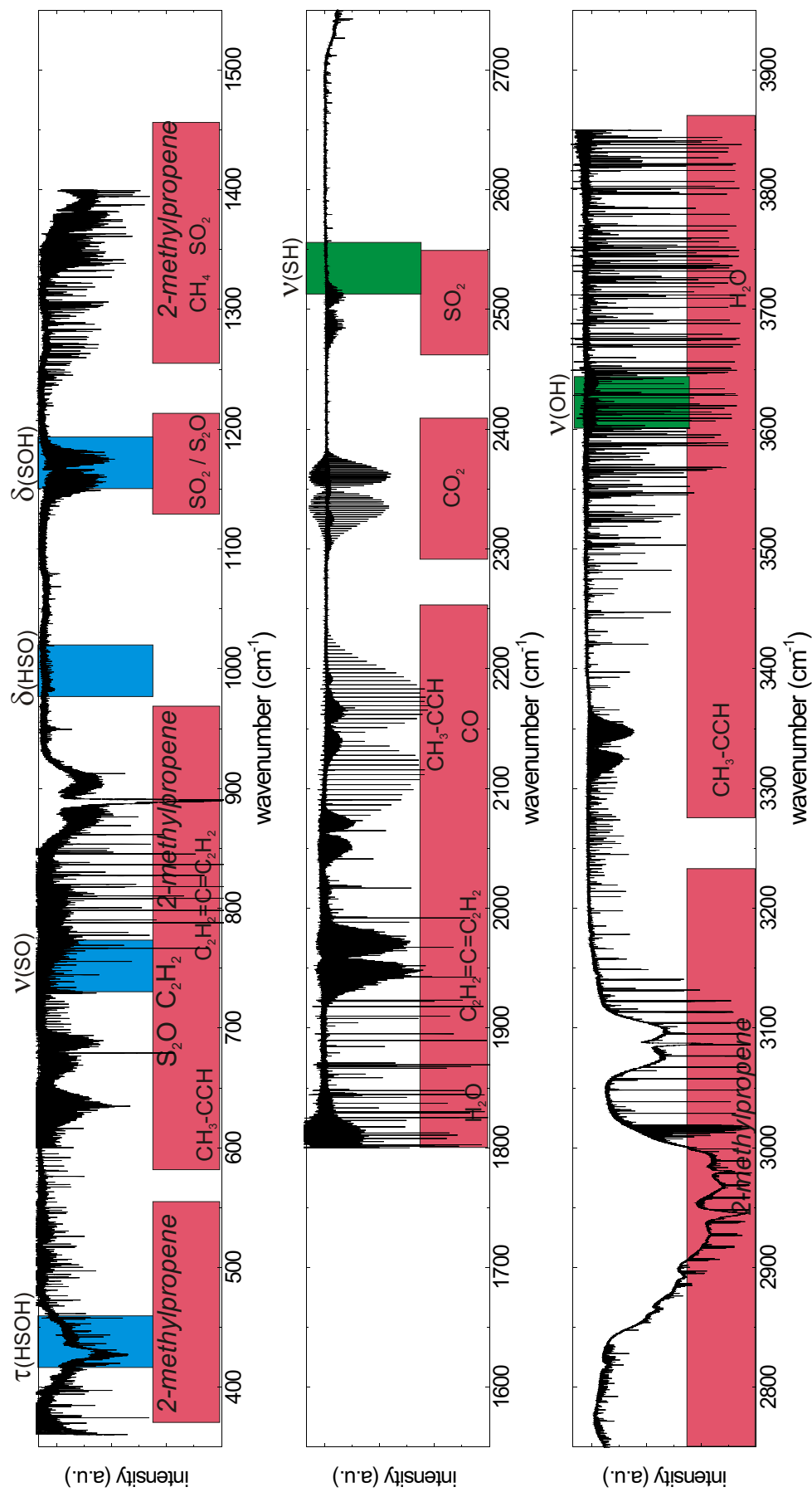


Figure 8.1: Gas-phase IR-spectra of the pyrolysis products di-*tert*-butyl sulfoxide obtained at 1150°C. Predicted positions of the fundamental vibrational modes of HSOH are marked in blue and green, respectively. Assigned vibrational bands of supplementary pyrolysis products are flagged in red.

8.1 Fundamental OH-stretching mode of HSOH

According to the geometry (see Chapter 7 Figure 7.2) of HSOH, with the OH-bond located in the a - c -plane of the principal axis-system, an a -type parallel and a c -type perpendicular spectrum but no b -type spectrum is expected when the fundamental OH-stretching mode is excited.

In Figure 8.2 the band center region of the recorded spectrum is plotted. It clearly shows the characteristic pattern of a parallel type spectrum with strong unresolved qQ -branches at the band center and a series of overlapping pP - and qR -branches. Furthermore two resolved strong Q -branches, peaked

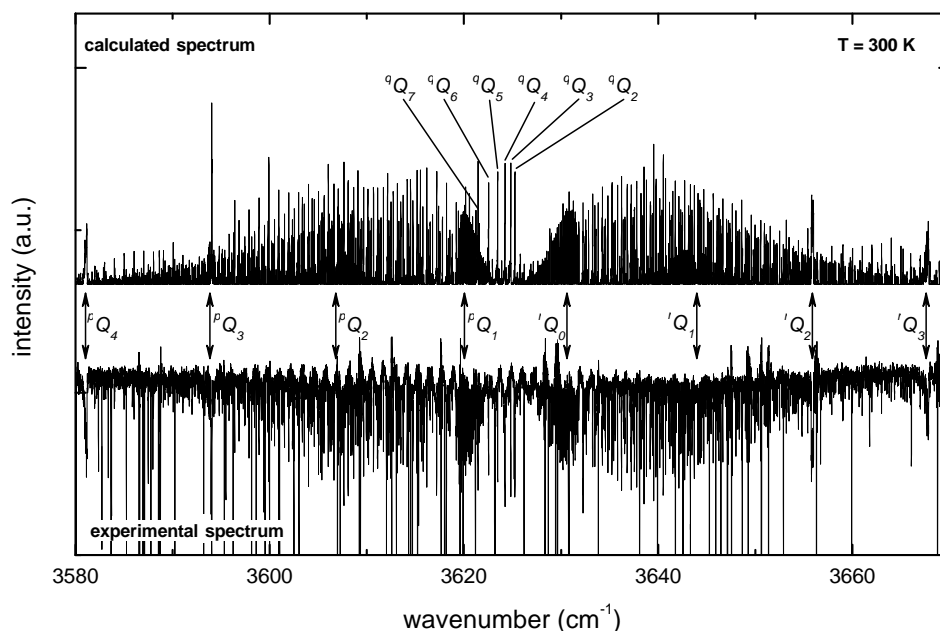


Figure 8.2: Measured and calculated spectrum of HSOH at the $\nu(\text{OH})$ band center region. The calculated spectrum at 300 K is based on molecular constants from the final data analysis. The pQ_4 - to rQ_3 -branches of the c -type band and the qQ_2 - to qQ_7 -branches of the a -type band are indicated. The strong absorption lines in the experimental spectrum are mainly due to the H_2O by-product.

towards the band center at 3625.6 cm^{-1} , are most prominent and were consequently assigned to the pQ_1 - and rQ_0 -branches of a perpendicular type band. Figure 8.3 shows the calculated spectra of the parallel and perpendicular bands in the band center region based on the molecular constants derived in the final data analysis. For comparison the lower trace of Figure 8.3 displays the recorded HSOH spectrum. It turned out, that the strongest lines in the recorded spectra are due to impurities of the sample (see transitions marked with an asterisk). The *in situ* production of the sample HSOH from its precur-

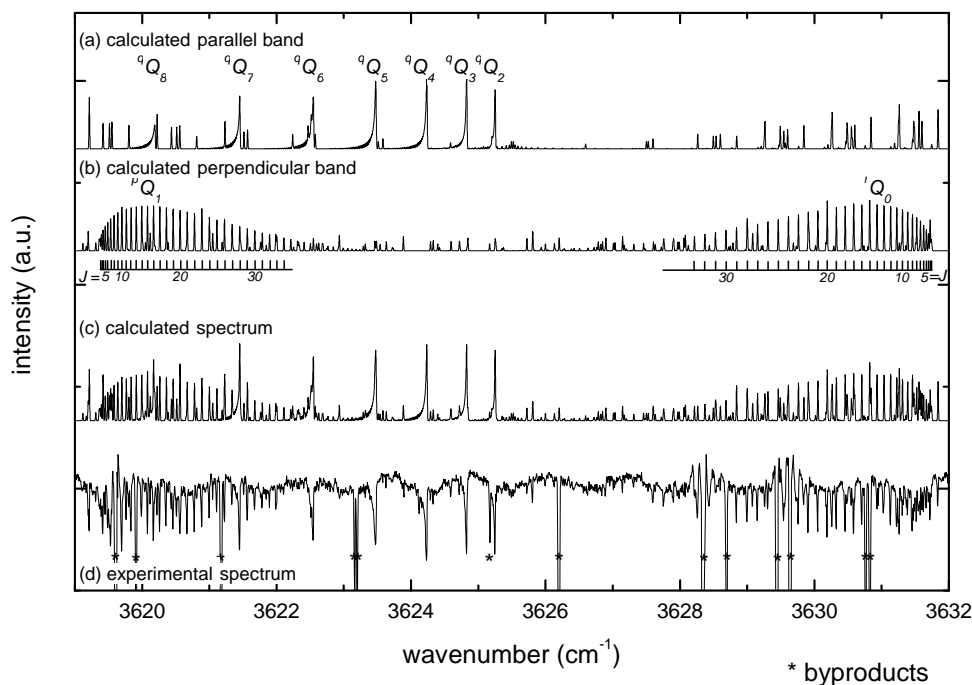


Figure 8.3: Band center region of the $\nu(\text{OH})$ stretching mode: (a) Calculated spectrum of the parallel band, (b) perpendicular band, and (c) superposition of both spectra using molecular constants from the final data analysis. The parallel band spectrum shows the qQ_2 - to qQ_8 -branches. The pQ_1 - and rQ_0 -branches form the dominant structure in the perpendicular band. (d) Experimental spectrum, spectral features of by-products are indicated with an asterisk.

sor is accompanied by several by-products, such as water, 2-methylpropene, and sulfur dioxide. The strongest transitions in the recorded range between 3500 and 3800 cm^{-1} belong to the H_2O molecule and had to be identified before further data treatment.

8.1.1 The a -type parallel band

For the parallel band of the $\nu(\text{OH})$ stretching fundamental vibrational mode ($\nu = 1 \leftarrow 0$) only transitions with $\Delta K_a = 0$ occur. Attending a particular K_a a sub-band with P -, Q -, and R -branches is obtained. The distances of succeeding lines in the P - and R -branches are according to a rigid rotor of order $B + C = 1 \text{ cm}^{-1}$. The complete parallel band is gained by superposition of a number of such sub-bands (if the interaction between vibration and rotation could be neglected all the sub-bands would coincide exactly). In Figure 8.4 the calculated sub-bands up to $K_a = 4$ and the superposition up to $K_a = 10$ are shown. Due to the internal asymmetry of this molecule there is some

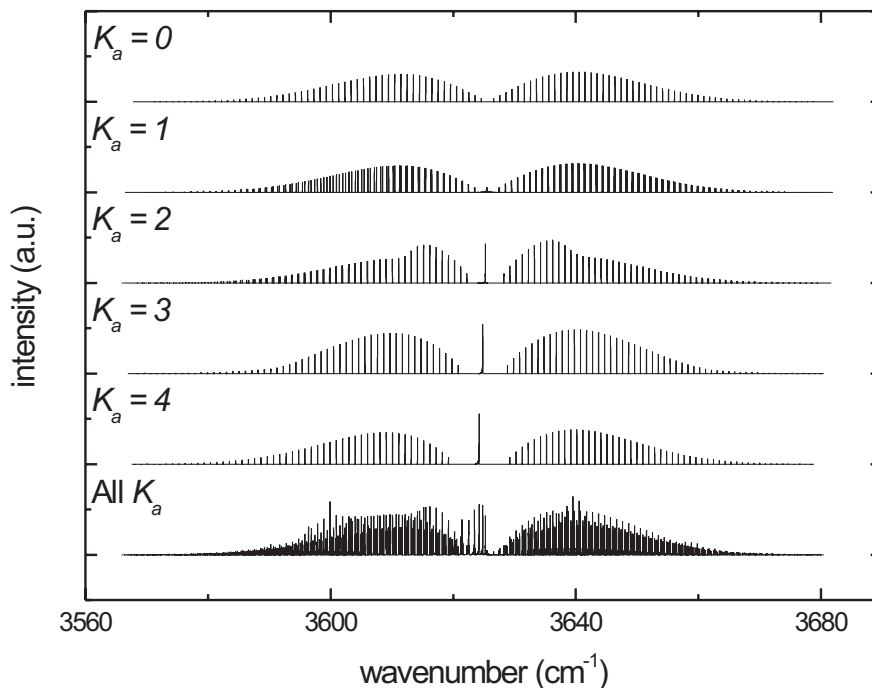


Figure 8.4: Sub-bands of the parallel band up to $K_a = 4$ and "complete2 parallel band of the OH-stretching vibration from HSOH (Temperature $T = 300\text{K}$). The "complete" parallel band is a superposition of all sub-bands up to $K_a = 10$. The "bump" in the $K_a = 2$ sub-band is due to the superposition of unresolved lines from the asymmetry components.

distortion of the branches. Every branch splits into two sub-branches for K_a different from zero according to the K_c value. Most pronounced is the splitting of the lines in the branches with $K_a = 1$. In the $K_a = 2$ sub-band the asymmetry splitting is not resolved for small J values and therefore a "bump" (see Figure 8.4) arises where these components are superimposed.

As mentioned before HSOH is only slightly asymmetric close to the limiting case of a symmetric prolate top; Figure 8.5 gives a graphical representation of the variation of the energy levels from the limiting case of a rigid symmetric prolate top. In the graph the quantum numbers $m = J + 1$ for *R*-branch transitions, and $m = -J$ for *P*-branch transitions are plotted over the deviation

$$\Delta v = (v_0 + (\tilde{B}' + \tilde{B}'')m + (\tilde{B}' - \tilde{B}'')m^2) - v_{exp} \quad (8.1)$$

with $\tilde{B} = \frac{1}{2}(B + C)$. It can be seen that the asymmetry splitting increases with increasing J but by far less rapidly for the higher K_a values and is not resolved for any $K_a \geq 4$. Also the deviation from the rigid rotor approximation can be seen for increasing J .

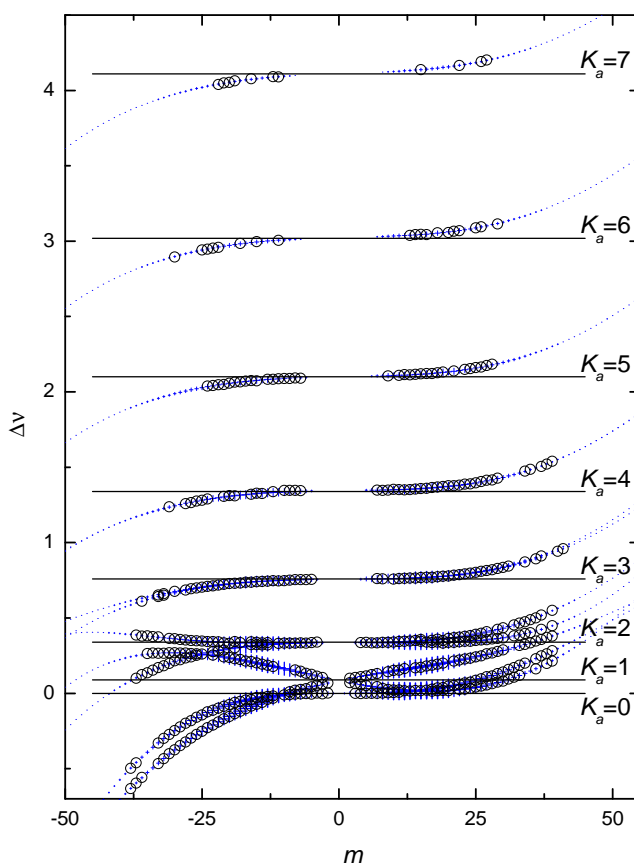


Figure 8.5: Rotational energy (in the $v_{OH} = 1$ state) of the slightly asymmetric top molecule HSOH as a function of m . For *R*-branch transitions the quantum number $m = J + 1$ and for *P*-branch transitions $m = -J$ is used. Assigned transitions are marked by circles, where the size of the crosses indicates their intensities. The deviation of the curves from the horizontal lines represents the deviation from the levels of a rigid symmetric top.

8.1.2 The c -type perpendicular band

A perpendicular band with $\Delta K_a = \pm 1$ consists, like a parallel band, of a number of sub-bands. But even if the interaction between vibration and rotation could be neglected the sub-bands do not coincide. The spacing of adjacent Q -branches of a perpendicular band is of order $(2A'' - B'' - C'')$ which is 12.47 cm^{-1} , taking into account the highly accurate HSOH ground state rotational constants (see Table 9.1). For K_a different from zero there are two sets of sub-bands, one with $\Delta K_a = +1$ and one with $\Delta K_a = -1$. In Figure 8.6 simulated sub-bands up to $K_a = 3$ and the superposition (up to $K_a = 10$) are shown.

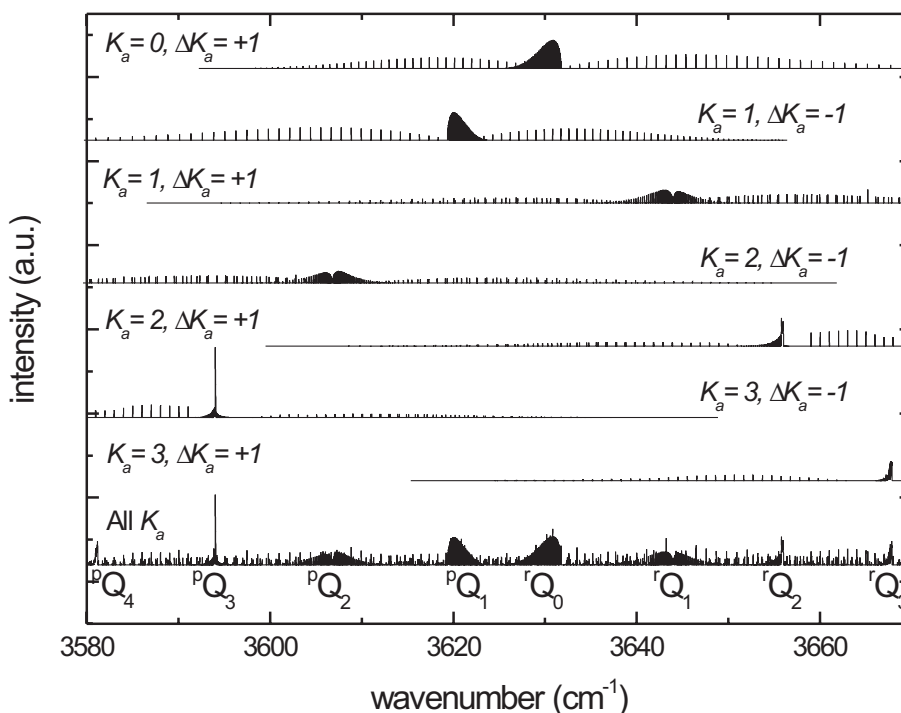


Figure 8.6: Sub-bands of the perpendicular band up to $K_a = 3$ and “complete” perpendicular band of the OH-stretching vibration from HSOH. The “complete” perpendicular band is a superposition of all sub-bands up to $K_a = 10$.

Due to the internal asymmetry of this molecule there is a small distortion of the $^{P,R}Q_{K_a}$ -branches. The $^RQ_{K_a}$ -branches split into two sub-branches for K_a different from zero, and the $^PQ_{K_a}$ -branches for K_a exceed zero, according to the K_c values. These splitting into the sub-branches is most pronounced in the PQ_2 - and the RQ_1 -branches.

A broad overview on the pattern of P -, R -, and Q -branches of the perpendicular spectrum is best obtained with a Fortrat diagram, shown in Figure 8.7. In

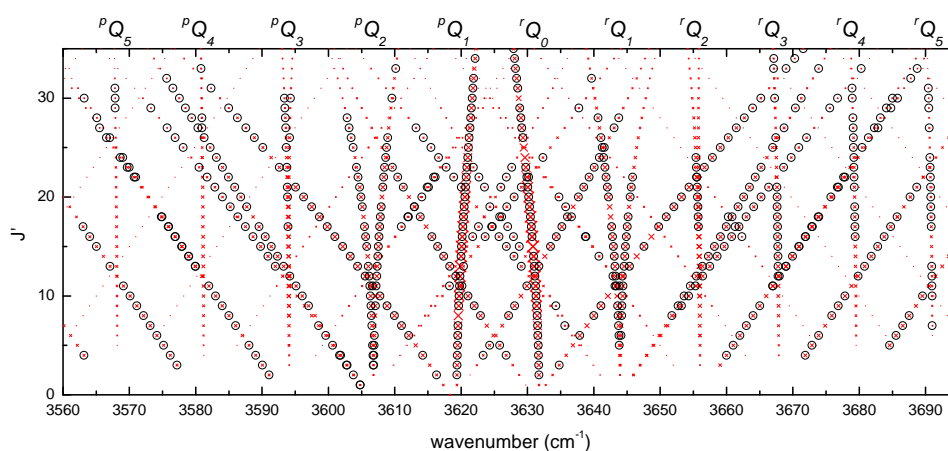


Figure 8.7: Fortrat diagram of the $\nu(\text{OH})$ perpendicular band up to $K''_a = 5$. Assigned transitions are marked by circles, where the size of the crosses indicates their intensities.

this diagram the arrangement in groups of individually measured transitions into branches and sub-branches stands out. Assigned transitions are marked with circles, and the line intensities are indicated by the size of the crosses. The branches are only slightly affected by centrifugal distortion, indicating HSOH to be a rather rigid molecule in its vibrational excited OH-stretching mode.

8.1.3 Molecular Parameters

All of the more than 1300 identified a - and c -type transitions were simultaneously fitted in a least-squares analysis to molecular parameters of a Watson type Hamiltonian in S -reduction (see Section 2.1.2). Transitions up to $J'' = 35$ and $K''_a = 7$ have been included in the final fit using Pickett's program *spfit* [99]. The ground state molecular constants were fixed to the highly accurate values from the measurements presented in Section 9.1 (see Table 9.1). The analysis yields a precise value for the band center frequency of the $\nu(\text{OH})$ stretching mode, its rotational constants A , B , and C as well as all quartic centrifugal distortion constants D_J , D_K , and D_{JK} . Except H_J , the sextic terms and higher order constants were not significant and thus have been fixed to their corresponding ground state values. In addition the asymmetry parameters d_1 and d_2 have been derived. All molecular constants and for comparison high level *ab initio* values [8, 44] are given in Table 8.2. The dimensionless weighted root-mean-square deviation value of 1.13 shows the excellent agreement of the experimental data with the semirigid rotor model.

Table 8.2: Spectroscopic parameters for the $\nu(\text{OH})$ first excited state of HSOH.

Parameter		theoretical ^a [8, 44]	experimental ^b [this work]
		$\nu_{\text{OH}} = 1$ state	$\nu_{\text{OH}} = 1$ state
A	MHz	199769.9	199532.61(74)
B	MHz	15255.6	15259.981(49)
C	MHz	14829.6	14833.182(51)
$D_J \times 10^{-3}$	MHz		24.870(65)
D_{JK}	MHz		0.38594(97)
D_K	MHz		5.8793(154)
d_1	MHz		-0.7053(156)
$d_2 \times 10^{-3}$	MHz		0.3080(156)
$H_J \times 10^{-6}$	MHz		0.0772(301)
$H_{JK} \times 10^{-6}$	MHz		-1.1950 ^c
$H_{KJ} \times 10^{-3}$	MHz		0.02987 ^c
$H_K \times 10^{-3}$	MHz		0.6042 ^c
$h_1 \times 10^{-9}$	MHz		1.0178 ^c
$h_2 \times 10^{-9}$	MHz		-1.5560 ^c
$h_3 \times 10^{-9}$	MHz		-0.9528 ^c
ν_{OH}	cm^{-1}	3657.2	3625.59260(20)
α_{OH}^A	MHz	2365.9	2536.44(74)
α_{OH}^B	MHz	23.3	21.975(49)
α_{OH}^C	MHz	10.8	7.034(51)

^a CCSD(T)/cc-pVQZ + CCSD(T)/cc-pVTZ vibrational correction
^b In the analysis values for the $\nu = 0$ state were fixed to data taken from Section 9.1 (see Table 9.1).
^c Values are fixed to constants of the vibrational ground state.

8.1.4 Conclusion and Discussion

The fundamental $\nu(\text{OH})$ stretching mode displays a clear cut *a*-type parallel and *c*-type perpendicular spectrum. In Figure 8.8 the calculated parallel band and perpendicular band is shown, also the superposition of these two bands and the measured spectrum is mapped.

The analysis of this band proves HSOH to be a fairly rigid molecule in the first excited $\nu(\text{OH})$ -state. The B and C rotational constants in the fundamental OH-stretching mode are less than 0.15% smaller than the ground state values. The same holds true for the centrifugal constants. The A rotational constants in the excited state changes by 1%.

For non of the vibrational excited states an experimental value of the splitting has been determined, but by Quack *et al.* [102] a value of 0.002177 cm^{-1} for the $\nu(\text{OH})$ state has been calculated. The instrumental resolution of the presented data is 0.011 cm^{-1} and the calculated Doppler line width in the vibrational excited $\nu(\text{OH})$ state is $\nu_{\text{Doppler}}(\text{FWHM}) = 0.0063 \text{ cm}^{-1}$. Accordingly, the tunneling splitting is not resolved in the recorded spectra.

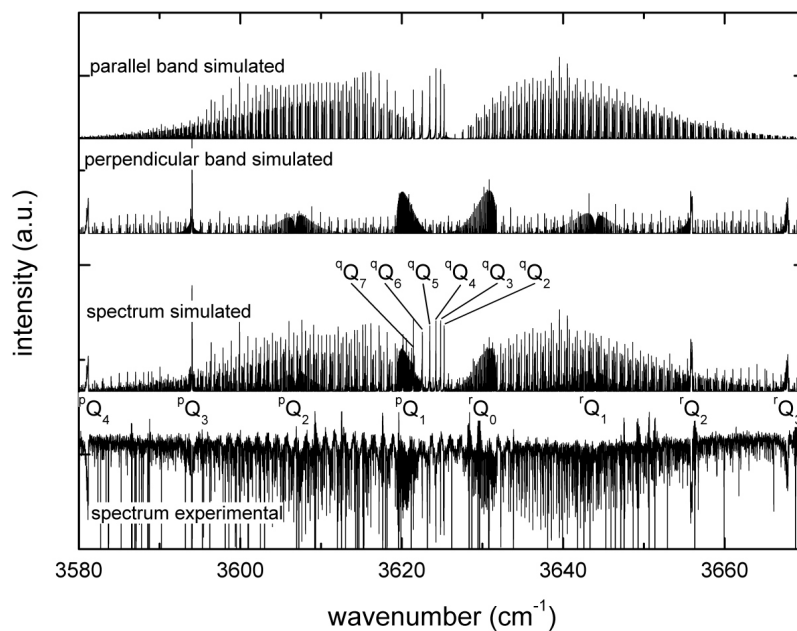


Figure 8.8: Calculated parallel band, perpendicular band, and spectrum of the fundamental OH-stretching mode of HSOH. The calculated parallel band and perpendicular band of the spectrum are directly superimposed in the complete simulated spectrum.

8.2 Fundamental SH-stretching mode of HSOH

The fundamental $\nu(\text{SH})$ stretching mode ($\nu_{\text{SH}} = 1$ state) is located at approximately 2538 cm^{-1} which is slightly above the $(\nu_1 + \nu_3)$ combination band of SO_2 , centered at 2500.0 cm^{-1} [100]. Since SO_2 is a pyrolysis by-product (see reference [8]), most of the low-wavenumber wing is buried under the combination band, as can be seen in Figure 8.9.

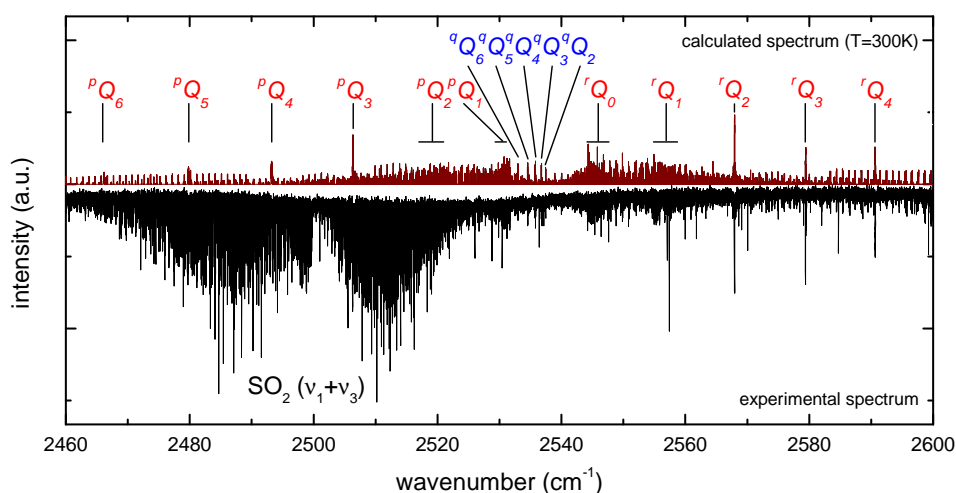


Figure 8.9: Experimental and calculated spectrum of the $\nu(\text{SH})$ fundamental vibrational mode of HSOH. The calculated spectrum at 300 K is based on molecular constants from the final data analysis. The pQ_6 - to rQ_4 -branches of the b -type band and the qQ_2 - to qQ_6 -branches of the a -type band are indicated. The strong band occurring at 2500.0 cm^{-1} belongs to the $(\nu_1 + \nu_3)$ combination band of the by-product SO_2 .

The $\nu(\text{SH})$ band is found to be five times weaker in intensity than the corresponding $\nu(\text{OH})$ band (see Section 8.1), which is in good agreement with previous matrix measurements and *ab initio* calculations by Beckers *et al.* [8] expecting the $\nu(\text{SH})$ band to be 4–5 times less intense than the fundamental OH-stretch (see Table 8.1).

In Figure 7.2 the geometry of HSOH is depicted. The SH-bond is found to lie in the plane stretched by the a - and b -principal axes of the molecule. Hence, the spectrum of the $\nu(\text{SH})$ fundamental vibrational mode is expected to display a clear-cut parallel a -type and perpendicular b -type spectrum with almost same intensities. In Figure 8.9 the dominating ${}^rQ_{K_a''}$ -branches from the perpendicular band are easily recognizable. Furthermore the ${}^qQ_{K_a''}$ -branches from the parallel band -occurring at the band center- are marked. A detailed analysis of occurring sub-bands in parallel- and perpendicular-type spectra

has been given in this thesis exemplarily for the case of the $\nu(\text{OH})$ fundamental vibrational mode (see Sections 8.1.1 & 8.1.2).

Figure 8.10 shows a close-up view on the ${}^P Q_1$ -branch region of the SH-stretch. It is clearly to see that, in contrast to the OH-stretching mode, each

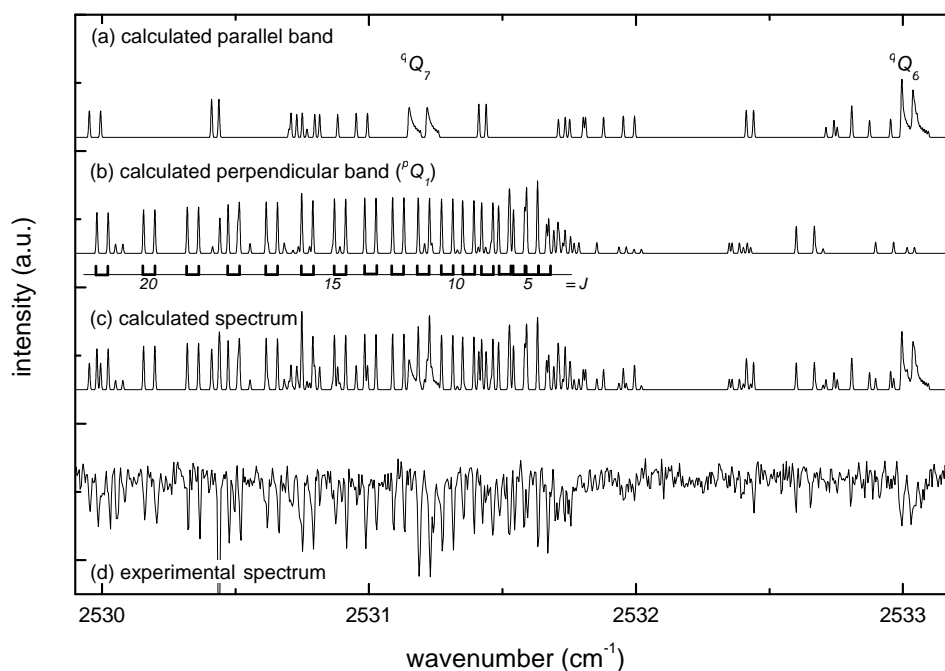


Figure 8.10: Band center region of the $\nu(\text{SH})$ stretching mode: (a) Calculated spectrum of the parallel band, (b) perpendicular band, and (c) superposition of both spectra using molecular constants from the final data analysis. The parallel band shows the ${}^Q Q_6$ - and ${}^Q Q_7$ -branches and the ${}^P Q_1$ -branch from the perpendicular band. (d) Experimental spectrum.

transition in the $\nu(\text{SH})$ -band is split into a doublet. The splitting of the transitions is of order 0.04 cm^{-1} . This value is by a factor of 20 larger than the value of $\approx 0.002 \text{ cm}^{-1}$ estimated by Quack and Willeke [102] for the torsional splittings of the energy levels in the $\nu_{\text{SH}} = 1$ state. A discussion on the splitting of the transitions is given in the next Section 8.2.1. In Section 8.2.2 the procedure of data analysis and the derived molecular constants of HSOH in the first excited $\nu(\text{SH})$ mode are presented.

8.2.1 The torsional splitting in the first excited SH stretching state of HSOH

The chain structure of HSOH is such that the equilibrium torsional (dihedral) angle $\tau(\text{HSOH})$ equals 90.41° (see Chapter 7), which is near the gauche configuration ($\tau = 90^\circ$). Potential barriers of 2216 cm^{-1} and 1579 cm^{-1} exist for the *cis* ($\tau = 0^\circ$) and *trans* ($\tau = 180^\circ$) configurations², respectively. These barriers are sufficiently large that the tunnel effect results in a small splitting of lower torsional energy levels, which lead in turn to the observed doublet structure of the rotational transitions of HSOH and its isotopologues (see Chapters 6 & 9).

In case of the main isotopologue of HSOH, Winnewisser *et al.* [123] reported a splitting of the energy levels in the torsional ground state ($v_t = 0, J = 0, K_a = 0$) of 64.5 MHz. In course of this work, the energy level splitting in the torsional ground state of the isotopologue HSOD has been found to be 3.36 MHz. Both values agree very well with the by Quack and Willeke [102] theoretically derived quantities of $2.34 \times 10^{-3} \text{ cm}^{-1}$ (=72.8 MHz) and $0.115 \times 10^{-3} \text{ cm}^{-1}$ (=3.45 MHz), respectively.

The spectrum of the first excited $\nu(\text{SH})$ state ($v_{SH} = 1$) shows a splitting of the transitions of approximately 0.04 cm^{-1} , which is by far larger than the splitting of 0.00215 cm^{-1} (=64.5 MHz) for the ground state, although smaller than the by Quack and Willeke theoretically derived value of 0.147 cm^{-1} for the first torsionally excited state. Quack and Willeke [102] also predicted a value of $\approx 0.0017 \text{ cm}^{-1}$ for splittings in the $v_{SH} = 1$ state which is of same order as the value for the vibrational ground state and by a factor of 20 smaller than the experimentally observed one.

The large enhancement in size of the $v_{SH} = 1$ torsional splitting is most probably caused by coupling between the first SH stretching state and the manifold of excited torsional states (or combination bands with at least one quanta in the torsional mode) which possess torsional splittings $\gg 0.04 \text{ cm}^{-1}$.

Figure 8.11 shows the observed deviation of split transitions from an averaged line center position in the $v_{SH} = 1$ state as a function of J' for different K'_a levels. The observed torsional splittings are only weakly affected by the rotational quantum number J which rules out the possibility of a Coriolis-type coupling between the $v_{SH} = 1$ state and some other dark-state. The alternatives remaining are a potential or Fermi-type coupling between the $v_{SH} = 1$ and excited torsional states (or combination bands with at least one quanta in the torsional mode).

The effect of potential coupling has already been observed in case of the brethren molecule HSSH [57]. Experimental evidence for a strong coupling of the torsional mode to the SS-stretching mode in the HSSH molecule came from pure rotational spectra of the first excited SS-stretching state [121]. The spectrum of the SS-stretching state shows torsional splittings of the transitions of order 1 MHz, which is almost one order of magnitude larger

²Values are taken from *ab initio* calculations at the CCSD(T)/cc-pCVQZ level of theory, see reference [123].

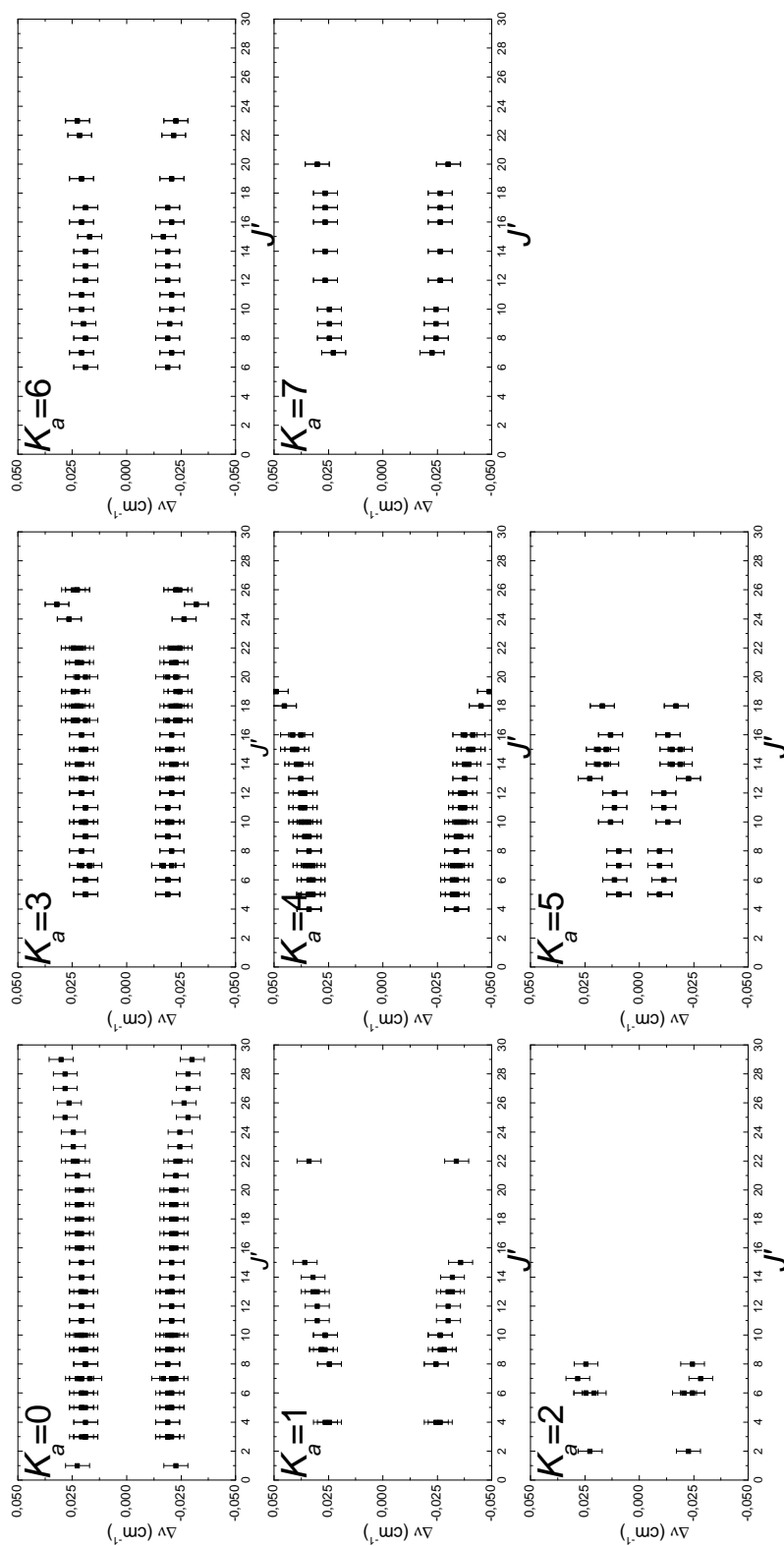


Figure 8.11: Observed torsional splittings of transitions in the $\nu_{\text{SFH}} = 1$ -state. The deviation of the split transitions to an averaged line center positions is plotted versus the rotational quantum number J' for the observed $K'_a = 0, 1, \dots, 7$ values.

than the value of 0.12 MHz theoretically predicted by Gottselig *et al.* [49]. This value is of same order as the value for the splitting of transitions in the vibrational ground state of 0.15 MHz [121]. Based on an *ab initio* potential surface Herbst *et al.* [57] calculated coupling matrix elements and they were able to show that the enhanced splitting in the first excited SS-stretching mode of HSSH is mainly due to a potential coupling between this state and the second torsionally excited state. Guarnieri *et al.* observed an analog splitting in the rotational spectrum of an excited non torsional low frequency vibrational state in the molecule CH₃SCl [57].

In HSOH the $\nu_{SH} = 1$ state is located at approximately 2538 cm⁻¹. This is higher in energy than the *cis*-barrier and in the order of the *trans*-barrier. Hence, an *ab initio* determination of mode coupling -as carried out by Herbst *et al.* in case of HSSH- is involved due to the need of a highly accurate potential energy surface (PES). At the time no PES with the required accuracy is available, but the results presented here triggered a collaboration with the theoreticians Yurchenko *et al.*. Within this cooperation calculations on a full 6-dimensional *ab initio* PES at highest level of theory (CCSD(T)³ with aug-cc-pV(Q+d)Z basis set for S, aug-cc-pVQZ basis set for O, and aug-cc-pVQZ basis set for H⁴) have been started. Preliminary results of these calculations show an enhanced splitting of the energy-levels in case of the $\nu_{SH} = 1$ state while the splitting for the $\nu_{OH} = 1$ state remains in the size estimated by both the experiment (see Section 8.1) and theory (see Quack and Willeke [102]).

In order to give a graphical explanation of the supposed potential coupling, *ab initio* calculations on the minimum energy path of HSSH and HSOH at the MP3/cc-pVTZ level of theory have been carried out -as part of this thesis- by employing the program package GAUSSIAN03 [43]. The results concerning the geometrical parameters of the molecules are illustrated in Figure 8.12. As one can see in Figure 8.12 (a) the SS-bond of HSSH is drastically effected by the change of the dihedral angle τ , which is in keeping with the observed mode coupling in this molecule. In case of HSOH (Figure 8.12 (b)) the strongest dependency on the dihedral angle motion shows the SO-bond. Nevertheless, the SH-bond is significantly changed, too, while the OH-bond is almost unaffected by the torsional motion. These results may explain qualitatively the potential coupling of the $\nu_{SH} = 1$ state to the manifold of torsionally excited states and hence the observed splitting of transitions in the $\nu_{SH} = 1$ state into doublets, whereas no splittings -and therefore no (or at least only a very small) mode coupling- have been observed in case of the $\nu(\text{OH})$ fundamental vibrational mode (see Section 8.1).

³Coupled cluster theory with all single and double substitutions from the Hartree-Fock reference determinant [101] augmented by a perturbative treatment of connected triple excitations [103, 110] (see also Chapter 3).

⁴For details on the basis sets see references [36, 70, 119, 127] (see also Chapter 3).

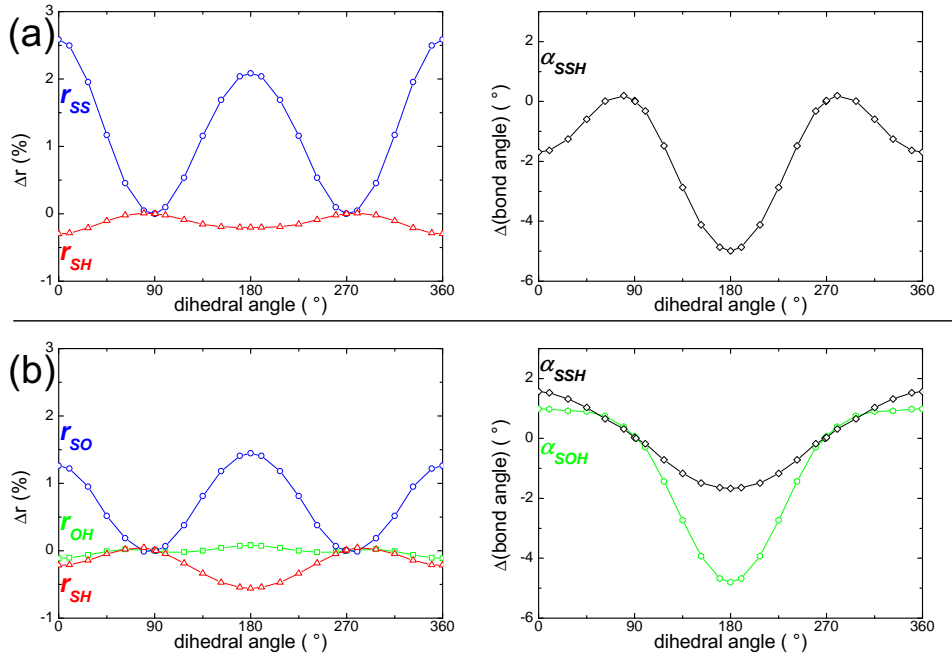


Figure 8.12: *Ab initio* minimum-energy path of the geometry of (a) HSSH and (b) HSOH in dependence of the dihedral angle τ . The change of bond lengths Δr is given relative to the corresponding equilibrium value.

8.2.2 Molecular Parameters

More than 700 transitions have been assigned to *a*- and *b*-type transitions of the $\nu(\text{SH})$ fundamental vibrational mode. Figure 8.13 shows a sketch of *a*- and *b*-type transitions for the $\nu_{\text{SH}} = 1$ state.

Following the ideas by Yamada *et al.* [130] the splitting $\Delta\nu(a)$ and $\Delta\nu(b)$ of *a*- and *b*-type transitions can be related to the splitting $\delta_{K'_a}$ and $\delta_{K''_a}$ of upper and lower energy levels, respectively, by the equations

$$\Delta\nu(a) = \delta_{K'_a} + \delta_{K''_a} \quad (8.2)$$

and

$$\Delta\nu(b) = |\delta_{K'_a} - \delta_{K''_a}|. \quad (8.3)$$

In case of the fundamental SH-stretching mode observed here it is $\delta_{K'_a} \gg \delta_{K''_a}$, and hence the torsional splitting of transitions can directly be related to the splitting of the energy levels in the $\nu_{\text{SH}}=1$ state:

$$\Delta\nu(a) = \Delta\nu(b) = \delta_{K'_a}. \quad (8.4)$$

In the analysis of the $\nu(\text{SH})$ fundamental vibrational mode it has been assumed, that the splitting of the transitions, due to the internal motion in the

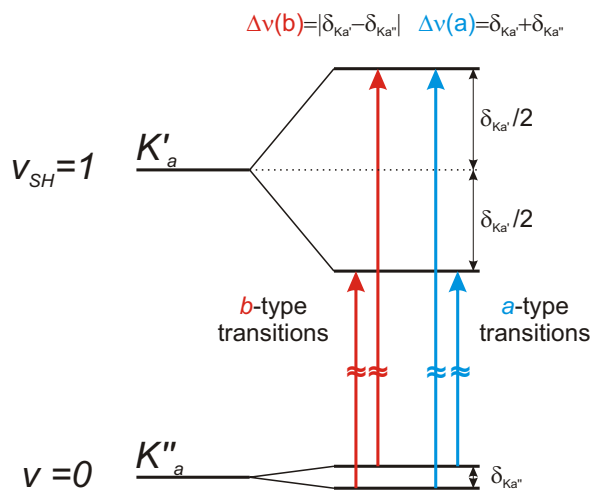


Figure 8.13: Torsional splitting of *a*- and *b*- type transitions in the $v_{SH} = 1$ state.

molecule, is symmetrically around a common center of gravity as indicated in Figure 8.13. Hence, in the fitting procedure every deviation $\delta_{K'_a}/2$ of the common center in dependence of K'_a has been determined as well as a shared set of rotational constants -of a Watson type Hamiltonian in S -reduction (see Section 2.1.2)- for all values of K'_a . All identified *a*- and *b*-type transitions were simultaneously fitted to this model in a least-squares analysis by employing Pickett's [99] program *spfit*. The fit includes transitions up to $J' = 32$ and $K'_a = 7$. The ground state molecular constants were fixed to the highly accurate microwave values derived in Section 9.1 (see Table 9.1). The analysis yields a precise value for the band center frequency of the $\nu(\text{SH})$ stretching mode, its rotational constants A , B , and C , all quartic centrifugal distortion constants D_J , D_K , and D_{JK} , as well as the values for the K'_a dependent splittings $\delta_{K'_a}$ of energy levels. All molecular constants of the vibrationally excited state and for comparison high level *ab initio* values [8, 44] are given in Table 8.3. The fit is in good agreement with the experiment for all K'_a -values except for $K'_a = 1$. In Figure 8.14 the rQ_0 -branch of the $v_{SH} = 1$ state of HSOH is depicted clearly showing a perturbation in the $K'_a = 1$ state. The deviation of assigned transitions in the rQ_0 -branch to the hypothetical unperturbed lines calculated from the constants of the final data analysis are marked in Figure 8.14. The perturbation reveals a strong J -dependence and hence it is very likely a Coriolis-type interaction. Unfortunately any information on the perturbing state is missing. Therefore the lines have been weighted down in the data analysis. The dimensionless weighted root-mean-square deviation of all other transitions have a value of 1.09 indicating to reproduce the experimental data quite well within their uncertainties. This agreement of the experimental data to the introduced model confirms the assumption that the splitting of the transitions, due to the internal motion in the molecule, is symmetrically with respect to a common center of gravity. The fact, that the experimental data could be fitted to a shared set of molec-

Table 8.3: Spectroscopic parameters for the $\nu(\text{SH})$ first excited state of HSOH.

Parameter		theoretical ^a [8, 44]	experimental ^b [this work]
		$\nu_{SH} = 1$ state	$\nu_{SH} = 1$ state
A	MHz	198057.7	197906.3(32)
B	MHz	15298.6	15300.92(74)
C	MHz	14840.7	14840.05(78)
$D_J \times 10^{-3}$	MHz		25.24(35)
D_{JK}	MHz		0.4113(72)
D_K	MHz		5.690(67)
d_1	MHz		-0.7163598 ^c
$d_2 \times 10^{-3}$	MHz		0.2910944 ^c
$H_J \times 10^{-6}$	MHz		-0.015188 ^c
$H_{JK} \times 10^{-6}$	MHz		-1.27723 ^c
$H_{KJ} \times 10^{-3}$	MHz		0.029602 ^c
$H_K \times 10^{-3}$	MHz		0.5352 ^c
$h_1 \times 10^{-9}$	MHz		1.0964 ^c
$h_2 \times 10^{-9}$	MHz		-1.5055 ^c
$h_3 \times 10^{-9}$	MHz		-0.9285 ^c
$\delta_{K_a=0}/2 \times 10^{-3}$	cm ⁻¹		21.35(87)
$\delta_{K_a=1}/2 \times 10^{-3}$	cm ⁻¹		27.92(170)
$\delta_{K_a=2}/2 \times 10^{-3}$	cm ⁻¹		24.02(173)
$\delta_{K_a=3}/2 \times 10^{-3}$	cm ⁻¹		21.02(82)
$\delta_{K_a=4}/2 \times 10^{-3}$	cm ⁻¹		37.33(96)
$\delta_{K_a=5}/2 \times 10^{-3}$	cm ⁻¹		13.68(143)
$\delta_{K_a=6}/2 \times 10^{-3}$	cm ⁻¹		19.61(140)
$\delta_{K_a=7}/2 \times 10^{-3}$	cm ⁻¹		25.78(173)
ν_{SH}	cm ⁻¹	2536.9	2537.9869(12)
α_{SH}^A	MHz	4078.1	4162.7(32)
α_{SH}^B	MHz	-19.7	-18.96(74)
α_{SH}^C	MHz	-0.3	0.16(78)

^a CCSD(T)/cc-pVQZ + CCSD(T)/cc-pVTZ vibrational correction

^b In the analysis values for the $\nu = 0$ state were fixed to data taken from Section 9.1 (see Table 9.1).

^c Values are fixed to constants of the vibrational ground state.

ular parameters validates the use of the semirigid rotor model for HSOH in case of the first excited fundamental SH-stretching mode.

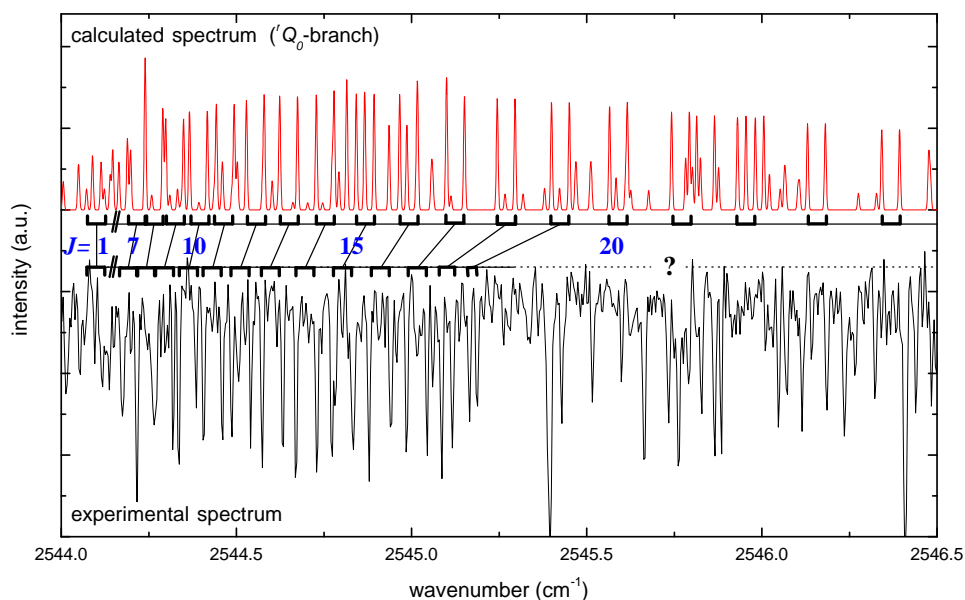


Figure 8.14: rQ_0 -branch of the $\nu_{SH} = 1$ state. In the upper trace a calculated spectrum based on the constants of the final data analysis is depicted. In the lower trace the experimental spectrum is mapped. Assigned transitions in the experimental spectrum are labelled by the rotational quantum number J . The deviation from the assigned to the corresponding calculated transitions is indicated.

8.2.3 Conclusion and Discussion

Although the torsional motion is customarily thought of as one dimensional in nature, in HSOH corresponding to the angle τ , it has been demonstrated that there is ample theoretical and experimental evidence that reality is more complex.

In contrast to the fundamental $\nu(\text{OH})$ stretching vibrational mode the $\nu_{SH} = 1$ state shows a splitting of transitions, due to the internal rotation tunneling, which are by a factor of 20 larger than theoretically expected. Due to the fact, that the torsional splitting in the vibrationally excited SH-stretching state is much larger than the splitting in the vibrational ground state, the splitting of transitions is almost equal to the splitting of energy levels. The observed torsional splittings in the $\nu_{SH} = 1$ state are found to be strongly K_a -dependent (see table 8.3). Within a K_a stack, the torsional splitting associated with K_a shows almost no dependence on the rotational quantum number J (see Figure 8.11). Following the ideas of the *Yamada-Winnewisser-Jensen*-model (see Section 2.3.1) the values of the torsional splittings in the $K_a = 1, 2, 4, 5, 7, \dots$ levels change non systematically, whereas the levels with $K_a = 0, 3, 6, \dots$ have equal splittings. These results are in agreement with the experimentally observed data presented here.

The oversimplified classic picture of mode-coupling in HSOH discussed here is a nice method to get an idea of the involved mechanics, but to get quantitative answers it is necessary to calculate a PES with sufficient accuracy. If such a PES is available the “perturbative instanton approach” by Benderski *et al.* [13] could be a powerful tool to calculate accurate splittings in the vibrational modes, as was already done e.g. for the brethren molecule HOOH [14].

The experimentally derived molecular constants in the $\nu_{SH} = 1$ state are in excellent agreement with those from high level *ab initio* calculations. The values of α_{SH}^A , α_{SH}^B , and α_{SH}^C presented here are -like the values α_{OH}^A , α_{OH}^B , and α_{OH}^C given in Section 8.1 (see Table 8.2)- very close to the *ab initio* values. Hence the theoretically values for α used in Chapter 7 to obtain an empirical equilibrium structure of HSOH, have been confirmed satisfactorily by the experimental results presented in this chapter.

Measurements on HSOH and its isotopologue H^{34}SOH at 1.3 THz

HSOH can be considered as a link between the two well known homo-nuclear species, HSSH [120] and HOOH [95]. Molecules of the type XYYX (with $\text{X}=\text{H},\text{D}$ and $\text{Y}=\text{S},\text{O}$) have two equivalent equilibrium conformations which are most simple representatives of molecular enantiomers. The tunneling between the corresponding two minima of the potential energy surface, which is an internal rotation (torsion) about the heavy atom bond YY , causes the observed rotational transitions to split into doublets. This tunneling splitting of the rotational transitions is well studied in case of HSSH and HOOH. The observed splitting depends on both, the height of the potential barrier and on the K_a projection quantum number of the total angular momentum, J . K_a is almost a good quantum number because the molecules of type XYYX are almost symmetric prolate tops.

In case of HSSH and HOOH it was found, that the size of the splitting alternates with K_a in modulo two [95, 120]. This phenomenon is best explained by a theoretical model introduced by Hougen [62, 63]. Obviously, HSOH is of lower symmetry than the C_2 molecules HSSH and HOOH. Hence, the tunneling splitting is found to be a more complicated function of K_a , which was subject of a recent theoretical treatment by Yamada, Winnewisser, and Jensen (YWJ) [130] (see also Section 2.3.1). Their model is presented in terms of a relatively simple parameterized form of the internal rotation dynamics in HSOH. It predicts the variation of the energy level tunneling splitting values to be largest and almost identical in case of $K_a = 0, 3, 6, \dots$, which is in keeping with the experimentally derived quantities of 64.5 MHz and 62.9 MHz for $K_a = 0$ and $K_a = 3$, respectively. Due to the lack of experimental data for energy level splittings with $K_a > 3$ Yamada *et al.* were not able to determine all variables in their model. Hence, the verification of the predictive power for energy-level splittings with $K_a = 1, 2, 4, 5, \dots$ still remains.

The purpose of the studies presented in this chapter is mainly twofold: (a) to determine the torsional splitting of $K_a = 4$ and $K_a = 5$ energy levels experimentally for testing a new -by Ovsyannikov *et al.* developed- theoreti-

cal model complementing the YWJ model (see Section 2.3.1) and (b) to give precise data for improved molecular parameters of the ³²S and ³⁴S main isotopologues of HSOH. Compared to the ³²S main isotopologue spectral data on the ³⁴S species are rather sparse. Nevertheless, due to the high sensitivity of the 1.3 THz multiplier spectrometer employed for the present measurements (see Chapter 4) and the good efficiency of the synthesis of HSOH via the pyrolysis (see Section 5.1), it was possible to record the H³⁴SOH spectra in natural abundance.

In course of the measurements presented here another unexpected effect reveals in the recorded spectra: It turned out that all *b*-type transition are missing in the ^rQ₃-branch.

This chapter is structured as follows: Details on the recorded H³²SOH and H³⁴SOH spectra and the data analysis including previous measurements are given in Section 9.1. The tunneling splitting of $K_a = 4$ and $K_a = 5$ levels¹ have been derived from combination differences and are compared to recently improved *ab initio* calculations in Section 9.2. The molecular parameters derived from these highly accurate measurements allow to predict line positions of *b*-type transitions of the ^rQ₃-branch within less than 50 kHz. Nevertheless not a single *b*-type transition has been recorded. This unexpected finding is discussed in Section 9.3.

9.1 The ^rQ₃-branch of HSOH and its isotopologue H³⁴SOH

The permanent electrical dipole moment of HSOH is pointing almost perpendicular to the S-O bond and towards the angle bisector of the dihedral angle. Hence, a perpendicular type spectrum is observed which exhibits strong *Q*-branches at distances $(A - (B + C)/2)(2K_a + 1)$, with *A*, *B*, and *C* the rotational constants and K_a the projection of the angular momentum onto the symmetry axis. The ^rQ _{$K_a''=0,1,2$} -branches of HSOH occur at 187, 561, and 935 GHz, respectively. Molecular constants from a previous study by Winnewisser *et al.* [123] have been used to predict line positions of the ^rQ₃-branch occurring at 1.308 THz, which leads to a clear identification of the here presented spectra in the region between 1.295 THz and 1.308 THz. Part of the ^rQ₃ band head spectrum of H³²SOH at 1.308 THz is depicted in the upper trace of Figure 9.1(a). The tunnel effect splits rotational transition into two components which in case of the ^rQ₃-branch are found to be separated by 120 MHz. The stick diagrams in Figure 9.1 shows the two tunnel components and the assignment of rotational transitions to the quantum

¹Data from $K_a = 5 \leftarrow 4$ transitions of an earlier work [123], which were recorded employing the Cologne Laser Sideband Spectrometer (COSSTA), have been used to determine the tunneling splitting of the $K_a = 5$ levels. COSSTA combines the fix frequency of a FIR gas laser at 1.9 THz with a tunable output frequency of a 300 GHz BWO. Details of the spectrometer are published by Lewen *et al.* [137].

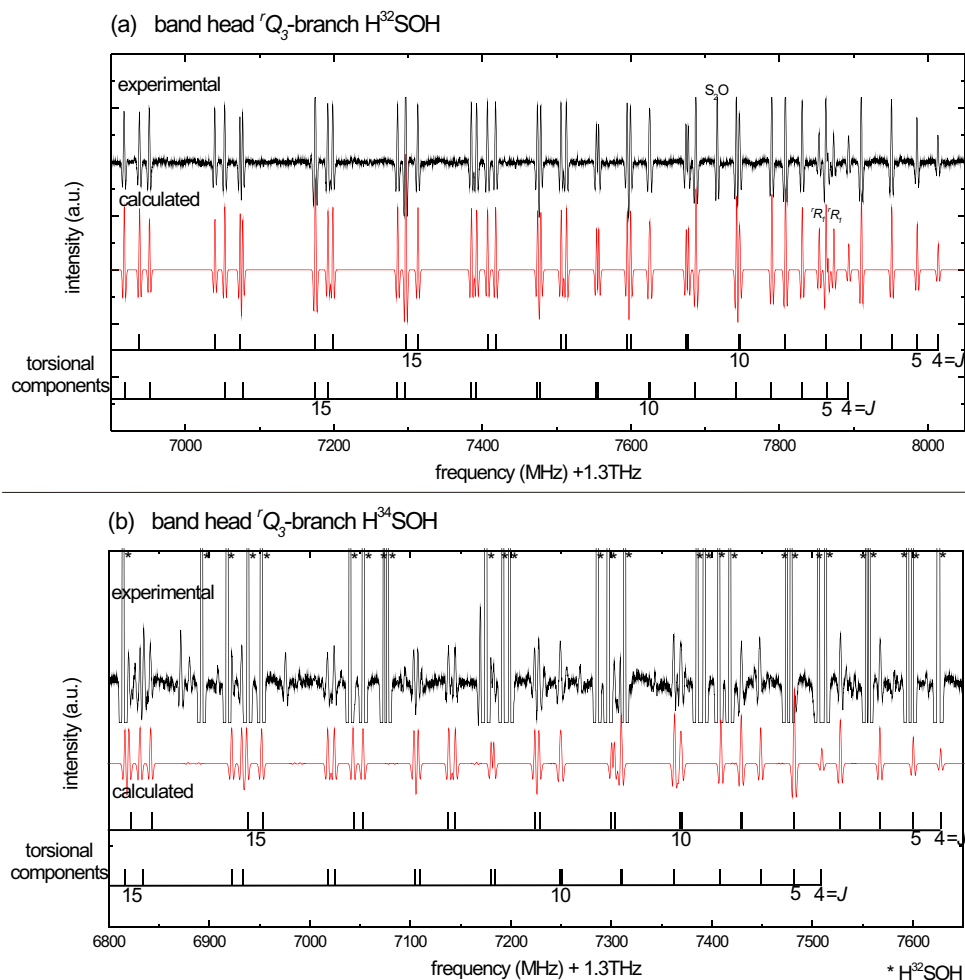


Figure 9.1: Band head of the rQ_3 -branch of (a) HSOH and its isotopologue (b) H³⁴SOH. In each case the experimental spectrum is depicted in the upper trace, while in the lower trace a calculated spectrum based on the molecular parameters of the final data analysis is plotted.

number J . As can be seen, the tunneling splitting is almost J independent. Further, each rotational transition split into a doublet due to the internal asymmetry of the molecule, which in case of HSOH is small because of almost identical B and C rotational constants. Progression of the asymmetry splitting with increasing J quantum numbers is best to be seen from the stick diagram in Figure 9.1(a). All lines of the rQ_3 -branch up to $J = 40$ have been assigned.

Corresponding to their isotopic ratio, transitions of the H³⁴SOH isotopologue are by a factor of 20 weaker than H³²SOH transitions. Due to the high sensitivity of the employed spectrometer, 36 transitions of the H³⁴SOH rQ_3 -branch could be measured in natural abundance. Figure 9.1(b) shows the rQ_3 -branch spectrum at a magnified scale.

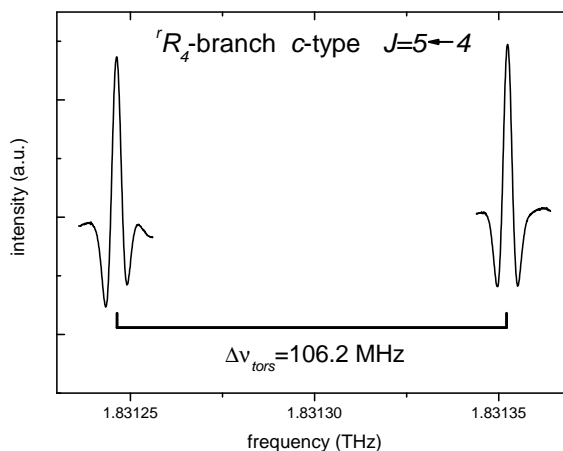


Figure 9.2: $J = 5 \leftarrow 4$ c-type transition of the rR_4 -branch.

Fortrat-diagrams for (a) H³²SOH and (b) H³⁴SOH in the interval from 0 to 2 THz are displayed in Figure 9.3, showing the positions of Q -branches with $K_a'' = 0, \dots, 4$. Details on the here studied rQ_3 -branches are depicted in Figure 9.3(a) and (b) at the lower traces in high frequency dispersion. New lines assigned in course of this work are marked in red while lines measured in previous work [123] are marked in blue.

For the main isotopologue H³²SOH the data set now contains 617 assigned transitions in total, from which 142 lines at 1.3 THz were added to the transitions reported in earlier work [123]. 132 of the 142 measured lines were assigned to rQ_3 -branch, 8 to rR_2 -branch, and 2 to rR_1 -branch transitions of H³²SOH.

All 617 transitions were finally analyzed in a global fit and improved parameters were obtained from fitting the data to a Watson Hamiltonian in S -reduction. To account for torsional splitting and interaction of the torsional substates, a two-state fit has been used. This fit is successful for all lines except for the $K_a = 5 \leftarrow 4$ transitions at 1.9 THz. Nevertheless, the center frequencies, which are obtained by setting the splitting to zero, is very well reproduced and hence in case of $K_a = 5 \leftarrow 4$ transitions the position of split lines is described by the center frequencies plus a constant, J independent value for the splitting. Figure 9.2 shows the two components of tunneling splitting for the $J = 5 \leftarrow 4$ c-type transition in the rR_4 -branch at 1.83 THz.

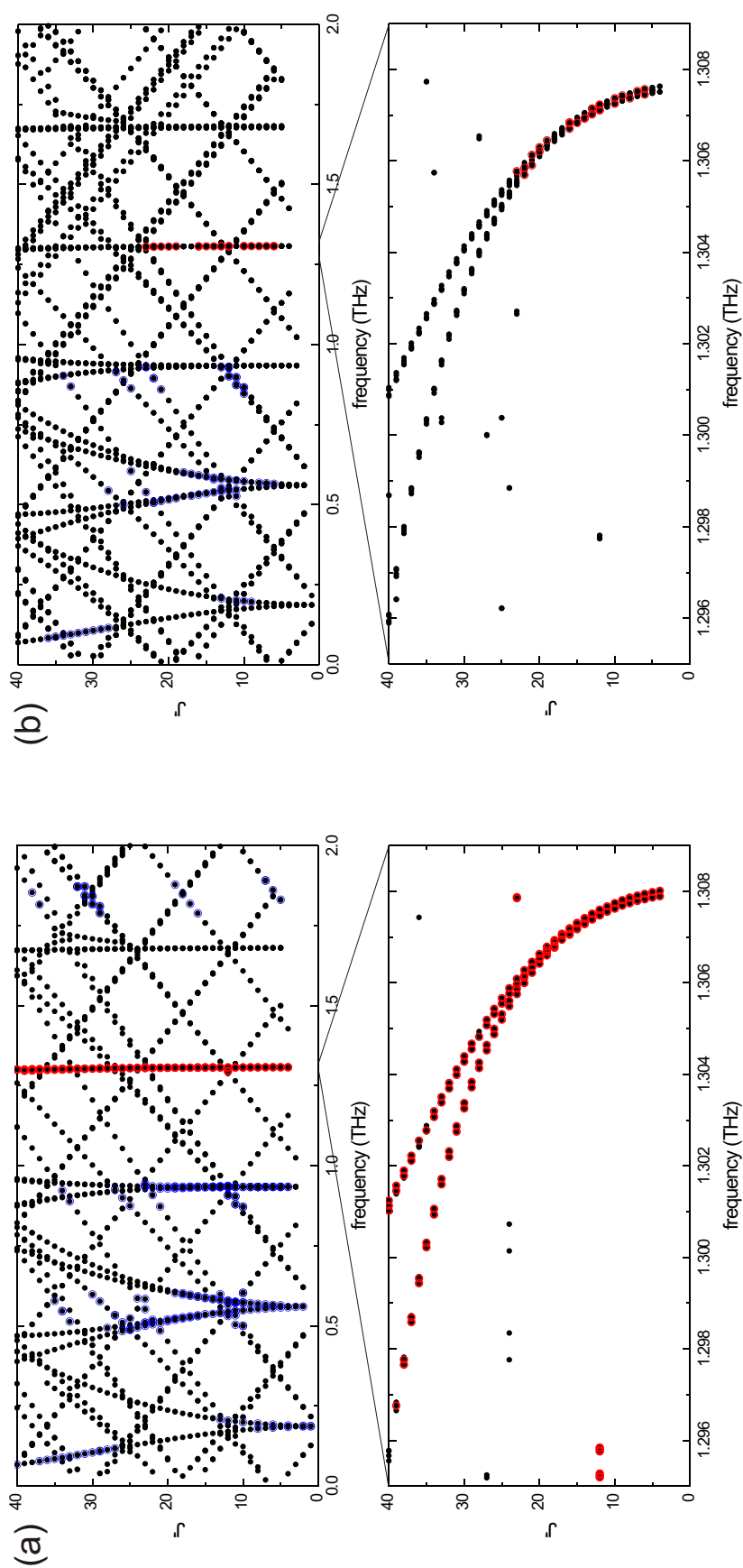


Figure 9.3: Fortrat diagram of (a) HSOH and its isotopologue (b) $H^{34}SOH$. Experimentally assigned lines are marked by circles (blue [123] and red [this work]). The blow-ups in the lower traces show the details of the rQ_3 band center regions at 1.308 THz.

As can be seen from the Fortrat diagram in Figure 9.3(b) the data set of H³⁴SOH is less complete referred to the main isotopologue. It contains 116 transitions up to 930 GHz. Since transitions above 1 THz were completely missing the here presented 36 new assigned rQ_3 -branch transitions at 1.3 THz led to a substantial improvement of the H³⁴SOH data set. Molecular constants obtained from a global analysis of all H³²SOH and H³⁴SOH transitions are listed in Table 9.1. For comparison the results of the previous study by Winnewisser *et al.* [123] are depicted in the table, too. Spectra calculated from the new set of molecular parameters are plotted in Figure 9.1(a) for H³²SOH and (b) for H³⁴SOH, showing in a convincing manner how well the measurements can be reproduced by the set of molecular parameters.

Table 9.1: Ground state molecular parameters (MHz) of H³²SOH and H³⁴SOH.

Parameter	H ³² SOH [123]	H ³² SOH [this work]	H ³⁴ SOH [123]	H ³⁴ SOH [this work]
A	202069.05431(134)	202069.04428(118)	201739.7641(129)	201739.7540(172)
$\Delta A/2$	-14.3805(39)	-14.3842(37)	-14.0255(139)	-12.839(76)
B	15281.956620(123)	15281.956038(115)	15001.43940(38)	15001.43809(64)
$\Delta B/2 \times 10^3$	-2.7622(135)	-2.7938(119)	-2.686(89)	-2.595(95)
C	14840.216440(121)	14840.215621(114)	14573.77816(39)	14573.77801(58)
$\Delta C/2 \times 10^3$	4.3548(77)	4.3469(71)	4.155(38)	4.196(49)
$D_J \times 10^3$	24.528463(138)	24.528194(132)	23.690720(304)	23.68897(100)
$\Delta D_J/2 \times 10^6$	0.3786(53)	0.3658(34)	0.266(44)	0.365(58)
D_{JK}	0.3904340(48)	0.39035886(308)	0.3787713(163)	0.378827(53)
$\Delta D_{JK}/2 \times 10^3$	0.2970(55)	0.2688(35)	0.3125(139)	0.469(44)
D_K	5.989715(202)	5.989574(172)	5.97102(211)	5.9662(34)
$\Delta D_K/2$	-1.07594(139)	-1.07513(128)	-0.79910(279)	0.757(98)
$d_1 \times 10^3$	-0.7161682(196)	-0.7163598(178)	-0.681897(51)	-0.681219(220)
$\Delta d_1/2 \times 10^6$	-0.0220(35)	-0.01190(290)	-0.041(37)	-0.045(39)
$d_2 \times 10^3$	0.2911054(104)	0.2910944(97)	0.270603(86)	0.270797(281)
$\Delta d_2/2 \times 10^6$	0.2907(52)	0.3035(42)		0.166(81)
$H_J \times 10^6$	-0.015109(38)	-0.015188(37)	-0.014 ^a	-0.01481(55)
$H_{JK} \times 10^6$	-1.1950(39)	-1.27723(222)	-1.2 ^a	-1.091(62)
$\Delta H_{JK}/2 \times 10^6$	0.0565(33)	0.04631(151)	-0.05 ^a	-0.065(54)
$H_{KJ} \times 10^3$	0.02987(32)	0.029602(113)	0.03 ^a	0.0260(33)
$\Delta H_{KJ}/2 \times 10^3$	0.01297(72)	0.00925(39)	0.014 ^a	0.0631(37)
$H_K \times 10^3$	0.6042(114)	0.5352(70)	0.6567 ^a	0.471(142)
$\Delta H_K/2 \times 10^6$	-0.031089(203)	-0.030920(155)	0.0227 ^a	0.4178(242)
$h_1 \times 10^9$	1.0178(79)	1.0964(70)	1.00 ^a	0.665(225)
$h_2 \times 10^9$	-1.5560(82)	-1.5055(55)	-1.50 ^a	-1.56(67)
$h_3 \times 10^9$	-0.9528(209)	-0.9285(67)	-0.9 ^a	2.20(173)
$\Delta L_K/2 \times 10^3$	0.3717(112)	0.3737(61)		-0.02012(122)
ΔE	64.5051(63)	64.5151(59)	64.1870(291)	64.1668(311)
G_a	-32.786(42)	-35.6631(223)	-12.0193(270)	-35.6631 ^b
G_{aK}	6.1807(154)	7.2182(81)		7.2182 ^b
$G_{aJK} \times 10^3$	0.0705(79)	0.0293(65)		0.0293 ^b
G_{aKK}	-0.24569(119)	-0.32596(54)		-0.32596 ^b
$G_{aJ} \times 10^3$	0.645(78)	0.138(81)		0.138 ^b

^a fixed at the value shown.

^b fixed in the analysis to the values of H³²SOH.

9.2 Internal rotation tunneling in HSOH

The experimental pure-rotational spectra of HSOH and its isotopologues exhibit splittings caused by internal rotation tunneling in the molecule. The splittings were observed for all transitions in HSOH and found to be clearly K_a -dependent. The observed values of the line frequency splitting in ${}^rQ_{K_a}$ -branches due to the torsional tunnelling depend also on J , especially for the rQ_1 - and rQ_2 -branch, as plotted in Figure 9.4. Because of the strongly non-

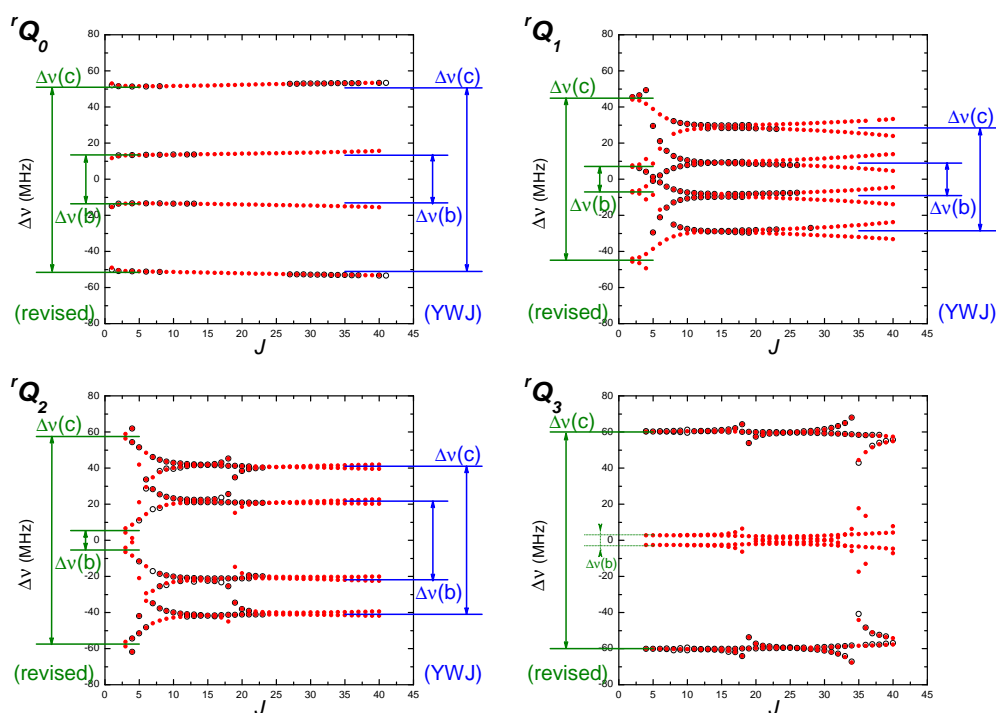


Figure 9.4: Torsional splitting for b - and c -type transitions of the ${}^rQ_{K_a}$ -branches with $K_a = 0, 1, 2, 3$. To the right of each diagram the values given in reference [130] are depicted in blue, whereas the revised values given in this work are shown on the left (green). Experimentally assigned transitions are marked by black circles.

linear J dependence in the low- J region, the splitting values extrapolated to $J = 0$ reported by Yamada, Winnewisser, and Jensen (YWJ) [130] (see Table 9.2) were in error for the rQ_1 - and rQ_2 -branch; they are the values for $J \approx 10$ as one can see in Figure 9.4. Besides the experimental values (black circles) also predicted transition splittings (red dots) -based on the best fit parameters- are plotted in Figure 9.4. With help of these calculated transition splitting the splitting values for the minimum J of each ${}^rQ_{K_a}$ -branches have been evaluated. The revised values for the minimum J of the internal rotation splitting observed in the transitions of the ${}^rQ_{K_a}$ -branches ($K_a = 0, 1, 2, 3$) and the rR_4 -branch of HSOH are listed in Table 9.2. Yamada *et al.* [130]

Table 9.2: Experimental tunnelling splittings of transitions in MHz.

branch	$\Delta\nu(c)$ [130]	$\Delta\nu(c)$ [this work]	$\Delta\nu(b)$ [130]	$\Delta\nu(b)$ [this work]
rQ_0	102.0	102.0	26.6	27.0
rQ_1	57.0	89.8	18.0	14.2
rQ_2	82.0	115.0	43.5	10.8
rQ_3		120.0		— ^a
rR_4		106.2		— ^b

^a no b -type transitions have been observed in this work. For details see Section 9.3

^b No data on b -type transitions are available from the previous work [123]

pointed out, that the observed line-frequency splittings can be related to the tunneling splittings δ_{K_a} of energy levels with a given value of K_a by means of the selection rules for the rQ_0 - and ${}^rQ_{K_a>0}$ -branches (these selection rules are illustrated schematically in Figures 9.5 (a) and (b))². For the splitting

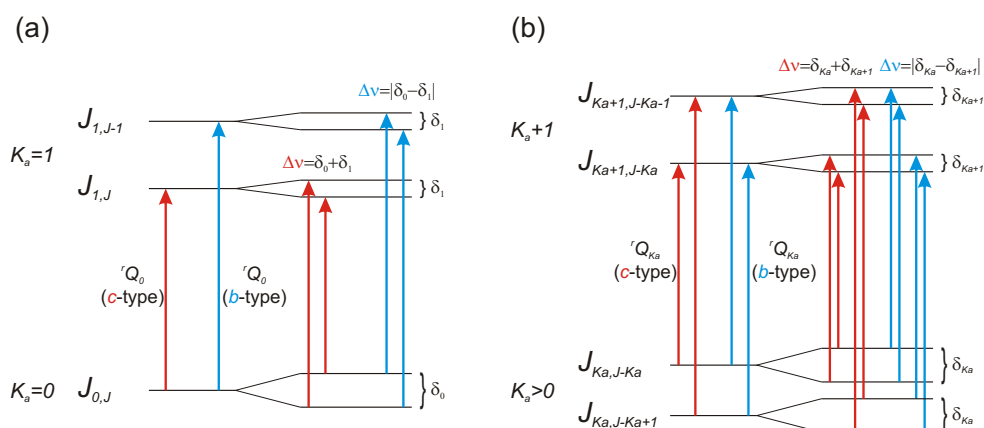


Figure 9.5: The (a) rQ_0 and (b) ${}^rQ_{K_a>0}$ transitions of HSOH. Arrows indicate the individual components of the transitions. On the left hand side of the figures (a) and (b), the asymmetric rotor levels are labeled by J_{K_a, K_c} , and the b - and c -type transitions are indicated. Due to the internal tunneling, these transitions are doubled as illustrated on the right hand side of the figures (a) and (b).

of transitions with minimum J -value -as given in Table 9.2- one obtains (in

²By assuming the torsional splitting to be almost J -independent the equation $\Delta\nu(c) = \delta_4 + \delta_5$ holds true for R -branch transitions with $K_a = 5 \leftarrow 4$.

units of MHz):

$$|\delta_0 - \delta_1| = 27.0 \quad (9.1)$$

$$\delta_0 + \delta_1 = 102.0 \quad (9.2)$$

$$|\delta_1 - \delta_2| = 14.2 \quad (9.3)$$

$$\delta_1 + \delta_2 = 89.8 \quad (9.4)$$

$$|\delta_2 - \delta_3| = 10.8 \quad (9.5)$$

$$\delta_2 + \delta_3 = 115.0 \quad (9.6)$$

$$\delta_3 + \delta_4 = 120.0 \quad (9.7)$$

$$\delta_4 + \delta_5 = 106.2. \quad (9.8)$$

For a certain K_a the value of δ_{K_a} should be common for all transitions. Therefore there is a solution to the set of equations (9.1)–(9.8)³.

The values obtained for the energy level splitting (for the minimum J) are summarized in Table 9.3.

Table 9.3: Observed and calculated internal rotation splittings δ_{K_a} (MHz) for energy levels with $K_a = 0, \dots, 5$.

K_a	experimental δ_{K_a} [this work]	theoretical δ_{K_a} [89]
0	64.5	64.5
1	37.8	37.9
2	52.1	55.3
3	62.9	64.0
4	57.2	58.8
5	49.0	52.9

Obtained by extrapolating the J -dependent splittings of the individual states to the minimum value of J for each level.

Yamada *et al.* conclude in their model [130], that the splittings δ_{K_a} of the energy levels should be similar for $K_a = 3t = 0, 3, 6, \dots$ (t : integer) and they found this result to be in agreement with the only somewhat different observed values $\delta_0 = 64.5$ MHz and $\delta_3 = 62.9$ MHz for these quantities. Furthermore, they predict for $K_a = 3t \pm 1 = 1, 2, 4, 5, 7, 8, \dots$ (t : integer) the energy level splittings to change erratically, but not to be periodic with a period of 3, as one could by mistake suspect. This result has been confirmed experimentally for the first time by the results presented here.

The δ_1 is especially small, about half of δ_0 ; this is caused by the large K -doubling for $K_a = 1$ as analytically shown in the YWJ-model (Section 2.3.1) as the asymmetric top limit (equation (2.89)). The strong non-linear dependence of the splitting observed in the rQ_1 - and rQ_2 -branch are caused mainly

³If the experimental values for δ_{K_a+1} differ slightly for ${}^rQ_{K_a}$ and ${}^rQ_{K_a+1}$ ($K_a = 0, 1, 2$) transitions the average value is taken.

by the J -dependent splitting for the $K_a = 2$ levels. For $K_a = 2$, the energy splitting can be evaluated by the symmetric top limit (equation (2.90)) for low J , but it is expressed by the asymmetric top limit for high J . The observed transitions are mainly related to the levels of the intermediate case, for which the splitting behavior is very non-linear. For the other K_a levels, we have found almost J -independent constant torsional splitting values.

In a collaboration with Ovsyannikov *et al.* [89] the results presented here have been used to evaluate a new theoretical treatment complementing the work given by Yamada *et al.* [130]. Ovsyannikov *et al.* take a more direct approach for calculating the torsional splitting by employing a newly computed *ab initio* potential energy surface together with the program TROVE (see Section 3.2). The splittings obtained by this approach are in excellent agreement with the experimental results presented here (see Table 9.3).

9.3 Intensity anomaly in *b*-type transitions of HSOH

The HSOH molecule is expected to display a rotational spectrum in the vibrational ground state with extremely weak *a*-type transitions and a dominating perpendicular-type spectrum with strong *c*-type and somewhat weaker accompanying *b*-type transitions, as can be understood from theoretical values (Table 9.4) of the dipole-moment components μ_a , μ_b , and μ_c . Surprisingly,

Table 9.4: Permanent dipole moment components for HSOH (in Debye) calculated at various theoretical levels (see reference [123])

	μ_a	μ_b	μ_c
MP2/cc-pVTZ	0.0435	0.8030	1.4808
CCSD(T)/cc-pVTZ	0.0544	0.7731	1.4644
CCSD(T)/cc-pVQZ	0.0182	0.7682	1.4321
CCSD(T)/cc-pCVTZ	0.0441	0.7729	1.4329

no *b*-type transitions have been observed in case of the measurements on the rQ_3 -branch presented here.

In Figure 9.1 the band head of the rQ_3 -branch of HSOH is depicted and the assignment of the lines to *c*-type transitions is given via the stick-spectrum. In the calculated⁴ spectrum -shown in the lower traces of Figure 9.1(a)- *b*-type transitions have been ignored. The excellent agreement of the experimental and the calculated spectrum shows the high quality of the molecular parameter set given in Table 9.1. By using these rotational constants, the frequencies of the corresponding *b*-type transitions in the rQ_3 -branch ($J \leq 30$) can be predicted with an accuracy of at least 50 kHz. In more detail, components of *b*-type transitions always should appear in between those of the corresponding *c*-type transitions (see Figure 9.5). For low values of J the asymmetry splitting of lines is not resolved and therefore *c*- and *b*-type transitions should occur at same frequency (grey line in Figure 9.6). Nevertheless, the splitting due to the internal rotation tunneling has to be considered. Lines belonging to *c*-type transitions split by $\Delta\nu(c)_{K_a} = \delta_{K_a} + \delta_{K_a+1}$ and those belonging to *b*-type transitions by $\Delta\nu(b)_{K_a} = |\delta_{K_a} - \delta_{K_a+1}|$, respectively (see Section 9.2). In case of the rQ_3 -branch the torsional splitting of *c*-type transitions is found to be

$$\Delta\nu(c)_3 = 120 \text{ MHz}, \quad (9.9)$$

while *b*-type transitions are expected to split by

$$\Delta\nu(b)_3 = |\delta_3 - \delta_4| = 5.7 \text{ MHz} \quad (9.10)$$

with $\delta_3 = 62.9$ MHz and $\delta_4 = 57.2$ MHz as given in Table 9.3.

In Figure 9.6 the unique pattern of -due to the internal rotation tunneling splitted- expected transitions within the rQ_3 -branch (for low values of J) is

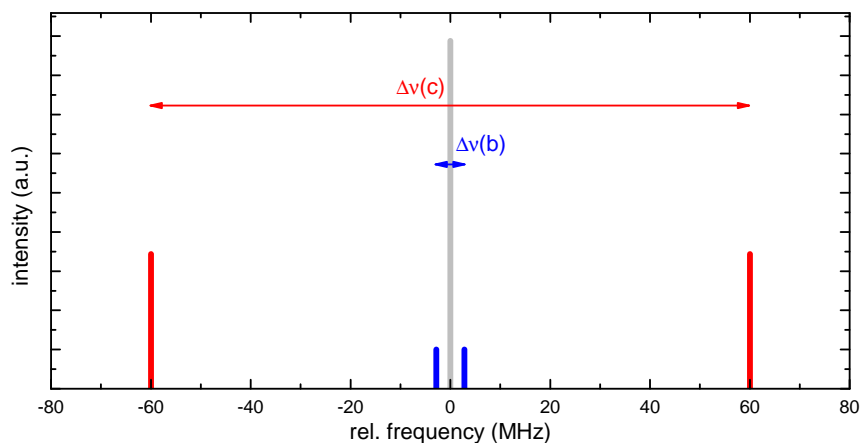


Figure 9.6: Unique pattern of hypothetical *b*- and *c*-type transitions in the rQ_3 -branch. If the asymmetry splitting is neglected *b*- and *c*-type transitions occur at same relative frequency (grey line at 0 MHz). By taking the torsional splitting into account the *b*- and *c*-type transitions are splitted by $\Delta\nu(b)$ and $\Delta\nu(c)$ (blue lines in case of *b*-type transitions and red lines in case of *c*-type transitions, respectively). The relative intensities are based on the theoretical calculations given in Table 9.4

depicted. The grey line in the stick spectrum indicates the hypothetical position of the not splitted and hence overlapped *b*- and *c*-type transitions, while the blue and red lines gives the positions of the *b*- and *c*-type transitions if the torsional splitting is taken into account.

By scanning for this unique pattern the assignment of all expected transitions in the spectrum should be straight forward. Nevertheless, no *b*-transitions could be found in the recorded spectra.

According to the calculated values for the permanent dipole moment components (see Table 9.4), the intensity of *b*-type transitions is expected to be about 4 times weaker than the corresponding *c*-type transitions shown in Figure 9.1(a), but they should be 5 times stronger compared to *c*-type transitions of H³⁴SOH depicted in Figure 9.1(b). This allows only for the conclusion that no *b*-type transitions occur in the rQ_3 -branch or they are at least by more than an order of magnitude less intense than expected.

Triggered by this unexpected result the intensities of *b*- and *c*-type transitions in the already known⁵ rQ_0 -, rQ_1 -, and rQ_2 -branches have been reexamined.

In Figure 9.7(a) the band head of the rQ_2 -branch of HSOH is depicted. In part (b) and (c) of this figure the assignment of the lines to *b*- and *c*-type transitions, respectively, are given via the Fortrat diagrams displayed in the lower traces. The match between the calculated and the experimental spec-

⁴The calculation is based on the constants derived in the final data analysis (see Table 9.1).

⁵see reference [123]

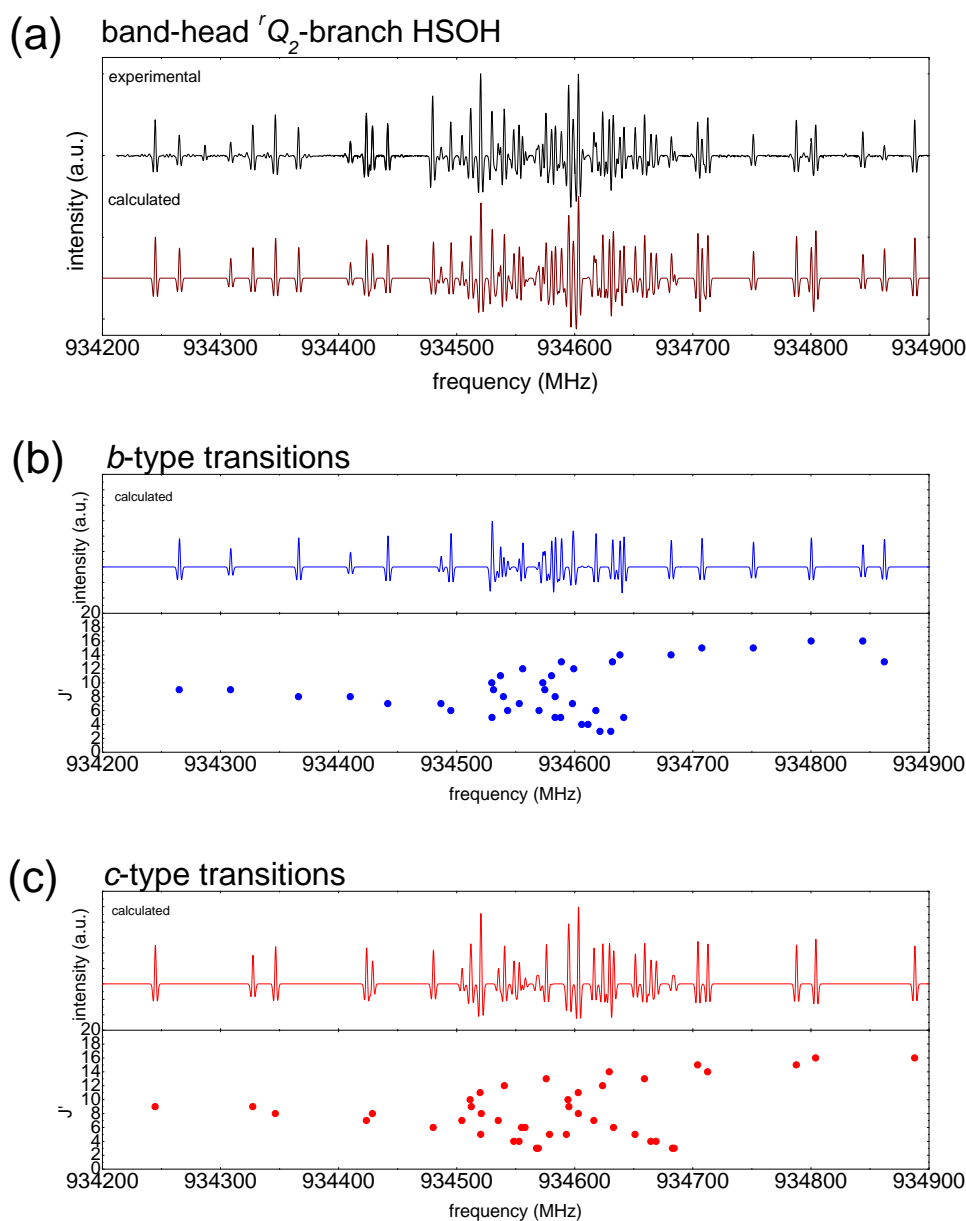


Figure 9.7: rQ_2 -branch of HSOH. In (a) the experimental spectrum and a μ -based on the constants of the final data analysis (see Table 9.1)- calculated spectrum are depicted. In (b) and (c) calculated sub-bands belonging to *b*- and *c*-type transitions, respectively are shown. In order to get the best agreement between the experimental and calculated spectrum, the ratio μ_b/μ_c of dipole moment components have been adjusted to the value of 0.76. The assignment of individual transitions is given via the corresponding Fortrat diagrams.

trum shown in Figure 9.7(a) is excellent. Since the calculated spectrum in (a) is the direct superposition of the two calculated hybrid-bands belonging to *b*- and *c*-type transitions -displayed in parts (b) and (c) of Figure 9.7- it

is evident that several lines occurring in the spectrum have to be assigned to *b*-type transitions. Note, the measured intensities of the *b*- and *c*-type transitions in the rQ_2 -branch are of same order. This result is -like the missing *b*-type transitions in case of the rQ_3 -branch- in disagreement with the theoretically predicted permanent dipole moment components given in Table 9.4.

In Table 9.5 the averaged ratio S_b/S_c of the intensities S_b , corresponding to *b*-type transitions, and S_c of *c*-type transitions are given for the rQ_0 -, rQ_1 -, rQ_2 -, and rQ_3 -branches. All spectra of *Q*-branch transitions have been measured in second derivative (*2f*-mode). Due to the fact that the relative intensities are the same for *0f*- and *2f*-mode, the areas below the curves of *b*- and *c*-type transitions have been used as quantities for the intensities S_b and S_c , respectively. To take into account the different population of energy levels, the ratio S_b/S_c has been calculated only if corresponding (involving the same quantum number *J*) *b*- and *c*-type transitions were available. The ratio S_b/S_c given in Table 9.5 -for a certain ${}^rQ_{K_a}$ -branch- is the average value of all ratios $S_b/S_c|_J$ available. The intensity ratio S_b/S_c observed in case of

Table 9.5: Theoretical and experimental intensity ratio S_b/S_c of *b*- and *c*-type transitions in the ${}^rQ_{K_a}$ -branches ($K_a = 0, 1, 2, 3$)

branch	S_b/S_c
${}^rQ_{K_a}$ ($K_a = 0, 1, 2, 3$)	0.29 ^a
rQ_0	0.22(4)
rQ_1	0.23(2)
rQ_2	0.58(11)
rQ_3	$\ll 0.02$

^a $S_b/S_c = \mu_b^2/\mu_c^2$ (μ_b and μ_c are taken from CCSD(T)/cc-pCVTZ calculations (see reference [123]))

the rQ_0 - and rQ_1 -branch, respectively, are well described by the permanent dipole moment components. Nevertheless, the value of $S_b/S_c=0.58$ for transitions with $K_a = 3 \leftarrow 2$, as well as the not observed *b*-type transitions in case of the rQ_3 -branch, are completely unexpected.

9.4 Conclusion and Discussion

In course of this thesis an active multiplier-chain (see Section 4.2.1) has been introduced to perform high resolution spectroscopy on HSOH at 1.3 THz for the first time. The depicted spectra in Figure 9.1 emphasize the high quality of the entire experimental setup that has been employed.

The measurements presented here are the highest in frequency for the isotopologue H^{34}SOH so far, thus the fit of the rotational parameters could be significantly improved. In Table 9.1 all results of the fit are summarized. Besides the excellent refinement of the H^{34}SOH data set, also the fit on the H^{32}SOH parameters has been improved.

The measurements on $K_a = 4 \leftarrow 3$ transitions presented here bridged the gap to previously reported measurements [123] on $K_a = 5 \leftarrow 4$ transitions. Hence, it became possible to experimentally determine the torsional splitting for energy levels with $K_a = 4$ and 5 for the first time. Furthermore, the highly precise molecular constants allowed to calculate accurate transition splittings (for $K_a = 1 \leftarrow 0$, $K_a = 2 \leftarrow 1$, $K_a = 3 \leftarrow 2$, and $K_a = 4 \leftarrow 3$) (see Figure 9.4). With help of these values the torsional splittings reported by Yamada *et al.* [130] have been revised. The new data set of energy level splitting for $K_a = 0, \dots, 5$ have been used to validate calculations by Ovsyannikov *et al.* complementing the YWJ-model (see Section 2.3.1).

The intensities of *b*-type transitions within the rQ_0 , rQ_1 , rQ_2 , and rQ_3 -branches of the torsional-rotational spectrum in the vibrational ground state of HSOH are found to exhibit an anomalous behavior. From the standard theory (see Section 2.1.3) the unperturbed intensities of spectral lines should be independent from the involved K_a -levels and proportional to the corresponding squared dipole moment component. Nevertheless, a strong K_a -dependence has been observed in the measurements on HSOH presented here (see Table 9.5).

To get a reasonable explanation for this unexpected alternation of the observed intensities a complete electric dipole moment surface for the electronic ground state of the HSOH molecule has been calculated by Yachmenev *et al.* [129]⁶. The *ab initio* calculations are carried out by means of the coupled cluster CCSD(T) method (i.e., including all single and double excitations and a perturbative term for connected triple substitutions) with the augmented correlation-consistent polarized aug-cc-pVTZ basis set. This surface has been used for calculating transition moments for selected vibrational bands in the ground electronic state of HSOH and for simulating a detailed

⁶Collaboration within the European project “*Quantitative Spectroscopy for Atmospheric and Astrophysical Research*” (QUASAAR)

pure torsional-rotational absorption spectrum of this molecule. The calculations have been carried out by means of the recently developed program TROVE [132] for describing the nuclear motion, and they are based on a new high-level (CCSD(T)/aug-cc-pVQZ) *ab initio* potential energy surface for HSOH [133].

Preliminary results show the observed intensity anomalies to be related to state mixing, i.e. the torsional tunneling effect mixes the state of different K_c -levels due to the low symmetry, C_1 , of the molecule. Hence, it turned out that in the symmetric top limit ($K_a > 3$) the type of transitions, *b*- or *c*-type, can not be distinguished anymore. As a result only one type of transitions occurs with its intensity proportional to $\mu_b^2 + \mu_c^2$ for high values of K_a .

The mathematical treatment introduced by Yachmenev *et al.* is more general and not restricted to the molecule HSOH. Therefore, it gives strong evidence that this effect is not constrained to HSOH but may be present for all asymmetric top molecules bearing a hindered internal motion. Thus, a future goal is to find another candidate molecule to verify the common validity of the model by Yachmenev *et al.*.

The assignment of transitions in case of HSOH is, however, clear for the transitions of $K_a = 1 \leftarrow 0$, due to the large K -type doubling of the $K_a = 1$ level. From those it is found that the *b*-type transitions occur between the torsional states with same parity and the *c*-type transitions occur between the torsional states with different parities (see Figure 9.5). This principle is applied throughout the whole work presented here.

Conclusion and Prospects

In course of this thesis many different traits of the elusive species HSOH have been studied. In a collaboration with the Department of Anorganic Chemistry of the University of Cologne new ways of synthesizing oxadisulfane, HSOH, and its isotopologues have been investigated. It turned out, that HSOH is quite abundant in a *rf*-discharge plasma of pure sulfur and water. This finding opened an “easy way” of synthesizing the singly deuterated species HSOD using HDO instead of H₂O.

Guided by high-level *ab initio* calculations it was possible to assign the rotational spectra of singly deuterated oxadisulfane, HSOD, -among all other discharge products- for the first time. Precise spectroscopic data of HSOD have been obtained and compared to high level coupled cluster calculations. The experimentally derived molecular constants are in excellent agreement with the theoretically predicted values.

Based on the highly accurate data obtained in course of this thesis not only for HSOD but also for HSOH and H³⁴SOH as well as the previously published data on DSOD [19], it became possible to determine an empirical equilibrium structure of HSOH for the first time. HSOH is the simplest molecule possessing a classical S-O single bond and thus can be considered a test-bed for high-level *ab initio* calculations of S-O single bond molecules and of geometrical structure calculations in general. For none of the other oxoacids of sulfur -of composition H₂SO_{*n*} with *n* ranging from 1 to 4- an experimental equilibrium structure is reported, yet.

Due to the lack of experimentally available rotation-vibration interaction constants, values of high-level *ab initio* calculations have been used instead to determine the empirical equilibrium structure of HSOH. However, the results on vibrationally excited states of HSOH -presented in this thesis- prove the used *ab initio* values to be satisfactory. The fundamental OH-stretching mode documents HSOH to be a fairly rigid “textbook” molecule, displaying a clear-cut perpendicular and parallel-type spectrum without any perturba-

tion. In contrast to that finding the fundamental SH-stretching mode displays a strong potential coupling as well as a Coriolis-type coupling for the $K_a = 1$ energy level.

New experimental results on the ground state torsional splitting of the energy levels with $K_a = 4$ and 5 have been obtained by performing measurements on HSOH in the THz region. Furthermore, the by Yamada *et al.* [130] reported values of the torsional splitting of energy levels have been revised. The *Yamada-Winnewisser-Jensen* (YWJ) model gives a qualitative explanation of the observed dependence of the splitting on the quantum number K_a . In a collaboration with Ovsyannikov *et al.* the results presented here have been used to evaluate a new theoretical treatment complementing the work given by the YWJ model. Ovsyannikov *et al.* take a more direct approach for calculating the torsional splitting employing a newly computed *ab initio* potential energy surface together with the program TROVE. The splittings obtained by the approach are in excellent agreement with the experimental results presented here.

The highly sensitive measurements performed at 1.3 THz also allowed for the assignment of the H³⁴SOH isotopologue in natural abundance. Therefore the data set could be remarkably expanded and the accuracy of the molecular parameters has been significantly enhanced.

Transitions with $K_a = 1 \leftarrow 0$, $K_a = 2 \leftarrow 1$, and $K_a = 3 \leftarrow 2$ all exhibit strong *c*-type and somewhat weaker *b*-type transitions. On the contrary, transitions with $K_a = 4 \leftarrow 3$ display only *c*-type but no *b*-type transitions. The nonexistence of *b*-type transitions is completely unexpected and yet not well understood. Nevertheless, this effect seems to be of general spectroscopic relevance. A first rough explanation gives some evidence, that this effect should always occur in case of an asymmetric top molecule bearing a hindered internal rotation. Hence, a future goal is to find another candidate molecule having such traits to verify the concept given here.

The details on the synthesis of HSOH via pure sulfur, water, and energy are not well understood, yet. An open question -for instance- is the absence of the second singly deuterated oxadisulfane, DSOH, in the *rf*-discharge plasma. An aim of further investigations is to verify the hypothetical intermediate state H₂OS to be abundant in the plasma, and hence to clarify the exact reaction mechanism.

Nevertheless, this synthesis of oxadisulfane gives strong evidence that the molecule should be quite abundant in the interstellar medium. Hence, another future goal is to attempt the detection of this elusive species in space and thus to do a further step in understanding the chemical processes in the interstellar medium involving sulfur.

Bibliography

- [1] J. A. Altmann, N. C. Handy. Evaluation of the performance of the HCTH exchange-correlation functional using a benchmark of sulfur compounds. *Phys. Chem. Chem. Phys.* **1** (1999) 5529–5536.
- [2] J. A. Altmann, N. C. Handy, V. E. Ingamells. A study of sulphur-containing molecules using Hartree-Fock, MP2 and DFT (hybrid) methodologies. *Mol. Phys.* **92** (1997) 339–352.
- [3] J. A. Altmann, N. C. Handy, V. E. Ingamells. A Study of the Performance of Numerical Basis Sets in DFT Calculations on Sulfur-Containing Molecules. *Int. J. Quant. Chem.* **57** (1996) 533–542.
- [4] P. W. Atkins. *Quanta*. 2nd ed. Oxford University Press, New York (1991).
- [5] P. W. Atkins and R. S. Friedmann *Molecular Quantum Mechanics*. 3rd ed. Oxford University Press, New York (1997).
- [6] O. Baum, S. Esser, N. Gierse, S. Brünken, F. Lewen, J. Hahn, J. Gauss, S. Schlemmer, T. F. Giesen. Gas-phase detection of HSOD and empirical equilibrium structure of oxadisulfane. *J. Mol. Struct.* **795** (2006) 256–262.
- [7] (a) A. D. Becke. Density functional exchange energy approximation with correct asymptotic behaviour. *Physical Review* **A38** (1998) 3098–3100. (b) A. D. Becke. Density functional thermochemistry. III. The role of exact exchange. *Journal of Chemical Physics* **98** (1993) 5648–5652.
- [8] H. Beckers, S. Esser, T. Metzroth, M. Behnke, H. Willner, J. Gauss, J. Hahn. Low Pressure Pyrolysis of t-Bu₂SO: Synthesis and Infrared detection of HSOH. *Chem. Eur. J.* **12** (2006) 832–844.
- [9] M. Behnke, J. Suhr, S. Thorwirth, F. Lewen, H. Lichau, J. Hahn, J. Gauss, K. M. T. Yamada, G. Winnewisser. Gas-phase detection of discharge-generated DSOD. *J. Mol. Spectrosc.* **221** (2003) 121–126.

- [10] M. Behnke. 1-Oxadisulfan in der Gasphase - Entwicklung von Synthesen und Nachweismethoden. Ph.D. thesis, Universität zu Köln (2001).
- [11] J. Behrend, P. Mittler, G. Winnewisser, K. M. T. Yamada. Spectra of Deuterated Disulfane and Spectroscopic Determination of Its Molecular Structure. *J. Mol. Spectrosc* **150** (1991) 99–119.
- [12] J. B. Bell. Introductory Fourier Transform Spectroscopy. Academic Press, New York (1972)
- [13] V. A. Benderskii, E. V. Vetoshkin, S. Yu Grebenshchikov, L. von Laue, H. P. Trommsdorff. Tunneling splittings in vibrational spectra of non-rigid molecules I. Perturbative instanton approach. *Chem. Phys.* **219** (1997) 119–142.
- [14] V. A. Benderskii, I. S. Irgibaeva, E. V. Vetoshkin, H. P. Trommsdorff. Tunneling splittings in vibrational spectra of non-rigid molecules VIII. Six-dimensional tunneling dynamics of hydrogen peroxide and its isotopomers. *Chem. Phys.* **262** (2000) 369–391.
- [15] P. F. Bernath. Spectra of Atoms and Molecules. Oxford University Press, New York (1995).
- [16] HSSH Synthesis:
a) J. Bloch, F. Höhn, *Ber. Dtsch. Chem. Ges.* **41** (1908) 1975–1980
b) F. Fehér, M. Baudler, *Z. Annorg. Allg. Chem.* **253** (1947) 170–172
- [17] M. Brown, C. M. L. Kerr, F. D. Wayne, K. M. Evenson, and H. E. Radford. The far-infrared Laser Magnetic Resonance Spectrum of the OH radical. *J. Mol. Spectrosc.* **86** (1981) 544–554
- [18] Bruker, IFS 120 HR User's Manual
- [19] S. Brünken, M. Behnke, S. Thorwirth, K. M. T. Yamada, T. Giesen, F. Lewen, J. Hahn, G. Winnewisser. Asymmetric rotor analysis of DSOD spectra up to the rQ_3 branch near 653 GHz. *J. Mol. Struct.* **742** (2005) 237–242.
- [20] P. R. Bunker and P. Jensen. Molecular Symmetry and Spectroscopy, second ed., *NRC Research Press*, Ottawa (1998)
- [21] P. R. Bunker and P. Jensen. Fundamentals of Molecular Symmetry. IOP Publishing, Philadelphia (2005)
- [22] D. G. Burkhard and D. M. Dennison. The Molecular Structure of Methyl Alcohol. *Phys. Rev.* **84** (1951) 408–417.
- [23] A. G. W. Cameron. Abundances of the Elements in the Solar System. *Space Science Reviews* **15** (1973) 121–146.

- [24] J. H. Carpenter. Convergence of the Reduced Hamiltonian with Centrifugal Distortion in Asymmetric Top Molecules. *J. Mol. Spectrosc.* **46** (1973) 348–357.
- [25] G. Chattopadhyay, E. Schlecht, J. Gill, S. Martin, A. Maestrini, D. Pukala, F. Maiwald, and I. Mehdi. A Broadband 800 GHz Schottky Balanced Doubler. *IEEE Microwave and Wireless Components Letters* **12** (2002) 117–118.
- [26] D. B. Cook. Handbook of Computational Quantum Chemistry. Oxford University Press, New York (1998).
- [27] C. C. Costain. Determination of Molecular Structure from Ground State Rotational Constants. *J. Chem. Phys.* **29** (1958) 864–874.
- [28] T. W. Crowe, W. L. Bishop, D. W. Porterfield, J. L. Hesler, and R. M. Weikle. Opening the Terahertz Window With Integrated Diode Circuits. *IEEE J. of solid-state circuits* **40** 2104–2110 (2005).
- [29] C. Cullis and M. Hirschler. Atmospheric Sulfur - Natural and Man-Made Sources. *Atmos. Environ.* **14** (1980) 1263–1278
- [30] J. Dabrowicz, M. Mikolajczyk. A Facile and Selective Oxidation of Organic Sulphides to Sulphoxides with Hydrogen Peroxide/Selenium Dioxide System. *Synthesis* **10** (1978) 758–759.
- [31] T. David, S. Arscott, J.-M. Munier, T. Akalin, P. Mounaix, G. Beaudin, and D. Lippens. Monolithic integrated circuits incorporating InP-based heterostructure barrier varactors. *IEEE Microw. Wireless Compon. Lett.* **12** 281–283 (2002).
- [32] F. A. Davis and R. L. Billmers. Chemistry of sulfenic acids. 6. Structure of simple sulfenic acids generated by flash vacuum pyrolysis. *J. Org. Chem.* **50** (1985) 2593–2595
- [33] B. Decker, L. Babcock, N. Adams. Selected Ion Flow Tube Studies of $S^+(^4S)$ Reactions with Small Oxygenated and Sulfurated Organic Molecules. *J. Phys. Chem. A* **104** (2000) 801–810.
- [34] B. Decker, N. Adams, L. Babcock. Gas-phase reactivity of SO^+ : a selected ion flow tube study. *Int. J. Mass Spectrom.* **195/196** (2000) 185–201.
- [35] H. Dorsett and A. White. Overview on Molecular Modelling and *Ab initio* Molecular Orbital Methods Suitable for Use with Energetic Materials. DSTO Aeronautical and Maritime Research Laboratory, Salisbury, Australia (2000).
- [36] T. H. Dunning. Gaussian basis sets for use in correlated molecular calculations. I. The atoms boron through neon and hydrogen. *J. Chem. Phys.* **90** (1989) 1007–1023.

- [37] J. L. Durant. Evaluation of transition state properties by density functional theory. *Chemical Physics Letters* **256** (1996) 595–602.
- [38] C. Eckart. Some Studies Concerning Rotating Axes and Polyatomic Molecules. *Physical Review* **47** (1935) 552–558.
- [39] S. Esser. Untersuchungen zum Bildungsmechanismus von Oxadisulfan durch Pyrolyse von Di-*tert*-butylsulfoxid und Entwicklung einer neuen Synthesemethode für Oxadisulfan und seine Isotopomere. Ph.D. thesis, Universität zu Köln (2006).
- [40] HSSH Structure:
a) F. Fehér, M. Baudler, *Z. Electrochem.* **47** (1941) 844–848
b) J. Hahn, P. Schmidt, K. Reinartz, J. Behrend, G. Winnewisser, K. Yamada, *Z. Naturforsch.* **46b** (1991) 1338–1342
d) D. Dixon, D. Zeroka, J. Wendolowski, Z. Wasserman, *J. Chem. Phys.* **89** (1985) 5334–5336
e) J. Koput, *Chem. Phys. Lett.* **259** (1996) 146–150
- [41] J.-M. Flaud, C. Camy-Peyret, J. W. C. Johns, and B. Carli. The far infrared spectrum of H₂O₂. First observation of the staggering of the levels and determination of the *cis* barrier. *J. Chem. Phys.* **91** (1989) 1504–1510
- [42] M. Frenklach, J. H. Lee, J. N. White, and W. C. Gardiner, Jr.. Oxidation of Hydrogen-Sulfide. *Combust. Flame* **41** (1981) 1–16.
- [43] M. J. Frisch, G. W. Trucks, H. B. Schlegel, G. E. Scuseria, M. A. Robb, J. R. Cheeseman, J. A. Montgomery Jr., T. Vreven, K. N. Kudin, J. C. Burant, J. M. Millam, S. S. Iyengar, J. Tomasi, V. Barone, B. Mennucci, M. Cossi, G. Scalmani, N. Rega, G. A. Petersson, H. Nakatsuji, M. Hada, M. Ehara, K. Toyota, R. Fukuda, J. Hasegawa, M. Ishida, T. Nakajima, Y. Honda, O. Kitao, H. Nakai, M. Klene, X. Li, J. E. Knox, H. P. Hratchian, J. B. Cross, V. Bakken, C. Adamo, J. Jaramillo, R. Gomperts, R. E. Stratmann, O. Yazyev, A. J. Austin, R. Cammi, C. Pomelli, J. W. Ochterski, P. Y. Ayala, K. Morokuma, G. A. Voth, P. Salvador, J. J. Dannenberg, V. G. Zakrzewski, S. Dapprich, A. D. Daniels, M. C. Strain, O. Farkas, D. K. Malick, A. D. Rabuck, K. Raghavachari, J. B. Foresman, J. V. Ortiz, Q. Cui, A. G. Baboul, S. Clifford, J. Cioslowski, B. B. Stefanov, G. Liu, A. Liashenko, P. Piskorz, I. Komaromi, R. L. Martin, D. J. Fox, T. Keith, M. A. Al-Laham, C. Y. Peng, A. Nanayakkara, M. Challacombe, P. M. W. Gill, B. Johnson, W. Chen, M. W. Wong, C. Gonzalez, and J. A. Pople. Gaussian 03, Revision C.02. Gaussian, Inc., Wallingford, CT, (2004)
- [44] J. Gauss. *private communication*
- [45] J. W. Gewartowski and H. A. Watson. Principles of Electron Tubes. Van Nostrand, Princeton (1965).

- [46] HOOH Reviews:
a) Gmelin, 8th Edition, Oxygen, System-Nr. 3
b) Ullmann Vol. A13, 443–466
c) W. Schumb, C. Satterfield, R. Wentworth, *Hydrogen Peroxide*; Reinhold Publ. Co.: New York, (1955)
- [47] HSSH Review:
Gmelin, 8th Edition, Sulfur, System-Nr. 9, Supplement Vol. 4a/b
- [48] W. Gordy and R. L. Cook. Microwave Molecular Spectra, 3rd ed. Wiley, New York (1984).
- [49] M. Gottselig, D. Luckhaus, M. Quack, J. Stohner, and M. Willeke. Mode Selective Stereomutation and Parity Violation in Disulfane Isotopomers H₂S₂, D₂S₂, T₂S₂. *Helvetica Chemica Acta* **84** (2001) 1846–1861.
- [50] A. Goumri, J.-D. R. Rocha, D. Laakso, C. E. Smith, and P. Marshall. Computational studies of the potential surface for O(¹D)+H₂S: Characterization of pathways involving H₂SO, HSOH, and H₂OS. *J. Chem. Phys.* **101** 9405–9411.
- [51] P. Griffiths and J. de Haseth. Fourier Transform Infrared Spectroscopy, John Wiley & Sons, New York (1986)
- [52] T. I. Hasegawa, E. Herbst, C. M. Leung. Models of Gas-Grain Chemistry in Dense Interstellar Clouds with complex Organic-Molecules. *Astrophys. J. Supp.* **82** (1992) 167–195.
- [53] H. Heffner. Analysis of the Backward-Wave Travelling-Wave Tubes. *Proc. IRE* **42** (1954) 930–937.
- [54] W. J. Hehre, L. Radom, P. v. R. Schleyer, and J. A. Pople. *Ab initio* Molecular Orbital Theory. Wiley-Interscience, Brisbane, Australia (1986).
- [55] E. Herbst, G. Winnewisser, F. Lewen, S. Thorwirth, M. Behnke, J. Hahn, J. Gauss. Gas phase detection of HSOH: An Elusive species. *unpublished manuscript*
- [56] E. Herbst. The astrochemistry of H₃⁺. *Phil. Trans. Roy. Soc. Lond. A* **358** (2000) 2523–2534.
- [57] E. Herbst, G. Winnewisser, K. M. T. Yamada, D. J. DeFrees, and A. D. McLean. *Ab initio* determination of mode coupling in HSSH: The torsional splitting in the first excited S-S stretching state. *J. Chem. Phys.* **91** (1989) 5905–5909.
- [58] D. R. Herschbach and V. W. Laurie. Influence of Vibrations on Molecular Structure Determinations. I. General Formulation of Vibration Rotation Interactions. *J. Chem. Phys.* **37** (1962) 1668–1686; V. W. Laurie

- and D. R. Herschbach. Influence of Vibrations on Molecular Structure Determinations. II. Average Structures Derived from Spectroscopic Data. *J. Chem. Phys.* **37** (1962) 1687–1693
- [59] G. Herzberg. *Molecular Spectra and Molecular Structure II: Infrared and Raman Spectra of Polyatomic Molecules*. Van Nostrand, Princeton, N.J. (1945).
- [60] J. Hesler, D. Porterfield, W. Bishop, T. Crowe, A. Baryshev, R. Hesper, and J. Baselmans. Development and Characterization of an Easy-to-Use THz Source. *Proc. of the 16th Intl. Symposium on Space Terahertz Technology* Goteborg, Sweden, May 2005.
- [61] J. Hesler, D. Porterfield, W. Bishop, T. Crowe, A. Baryshev, R. Hesper, and J. Baselmans. Development and Characterization of an Easy-to-Use THz Source. *Proc. 16th Intl. Symposium on Space Terahertz Technology* (2005) Goteborg, Sweden.
- [62] J. T. Hougen and B. M. DeKoven. The Application of Extended Permutation-Inversion Groups to Internal Rotation of a Symmetric Rotor Top in a Symmetric or Asymmetric Rotor Molecule. *J. Mol. Spectrosc.* **98** (1983) 375–391.
- [63] J. T. Hougen. Summary of group theoretical results for microwave and infrared studies of H_2O_2 . *Can. J. Phys.* **62** (1984) 1392.
- [64] M. Iraqi, H. Schwarz. Experimental evidence for the gas phase existence of HSOH (hydrogen thioperoxide) and SOH_2 (Thioxonium ylide). *Chem. Phys. Lett.* **221** (1994) 359–362.
- [65] W. Jabs, M. Winnewisser, S. P. Belov, T. Klaus, and G. Winnewisser. The $r'Q_1$ branch of carbodiimide, HNCNH , at 1.1 THz. *Chem. Phys.* **225** (1997) 77–91.
- [66] H. R. Johnson. Backward-Wave Oscillator. *Proc. IRE* **43** (1955) 684–697.
- [67] D. Joubert. *Density Functionals: Theory and Applications*. Springer-Verlag, Heidelberg, DE (1998).
- [68] J. D. Kemp and K. S. Pitzer. The Entropy and the Third Law of Thermodynamics. Hindered Rotation of Methyl Groups. *J. Am. Chem. Soc.* **59** (1937) 276–279.
- [69] J. D. Kemp and K. S. Pitzer. Hindered Rotation of the Methyl Groups in Ethane. *J. Chem. Phys.* **4** (1936) 749.
- [70] R. A. Kendall, T. H. Dunning, and R. J. Harrison. Electron affinities of the first-row atoms revisited. Systematic basis sets and wave functions. *J. Chem. Phys.* **96** (1992) 6796–6806.

- [71] Y. Kimura, M. Yamamoto, S. Tobita, and H. Shizuka. Kinetic studies on the 1,2-sigmatropic hydrogen shift in the photorearranged intermediate of N-acetylpyrrole: Tunneling effects. *J. Chem Phys. A* **101** (1997) 459–465.
- [72] G. W. King, R. M. Hainer, and P. C. Cross. I. Calculation and Symmetry Classification of Energy Levels. *J. Chem. Phys* **11** (1943) 27–42.
- [73] W. Kohn, A. D. Becke, and R. G. Parr. Density functional theory of electronic structure. *Journal of Physical Chemistry* **100** (1996) 12974–12980.
- [74] R. Kompfer and N. T. Williams. Backward-Wave Tubes. *Proc. IRE* **41** (1953) 1602–1611.
- [75] M. Krach, J. Freyer, and M. Claassen. An integrated ASV frequency tripler for millimeter wave applications. *Proc. 33rd Eur. Microwave Conf.* **3** 1279–1281 (2003).
- [76] J. Kraitchman. Determination of Molecular Structure from Microwave Spectroscopic Data. *Am. J. Phys.* **21** (1953) 17–24
- [77] K. Kuchitsu. Comparison of Molecular Structures Determined by Electron Diffraction and Spectroscopy. Ethane and Diborane. *J. Chem. Phys.* **49** (1968) 4456–4462
- [78] C. Lee, W. Yang, and R. G. Parr. Development of the Colle-Salvetti correlation energy formula into a functional of the electron density. *Physical Review B37* **2** (1988) 785–789.
- [79] T. J. Lee, N. C. Handy, J. E. Rice, A. C. Scheiner, H. F. Schaefer III. The efficient evaluation of configuration interaction analytic energy second derivatives: Application to hydrogen thioperoxide, HSOH. *J. Chem. Phys.* **85** (1986) 3930–3938.
- [80] I. N. Levine. Quantum Chemistry. Allyn and Bacon, Inc., Boston (1983).
- [81] R. A. Linke, M. V. Schneider, and A. Y. Cho. Cryogenic millimeter-wave receiver using molecular beam epitaxy diodes. *IEEE Trans. Microw. Theory Tech.* **MTT-26** 935–938 (1978).
- [82] M. T. H. Liu, R. Bonneau, S. Wierlacher, and W. Sander. 1,2-H shift in benzylchlorocarbene - isotope effect and influence of the solvent. *J. of Photochem. and Photobiol. A-Chem.* **84** (1994) 133–137.
- [83] A. Maestrini, J. Ward, J. Gill, H. Javadi, E. Schlecht, C. Tripon-Canseliet, G. Chattopadhyay, and I. Mehdi. A 540-640 GHz High Efficiency Four Anode Frequency Tripler. *IEEE Transactions on Microwave Theory and Techniques* **53** (2005) 2835–2843.

- [84] A. Maestrini, J. Ward, J. Gill, G. Chattopadhyay, F. Maiwald, K. Ellis, H. Javadi, and I. Mehdi. A Planar-Diode Frequency Tripler at 1.9 THz. *Proc. of the 2003 IEEE MTT-S Int. Microwave Symp. Digest* Philadelphia, PA, June 2003
- [85] G. Menconi, D. J. Tozer. Structures and harmonic frequencies of sulfur-containing molecules: Assessment of the 1/4 exchange-correlation functional. *Phys. Chem. Chem. Phys.* **5** (2003) 2938–2941.
- [86] S. Mizushima. Structure of Molecules and Internal Rotation. *Academic*, New York (1954)
- [87] I. Morino and K. Kawaguchi. Fourier Transform Far-Infrared Spectroscopy of the SH Radical. *J. Mol. Spectrosc.* **170** (1995) 172–177
- [88] S. M. Nilsen, H. Gronqvist, H. Hjelmgren, A. Rydberg, and E. L. Kollberg. Single barrier varactors for submillimeter wave power generation. *IEEE Trans. Microw. Theory Tech.* **41** 572–580 (1993).
- [89] R. I. Ovsyannikov, V. V. Melnikov, W. Thiel, P. Jensen, O. Baum, T. F. Giesen, and S. N. Yurchenko. Theoretical rotation-torsion energies of HSOH. *J. Chem. Phys.* (2008) submitted.
- [90] W. J. Orville-Thomas. Internal Rotation In Molecules. *Wiley-Interscience*, New York (1974)
- [91] A. Otto and R. Steudel. Sulfur compounds, 211 - Gas-phase acidities of nine sulfur oxoacids of composition $[H_2S_nO_n]$ ($n=1-4$) *Eur. J. Inorg. Chem.* (2000) 617–624.
- [92] D. Papoušek and M. R. Aliev. Molecular Vibrational / Rotational Spectra. *Academica*, Prague (1982)
- [93] R. G. Parr and W. Yang. Density-Functional Theory of Atoms and Molecules, in International Series of Monographs on Chemistry, R. Breslow, J. B. Goodenough, J. Halpern, and J. Rolinson. Eds., Oxford University Press, New York (1989).
- [94] F. Pawłowski, P. Jørgensen, J. Olsen, F. Hegelund, T. Helgaker, J. Gauss, K. L. Bak, and J. F. Stanton. Molecular equilibrium structures from experimental rotational constants and calculated vibration-rotation interaction constants. *J. Chem. Phys.* **116** (2002) 6482–6496.
- [95] G. Pelz, K. M. T. Yamada, and G. Winnewisser. Torsional Dependence of the Effective Rotational Constants of H_2O_2 and H_2S_2 . *J. Mol. Spectrosc.* **159** (1993) 507–520.
- [96] HOOH Structure:
a) W. Penny, G. Sutherland, *Trans Faraday Soc.* **30** (1934) 898–902; *J. Chem. Phys.* **2**(1934) 492–498
b) D. Cremer, *J. Chem. Phys.* **69** (1978) 4440–4455

- c) S. Abrahams, R. Collin, W. Lipscomb, *Acta crystallogr. [Cambridge]* **4** (1951) 15–20
- d) W. Busing, H. Levy, *J. Chem. Phys.* **42** (1965) 3054–3059
- [97] J. P. Perdew, K. Burke, and Y. Wang. Generalised gradient approximation for the exchange-correlation hole of a many-electron system. *Physical Review* **B54** (1996) 16533–16539.
- [98] M. Philipp. Entwicklung und Aufbau eines BWO-basierten 1,9 THz Lokalszillatoren für den Heterodynempfänger GREAT. Ph.D. thesis, Universität zu Köln (2008).
- [99] H. .M. Pickett. The fitting and prediction of vibration-rotation spectra with spin interactions. *J. Mol. Spectrosc.* **148** (1991) 371–377.
- [100] A. S. Pine and P. F. Moulton. Doppler-limited and atmospheric spectra of the $4\mu\text{m } \nu_1 + \nu_3$ combination band of SO_2 . *J. Mol. Spectrosc.* **64** (1977) 15–30.
- [101] G. D. Purvis and R. J. Bartlett. A full coupled-cluster singles and doubles model: The inclusion of disconnected triples. *J. Chem. Phys.* **76** (1982) 1910–1918.
- [102] M. Quack, M. Willeke. Theory of Stereomutation Dynamics and Parity Violation in Hydrogen Thioperoxide Isotopomers $^{1,2,3}\text{HSO}^{1,2,3}\text{H}$. *Helvetica Chimica Acta* **86** (2003) 1641–1652.
- [103] K. Raghavachari, G. W. Trucks, J. A. Pople, and M. Head-Gordon. A fifth-order perturbation comparison of electron correlation theories. *Chem. Phys. Lett.* **157** (1989) 479–483.
- [104] J. Simons and J. Nichols. Quantum Mechanics in Chemistry. Oxford University Press, Oxford, UK (1997).
- [105] R. R. Smardzewski, M. C. Lin. Matrix Reactions of oxygen atoms with H_2S molecules. *J. Chem. Phys.* **66** (1977) 3197–3204.
- [106] B. Smith. Fundamentals of Fourier Transform Infrared Spectroscopy. CRC Press, Boca Raton (1996)
- [107] HOOH Synthesis:
L.-J. Thenard, *Ann. Chim. Phys.* **8** (1818) 306–313
- [108] G. Tyndall and A. Ravishankara. Atmospheric Oxidation of Reduced Sulfur Species. *Int. J. Chem. Kinet.* **23** (1991) 483–527.
- [109] V. Typke. Centrifugal Distortion Analysis Including P^6 -Terms. *J. Mol. Spectrosc.* **63** (1976) 170–179.

- [110] M. Urban, J. Noga, S. J. Cole, and R. J. Bartlett. Towards a full CCSDT model for electron correlation. *J. Chem. Phys.* **83** (1985) 4041–4046.
- [111] T. J. Viola and R. J. Mattauch. Unified theory of high-frequency noise in Schottky barrier diodes. *J. Appl. Phys.* **44** 2805–2808 (1973).
- [112] H. Wallmeier, W. Kutzelnigg. Nature of the Semipolar XO Bond. Comparative Ab Initio Study of H₃NO, H₂NOH, H₃PO, H₂POH, H₂P(O)F, H₂S₀, HSOH, HC10, ArO, and Related Molecules. *J. Am. Chem. Soc.* **101** (1979) 2084.
- [113] . N. Wang and C. Howard. Kinetics of the Reactions of HS and HSO with O₃. *J. Phys. Chem.* **94** (1990) 8787–8794.
- [114] J. K. G. Watson. A Planarity for Sextic Centrifugal Distortion Constants. *J. Mol. Spectrosc.* **65** (1977) 123–133.
- [115] J. K. G. Watson. Aspects of Quartic and Sextic Centrifugal Effects on Rotational Energy Levels. In *Vibrational Spectra and Structure* , J. R. Durig, Ed., Vol. 6, Marcel Dekker, New York (1977).
- [116] J. K. G. Watson. Centrifugal Corrections for Asymmetric-Top Molecules. *J. Chem. Phys.* **45** (1966) 1360–1361.
- [117] J. U. White. Long Optical Paths of Large Aperture. *J. Opt. Soc. Am.* **32** 285–288
- [118] D. H. Williams and E. Herbst. It’s a dusty Universe: surface science in space. *Surface Science* **500** (2002) 823–837.
- [119] A. K. Wilson and T. H. Dunning. SO₂ revisited: Impact of tight d augmented correlation consistent basis sets on structure and energetics. *J. Chem. Phys.* **119** (2003) 11712–11714.
- [120] G. Winnewisser and K. M. T. Yamada. Millimetre, submillimetre and infrared spectra of disulfane (HSSH) and its isotopic species. *Vib Spectrosc.* **1** (1991) 263–272.
- [121] G. Winnewisser, M. Winnewisser, W. Gordy. Millimeter-Wave Rotational Spectrum of HSSH and DSSD. I. *Q* Branches. *J. Chem. Phys.* **49** (1968) 3465–3478.
- [122] G. Winnewisser. Millimeter Wave Rotational Spectrum of HSSH and DSSD. II. Anomalous *K* Doubling Caused by Centrifugal Distortion in DSSD. *J. Chem. Phys.* **56** (1972) 2944–2954.
- [123] G. Winnewisser, F. Lewen, S. Thorwirth, M. Behnke, J. Hahn, J. Gauss, E. Herbst. Gas-Phase detection of HSOH: Synthesis by Flash Vacuum Pyrolysis of ditert-butyl-sulfoxide and rotational-torsional spectrum. *J. Chem. Phys.* **9** (2003) 5501–5510.

- [124] G. Winnewisser, A. F. Krupnov, M. Y. Tretyakov, M. Liedtke, F. Lewen, A. H. Saleck, R. Schieder, A. P. Shkaev, and S. V. Volokhov. Precision broadband Spectroscopy in the Terahertz Region. *J. Mol. Spectrosc.* **165** (1994) 294–300.
- [125] G. Winnewisser. Spectroscopy in the Terahertz region. *Vib. Spectrosc.* **8** (1995) 241.
- [126] D. E. Woon. Modeling gas-grain chemistry with quantum chemical cluster calculations. I. Heterogeneous hydrogenation of CO and H₂CO on icy grain mantles. *Astrophys. J.* **569** (2002) 541–548.
- [127] D. E. Woon and T. H. Dunning. Gaussian basis sets for use in correlated molecular calculations. III. The atoms aluminum through argon. *J. Chem. Phys.* **98** (1993) 1358–1371.
- [128] Q. Xiao, Y. Duan, J. L. Hesler, T. W. Crowe, and R. M. Weikle. A 5 mW and 5% efficiency 210 GHz InP-based heterostructure barrier varactor quintupler. *IEEE Microw. Wireless Compon. Lett.* **14** 159–161 (2004).
- [129] A. Yachmenev, W. Thiel, S. N. Yurchenko, O. Baum, M. Koerber, T. F. Giesen, S. Schlemmer, and P. Jensen. DIPOLE MOMENT SURFACE AND ROTATION-TORSION INTENSITIES OF HSOH. *20th Intl. Conference on High Resolution Molecular Spectroscopy*, Prague, (2008)
- [130] K. M. T. Yamada, G. Winnewisser, P. Jensen. Internal rotation tunnelling in HSOH. *J. Mol. Struct.* **695–696** (2004) 323–337.
- [131] D. T. Young and J. C. Irvin. Millimeter frequency conversion using Au-n-type GaAs Schottky barrier epitaxial diodes with a novel contacting technique. *Proc. IEEE* **53** 2130–2131 (1965).
- [132] S. N. Yurchenko, W. Thiel, and P. Jensen. Theoretical ROVibrational Energies (TROVE): A robust numerical approach to the calculation of rovibrational energies for polyatomic molecules. *J. Mol. Spectrosc.* **245** (2007) 126–140.
- [133] S. N. Yurchenko. *private communication*
- [134] R. N. Zare. Angular Momentum. Wiley, New York (1988) 266–277.
- [135] Guide for Infrared Spectroscopy. www.brukeroptics.de
- [136] B. P. van Eijck. Reformulation of Quartic Centrifugal Distortion Hamiltonian. *J. Mol. Spectrosc.* **53** (1974) 246–249.
- [137] F. Lewen, E. Michael, R. Gendriesch, J. Stutzki, and G. Winnewisser. Terahertz laser sideband spectroscopy with backward wave oscillators. *J. Mol. Spectrosc.* **183** (1997) 207–209.

Danksagung

Ich möchte mich bei allen bedanken, die mich während meiner gesamten Promotionszeit unterstützt haben und mit dazu beigetragen haben, dass diese erfolgreich abgeschlossen werden konnte.

An erster Stelle möchte ich mich bei Priv.-Doz. Dr. Thomas F. Giesen dafür bedanken, dass er die Betreuung meiner Arbeit übernommen hat, und mir darüber hinaus -bei einer oder zwei Tassen Kaffee- mit fruchtbaren fachlichen Diskussionen immer wieder neue Impulse gegeben hat.

Ich möchte Herrn Prof. Dr. Markus Grüninger für die Übernahme des Zweitgutachtens danken. Ein weiterer Dank geht an Prof. Dr. Axel Klein für die Bereitschaft, den Vorsitz der Disputationsprüfung zu übernehmen. Herrn Dr. Frank Lewen danke ich für das technische Know-How und für die Übernahme des Besitzes.

Bei Prof. Dr. Stephan Schlemmer möchte ich mich für diverse Diskussionen und das sehr angenehme Arbeitsklima innerhalb seiner Gruppe bedanken.

Many thanks to Prof. Dr. K. M. T. Yamada for all the helpful discussions and valuable suggestions concerning the spectra of HSOH.

Herrn Prof. Dr. Gisbert Winnewisser möchte ich für sein generelles Interesse an meiner Arbeit und für die Bereitstellung der ersten HSOH Daten danken.

Dir, Monika Koerber gilt ein ganz besonderer Dank. Sei es für das unentwegte Korrekturlesen, für die tolle Unterstützung bei Messungen oder auch für deine Hilfe beim "layouten" dieser Arbeit. Und nicht zu vergessen, für die Versorgung mit Keksen und Müsliriegeln gerade in der Endphase meiner Arbeit.

Ein ganz großes Dankeschön geht auch an Dr. Petra Neubauer-Guenther und an Serjoscha "Joschi" Wahed für das fleißige Korrekturlesen.

Herrn Prof. Dr. Jürgen Gauss danke ich für die gute Zusammenarbeit und seine hervorragenden Rechnungen zum HSOH-Molekül und seinen Isotopologen.

Der gesamten "Speckis"-Gruppe danke ich ganz herzlich für die große Unterstützung und das angenehme Arbeiten während meiner Promotionszeit. Besonders auch für die freundliche Aufnahme von Matthias, auch schon während meiner Babypause.

Herrn Dr. Holger S. P. Müller danke ich für diverse Tipps rund um das Pickett-Programm (nicht nur im Bezug auf die "Fourierentwicklung").

Nicht vergessen möchte ich die "Garde der ersten Stunde", dazu zählen u.a.

Dr. Michael Caris, Dr. Sandra Brünken, Holger Spahn, Christian Endres und Manuela Sornig.

Priv.-Doz. Dr. Helmut Beckers möchte ich danken für die Unterstützung bei den IR-Messungen in Wuppertal. Auch Dr. Simone Esser gilt ein großes Dankeschön für unsere gemeinsame Zeit in Wuppertal, und darüber hinaus der stets guten Zusammenarbeit.

Allen Chemikern die für mich den Precursor herstellen durften oder mussten, insbesondere Yvonne von Mering und Mike Polinowski, als auch Prof. Dr. Josef Hahn: Danke!

Ein Dankeschön geht sowohl an die feinmechanische wie auch an die elektronische Werkstatt für die Herstellung all der "kleinen" Bauteile ohne die eine experimentelle Arbeit nicht möglich wäre.

Für die gute Zusammenarbeit und den letzten erhellenden Impuls dieser Arbeit danke ich Dr. Sergei Yurchenko.

Herrn Prof. Dr. Klaus Müllen möchte ich für den kleinen, aber wichtigen Anstoss danken, der mich letztendlich zum Promovieren motivierte.

Allen Freunden danke ich für das rege Interesse und das Mitfiebern während der Promotionszeit.

Meiner Schreibgruppe, ganz besonders Bettina Grimmer, möchte ich für die vielen arbeitsreichen, aber auch schönen Stunden, für aufmunternden Worte und des "Einfach-Daseins" danken.

Ein ganz besonders herzlicher Dank geht an Jutta und Klaus Grimmer, deren enorme Unterstützung bzgl. der Betreuung von Matthias und darüber hinaus das Fertigstellen der Arbeit mit ermöglicht haben.

Ein großes Dankeschön geht an die Elfs, Angelika und Heinz Baum, die mir überhaupt erst ein Studium der Physik ermöglicht und somit die Basis für eine Promotion geschaffen haben.

Desweiteren möchte ich mich vielmals bei Nicole Kramer für die tolle und in der Endphase der Promotion auch oft spontane Betreuung von Matthias bedanken. Es hilft ungemein zu wissen, dass Matthias gut aufgehoben ist.

Nicht zuletzt will ich meiner geliebten Sonja für ihre immer währende Unterstützung und ihr Verständnis -vorallem auch zum Ende der Arbeit- danken. Ohne Sie wäre diese Arbeit nie geschrieben worden! "Du bist nicht alles, aber ohne dich ist alles nichts!"

Erklärung

Ich versichere, daß ich die von mir vorgelegte Dissertation selbständig angefertigt, die benutzten Quellen und Hilfsmittel vollständig angegeben und die Stellen der Arbeit - einschließlich Tabellen, Karten und Abbildungen -, die anderen Werken im Wortlaut oder dem Sinn nach entnommen sind, in jedem Einzelfall als Entlehnung kenntlich gemacht habe; daß diese Dissertation noch keiner anderen Fakultät oder Universität zur Prüfung vorgelegen hat; daß sie - abgesehen von unten angegebenen Teilpublikationen - noch nicht veröffentlicht worden ist sowie, daß ich eine solche Veröffentlichung vor Abschluß des Promotionsverfahrens nicht vornehmen werde. Die Bestimmungen dieser Promotionsordnung sind mir bekannt. Die von mir vorgelegte Dissertation ist von Privatdozent Dr. Thomas F. Giesen betreut worden.

Teilpublikationen

- O. Baum, S. Esser, N. Gierse, S. Brünken, F. Lewen, J. Hahn, J. Gauss, S. Schlemmer, T. F. Giesen. Gas-phase detection of HSOD and empirical equilibrium structure of oxadisulfane. *J. Mol. Struct.* **795** (2006) 256–262.
- O. Baum, T. F. Giesen, and S. Schlemmer. High-resolution infrared measurements on HSOH: Analysis of the OH fundamental vibrational mode. *J. Mol. Spectrosc.* (2008) **247** 25–29.
- R. I. Ovsyannikov, V. V. Melnikov, W. Thiel, P. Jensen, O. Baum, T. F. Giesen, and S. N. Yurchenko. Theoretical rotation-torsion energies of HSOH. *J. Chem. Phys.* (2008) submitted.
- O. Baum, M. Koerber, S. Yurchenko, W. Thiel, P. Jensen, S. Schlemmer, and T. F. Giesen. High resolution infrared measurements on HSOH. Analysis of the SH fundamental vibrational mode. *J. Mol. Spectrosc.* in preparation.
- O. Baum, M. Koerber, O. Ricken, G. Winnewisser, S. Schlemmer, K. M. T. Yamada, and T. F. Giesen. The Rotational Spectrum of H³²SOH and H³⁴SOH above 1 THz. *J. Chem. Phys.* in preparation.

Lebenslauf

Oliver Baum
Ferdinand-Schmitz-Str. 5
50969 Köln

Geburtstag: 23.05.1975
Geburtsort: Köln
Staatsangehörigkeit: deutsch
Familienstand: verheiratet, ein Kind

Schulausbildung:

1981–1985 Katholische Grundschule Lohrbergstrasse, Köln
Zulassung zum Gymnasium
1985–1994 Elisabeth von Thüringen Gymnasium, Köln
06/1994 Abitur

Studium:

10/1994 Beginn des Studiums an der Universität zu Köln
Fachrichtung: Mathematik Diplom
10/1995 Fachrichtung: Mathematik & Physik Staatsexamen Sek. I+II
03/2003–09/2003 Staatsexamenarbeit am II. Physikalischen Institut
“Aufbau eines Praktikumsversuches für Fortgeschrittene: Fourier-Spektroskopie mehratomiger Gase”
11/2003 1. Staatsexamen für Sek. I+II in Mathematik und Physik
01/2004 Beginn des Promotionsstudiums
Universität zu Köln

Wehrdienst:

05/1994–05/2001 Ersatzdienst im Katastrophenschutz bei dem
Arbeiter-Samariter-Bund Ortsverband Köln

Berufs- und Familientätigkeit:

07/1999–05/2002 Werkstudent, EDV-Support im Gerling-Konzern, Köln
05/2002–12/2003 Studentische Hilfskraft am II. Physikalischen Institut
01/2003–03/2007 Wissenschaftlicher Mitarbeiter am I. Physikalischen Institut
04/2007–03/2008 Elternzeit
seit 03/2008 Wissenschaftlicher Mitarbeiter am I. Physikalischen Institut